State and parameter estimation of physics-based lithium-ion battery models

Adrien Bizeray

Department of Engineering Science

University of Oxford

This dissertation is submitted for the degree of

Doctor of Philosophy

Kellogg College

Michaelmas 2016

To my parents.

To Yunyun.

Acknowledgements

This work was undertaken as part of a Global Research Outreach (GRO) collaborative project between the Samsung Advanced Institute of Technology (SAIT) and the University of Oxford. I am extremely grateful to Samsung Electronics Co. Ltd. and the Samsung Advanced Institute of Technology for funding this project and sharing experimental data to support my research.

Personally, I would also like to take this opportunity to thank my fantastic supervisor Prof David Howey for his enthusiasm and essential guidance that kept me on-target and motivated during this few years of DPhil. I am very proud to be with Rob and Chris one of the original three DPhil students under Dave's supervision and I can say with confidence that I couldn't have asked for a better supervisor.

I also wish to thank my co-supervisor Prof Stephen Duncan for his time and invaluable advice throughout this DPhil. This project has taken directions that would not have been possible without his suggestions and extensive knowledge.

I thank Dr Adam Mahdi for taking the time to help me comprehend the concept of structural identifiability, and Prof Charles Monroe for offering me the opportunity to collaborate with him on a journal publication.

I am very lucky to work with great people and my time studying in Oxford has been a delight thanks to them. I would like to thank all past and present fellow members and friends of the Energy and Power Group for the pleasant working environment they contributed to. I thank in particular the 'Holder team' for all the daily laughs and support that made this experience so enjoyable.

Especially, I wish to thank Dr Shi Zhao as a friend and colleague. He has been an invaluable source of advice and knowledge during this DPhil. I also thank Christoph Birkl and Dr Robert Richardson, aka Chris and Rob, for sharing this DPhil experience with me from the very beginning (a long time ago, in a tiny office) and helping me in countless ways throughout the years, from performing experimental tests in the lab to proofreading my thesis.

I would like to thank Yunyun for being by my side everyday and supporting me with love and affection. She has been an essential source of inspiration and motivation and I could simply not have done this without her. I would also like to take this opportunity to thank Yunyun's family for their generosity and kindness, and for welcoming me as a family member.

Most importantly, I am very grateful to my parents for their everlasting love and unwavering support. They supported me in all possible ways and could not have offered me a better education. I am privileged to have such wonderful parents and cannot possibly thank them enough.

Thank you.

Publications

The vast majority of the work presented in this thesis has been published in the joint-author peer-reviewed journal and conference publications listed below:

[1] A.M. Bizeray, S.R. Duncan, and D.A. Howey, Advanced battery management systems using fast electrochemical modelling. In *Proceedings of the 4th Hybrid and Electric Vehicles Conference IET 2013 (HEVC 2013)*, London, United Kingdom, 2013. [Publisher copy]

[2] A.M. Bizeray, S. Zhao, S.R. Duncan, and D.A. Howey, Lithium-ion battery thermal-electrochemical model-based state estimation using orthogonal collocation and a modified extended Kalman filter. *Journal of Power Sources* 296 (2015) 400–412. [Publisher copy and open access pre-print]

[3] S. Zhao, A.M. Bizeray, S.R. Duncan, and D.A. Howey, Performance evaluation of an extended Kalman filter for state estimation of a pseudo-2D thermal-electrochemical lithium-ion battery model. In *Proceedings of the ASME 2015 Dynamic Systems and Control Conference (DSCC 2015)*, Columbus, Ohio, USA, 2015. [Publisher copy]

[4] A.M. Bizeray, D.A. Howey, and C.W. Monroe, Resolving a Discrepancy in Diffusion Potentials , with a Case Study for Li-Ion Batteries. *Journal of the Electrochemical Society* **163**(8) E223-E229 (2016). [Open-access publisher copy]

[5] A.M. Bizeray, J–H Kim, S.R. Duncan, and D.A. Howey, Identifiability of the single particle Li-ion battery model, **(In preparation)**.

I contributed the theory, code development and results analysis for the fast solution using Chebyshev orthogonal collocation and the state estimation using Kalman filtering of the pseudo-two dimensional model discussed in [1–3] and for the analysis of the single-particle model parameter identifiability discussed in [5]. Dr Shi Zhao assisted me with the development and debugging of the Kalman filtering estimation algorithm in [2, 3]. I wrote the journal publications [1, 2, 5] and Dr Shi Zhao wrote most of [3]. Prof Stephen Duncan and Prof David Howey provided the problem motivations, the foundation of the theory and general advice on [1–3, 5] and proof-read all of these publications. All theoretical arguments discussed in [4] regarding the Nernst–Planck and Onsager–Stefan–Maxwell approaches for modelling concentration over-potentials in electrolytic solution were developed and written by Prof Charles Monroe. In [4], I compiled and calculated the transport properties presented in Table I and wrote the 'Case Study for Lithium-Ion Battery Simulation', including performing the P2D model simulations shown in Figure 1.

This dissertation is my own work and contains nothing which is the outcome of work done by collaborators or others unless specified otherwise and duly referenced in the text.

Adrien Bizeray

Michaelmas 2016

Abstract

This thesis investigates novel algorithms for enabling the use of first-principle electrochemical models for battery monitoring and control in advanced battery management systems (BMSs). Specifically, the fast solution and state estimation of a high-fidelity spatially resolved thermal-electrochemical lithium-ion battery model commonly referred to as the pseudo two-dimensional (P2D) model are investigated. The partial-differential algebraic equations (PDAEs) constituting the model are spatially discretised using Chebyshev orthogonal collocation enabling fast and accurate simulations up to high C-rates. This implementation of the P2D model is then used in combination with an extended Kalman filter (EKF) algorithm modified for differential-algebraic equations (DAEs) to estimate the states of the model, *e.g.* lithium concentrations, overpotential. The state estimation algorithm is able to rapidly recover the model states from current, voltage and temperature measurements. Results show that the error on the state estimate falls below 1 % in less than 200 s despite a 30 % error on battery initial state-of-charge (SoC) and additive measurement noise with 10 mV and 0.5 °C standard deviations.

The parameter accuracy of such first-principle models is of utmost importance for the trustworthy estimation of internal battery electrochemical states. Therefore, the identifiability of the simpler single particle (SP) electrochemical model is investigated both in principle and in practice. Grouping parameters and partially non-dimensionalising the SP model equations in order to understand the maximum expected degrees of freedom in the problem reveals that there are only six unique parameters in the SP model. The structural identifiability is then examined

by asking whether the transfer function of the linearised SP model is unique. It is found that the model is unique provided that the electrode open circuit voltage curves have a non-zero gradient, the parameters are ordered, and that the behaviour of the kinetics of each electrode is lumped together into a single parameter which is the charge transfer resistance. The practical estimation of the SP model parameters from frequency-domain experimental data obtained by electrochemical impedance spectroscopy (EIS) is then investigated and shows that estimation at a single SoC is insufficient to obtain satisfactory results and EIS data at multiple SoCs must be combined.

Table of contents

List of figures **xiii**

List of tables **xvi**

Nomenclature **xvii**

1 Introduction **1**

1.1 Research motivations and objectives 1

1.2 Background and literature review 3

1.2.1 Li-ion battery fundamentals 3

1.2.2 Battery modelling 5

1.2.3 Fast electrochemical modelling for BMSs 6

1.2.4 Model parameter estimation 7

1.3 Overview of the present work 12

2 Li-ion battery physics-based models **16**

2.1 The pseudo-two dimensional model 17

2.1.1 A multi-scale model 17

2.1.2 Transport of lithium 21

2.1.3 Electrode kinetics 23

2.1.4 Equilibrium potential and overpotential 24

2.1.5 A differential-algebraic problem 28

2.2 The single-particle model 33

2.2.1 Solid-phase diffusion model with uniform reaction rate . . . 34
2.2.2 Voltage measurement equation . . . 35
2.3 Thermal model . . . 36
2.3.1 Overview of literature . . . 37
2.3.2 Bulk thermal model . . . 39
2.3.3 Heat generation rate . . . 42
2.3.4 Temperature-dependent electrochemical parameters . . . 43

3 Fast solution of electrochemical models using orthogonal collocation 45

3.1 Chebyshev orthogonal collocation . . . 45
3.1.1 Chebyshev polynomials approximation . . . 45
3.1.2 Differentiation . . . 47
3.1.3 Integration and Quadrature . . . 48
3.2 Spatial discretisation of the P2D model . . . 50
3.2.1 Computational domain decomposition . . . 50
3.2.2 Solid-phase diffusion model . . . 52
3.2.3 Electrolyte diffusion model . . . 57
3.2.4 Electrolyte and solid-phase current densities . . . 67
3.2.5 Solid-phase and electrolyte potentials . . . 68
3.2.6 Reaction rate . . . 70
3.2.7 Thermal model . . . 70
3.3 A semi-explicit DAEs system . . . 70
3.3.1 DAE state-space formulation of the discretised model . . . 70
3.3.2 Solution of DAE systems . . . 72
3.4 P2D model performance . . . 74
3.4.1 COMSOL® P2D model implementation . . . 75
3.4.2 Model parameters from literature . . . 76
3.4.3 Constant current discharge . . . 76

3.4.4 Dynamic current input 83
3.5 Concluding remarks 87

4 State estimation using a modified extended Kalman filter 88
4.1 Kalman filtering 89
4.2 P2D model state estimation algorithm 91
4.2.1 Battery stochastic state-space model 91
4.2.2 DAE state-space model linearisation 92
4.2.3 Summary of modified EKF for non-linear DAEs 95
4.3 Results and discussion 97
4.3.1 Constant-current discharge 99
4.3.2 Dynamic current input 100
4.3.3 Performance with reduced number of collocation nodes . . 101
4.3.4 Comparison with SP model-based state estimation 103
4.3.5 Effect of voltage measurement noise 103
4.4 Concluding remarks 104

5 Identifiability analysis and SP model parameter estimation 106
5.1 SP model grouped parameters 107
5.2 Structural identifiability 111
5.2.1 Diffusion model transcendental transfer function 112
5.2.2 Linearisation of the voltage measurement equation 114
5.2.3 Transfer function of the linearised SP model 116
5.2.4 Structural identifiability analysis 121
5.3 Frequency-domain parameter estimation 122
5.3.1 Single DoD parameter estimation 123
5.3.2 Combined DoDs parameter estimation 123
5.3.3 Estimation of the charge-transfer resistance by linear regression 124

5.4 Results and discussion 126
5.4.1 Parameter estimation using synthetic data 126
5.4.2 Parameter estimation using experimental data 129
5.5 Concluding remarks 136

6 Conclusion **138**
6.1 Summary of dissertation and contributions 138
6.2 Future work and perspectives 141

Appendix A Modelling of degradation by SEI layer growth **144**

Appendix B Discretisation of the spherical diffusion equation using symmetry **151**

References **156**

List of figures

1.1 Structure and operating principle of a lithium-ion cell. 3

1.2 Graphical abstract of the P2D model state estimation approach [2]. 14

2.1 Schematic of the cell computational domains [2]. 19

2.2 Comparison of P2D model predictions using the NP potential or the potential measured by a reference electrode (OSM) as electrolyte potential [4]. 27

2.3 Block diagram showing the interdependencies of the P2D model equations, dependent variables and input/output. 32

3.1 Schematic of the cell domain decomposition into sub-domains and their mapping onto the Chebyshev nodes computational domains [2]. 51

3.2 Schematic showing the number of orthogonal collocation nodes used to discretise each computational sub-domain. 61

3.3 Comparison of various piecewise interpolation techniques. 75

3.4 Comparison of voltage predicted by the P2D model under constant current discharge at several C-rates computed using orthogonal collocation and the high-fidelity COMSOL® model [2]. 78

3.5 Decreasing voltage and SoC prediction error with increasing number of collocation nodes [2]. 80

3.6 Electrolyte concentration and reaction rate profiles across the cell [2]. 82

3.7 Bode plot of the frequency response of the anode solid-phase particle model with increasing number of Chebyshev collocation nodes. . . 83
3.8 Input current (C-rate), voltage and temperature predicted by the thermal-P2D model under a Combined ARTEMIS Driving Cycle [2]. 86
3.9 Cumulative heat generated and convective heat removed per cell unit volume under the CADC [2]. 86

4.1 Performance of the state estimation algorithm during constant current discharge [2]. 98
4.2 Performance of the state estimation algorithm during CADC discharge [2]. 100
4.3 Anode bulk SoC estimation error with reduced number of collocation nodes and SP model-based EKF estimation [3]. 102
4.4 Electrolyte concentration (at the anode current collector) estimation error with reduced number of collocation nodes [3]. 102
4.5 Anode bulk SoC estimation error with increasing voltage measurement noise [3]. 104

5.1 Nyquist plot of the SP model transfer function with varying time constants [5]. 119
5.2 Contour plot of the parameter estimation loss function at several DoDs based on synthetic EIS data [5]. 127
5.3 Contour plot of the parameter estimation loss function based on synthetic experimental data with combined DoDs [5]. 128
5.4 Nyquist plot of the electrochemical impedance of a Kokam SLPB 533459H4 740 mA h NMC cell [5]. 130
5.5 Charge-transfer resistance against DoD estimated from experimental data by linear regression [5]. 131

5.6 Contour plot of the loss function based on experimental EIS data at several DoDs, experimental OCP curves and fitted frequency-response. 133
5.7 Contour plot of the loss function based on experimental EIS data combining several DoDs [5]. 135

A.1 Voltage predicted by the model under $1C$ discharge/charge cycling at various cycles ranging from cycle 1 to 5000. 148
A.2 Capacity loss at different C-rates as a function of cycle number and time. 149
A.3 Effect of operating voltage window on SEI formation. 149
A.4 Evolution of the SEI layer thickness and capacity loss with cycle number at 15 °C, 30 °C and 60 °C. 150

List of tables

1.1 Summary of the literature on the parameter estimation of electrochemical lithium-ion battery models. 13

3.1 Parameters of the electrochemical P2D model [2]. 77

3.2 Thermal model parameters [2]. 77

Nomenclature

Abbreviations

BDF	Backward Differentiation Formulae
BMS	Battery Management System
CADC	Combined ARTEMIS Drive Cycle
CPE	Constant-Phase Element
DAE	Differential Algebraic Equation
DMC	Dimethyl Carbonate
DoD	Depth-of-Discharge
EC	Ethylene Carbonate
ECM	Equivalent Circuit Model
EIS	Electrochemical Impedance Spectroscopy
EKF	Extended Kalman Filter
EMC	Ethyl Methyl Carbonate
EV	Electric Vehicle
GEIS	Galvanostatic Electrochemical Impedance Spectroscopy
GITT	Galvanostatic Intermittent Titration Technique
HEV	Hybrid Electric Vehicle
IBVP	Initial Boundary Value Problem
LCO	$LiCoO_2$
LFP	$LiFePO_4$
LMO	$LiMn_2O_4$
NCA	$LiNiCoAlO_2$

NDF	Numerical Differentiation Formulae
NMC	$LiNiMnCoO_2$
NP	Nernst–Planck
OCP	Open Circuit Potential
OCV	Open Circuit Voltage
OSM	Onsager–Stefan–Maxwell
P2D	Pseudo Two-Dimensional
PC	Propylene Carbonate
PDAE	Partial Differential Algebraic Equation
PDE	Partial Differential Equation
PHEV	Plug-in Hybrid Electric Vehicle
SEI	Solid-Electrolyte Interphase
SoC	State-of-Charge
SoH	State-of-Health
SP	Single Particle

Roman

A	electrode surface area, m^2
A_{cell}	cell surface area, m^2
a_{s}	electrode specific interfacial area, $\mathrm{m}^2\,\mathrm{m}^{-3}$
b	Bruggeman coefficient
Bi	Biot number
c	concentration, $\mathrm{mol}\,\mathrm{m}^{-3}$
c_{T}	total solution concentration, $\mathrm{mol}\,\mathrm{m}^{-3}$
D	diffusivity, $\mathrm{m}^2\,\mathrm{s}^{-1}$
D'_N	N^{th} order first-derivative Chebyshev differentiation matrix
D''_N	N^{th} order second-derivative Chebyshev differentiation matrix
E^{ψ}_{act}	activation energy of parameter ψ, $\mathrm{kJ}\,\mathrm{mol}^{-1}$

$\mathcal{F}$	Faraday's constant, $\mathrm{C\,mol^{-1}}$
h	convective heat transfer coefficient, $\mathrm{W\,m^{-2}\,K^{-1}}$
I	current, A
i	current density, $\mathrm{A\,m^{-2}}$
i_0	exchange current density, $\mathrm{A\,m^{-2}}$
I_N	N^{th} order Chebyshev integration matrix
j	reaction rate, $\mathrm{mol\,m^{-2}\,s^{-1}}$
K	see N_s
k	reaction rate constant, $\mathrm{m^{2.5}\,mol^{-0.5}\,s^{-1}}$
L	cell thickness, m (or loss function in Chapter 5)
L_c	characteristic length, m
M	see N_a
N	see N_p
n	number of electrons per reaction
N_a	number of collocation nodes in anode $M+1$
N_c	number of collocation nodes in cathode $Q+1$
N_s	number of collocation nodes in separator $K+1$
N_p	number of collocation nodes in particles $N+1$
n_x	number of model differential states
n_z	number of model algebraic states
P	state estimation error covariance matrix
Q	see N_c
Q^{th}	theoretical electrode capacity, A h
Q	process noise covariance matrix
$\dot{q}$	heat generation rate, W
$\dot{q}''$	heat generation rate per unit area, $\mathrm{W\,m^{-2}}$
$\dot{q}'''$	heat generation rate per unit volume, $\mathrm{W\,m^{-3}}$
R	gas constant, $\mathrm{J\,mol^{-1}\,K^{-1}}$

R_{ct}	charge transfer resistance, Ω
R_{ctc}	normalised contact resistance $\Omega\,\mathrm{m}^2$
R	measurement noise covariance matrix
R_{s}	radius of particles, m
S	entropy, $\mathrm{J\,mol^{-1}\,K^{-1}}$
T	temperature, K
T_k	Chebyshev polynomial of the first-kind of degree k
T_{s}	sampling period, s
t_+	cation transference number
U	open-circuit potential, V
u	model scalar input
V	cell voltage, V
V_{cell}	cell volume, m^3
$\mathbf{w}_N^{\mathrm{T}}$	Clenshaw–Curtis quadrature weights (order N)
$\mathbf{x}$	vector of differential states
x_{s}	stoichiometry
$\mathbf{y}$	vector of measurements
$\mathbf{z}$	vector of algebraic states
Z	cell impedance, Ω
z	ion charge number

Greek

α	OCP slope w.r.t. stoichiometry, V
α_a	anodic charge transfer coefficient
α_c	cathodic charge transfer coefficient
β	OCP slope w.r.t. capacity, $\mathrm{V\,(Ah)^{-1}}$
δ	thickness of cell layers, m
ΔS	entropy change, $\mathrm{J\,mol^{-1}\,K^{-1}}$

ϵ	volume fraction of a phase
η	overpotential, V
θ	vector of model parameters
κ	ionic conductivity, $\mathrm{S\,m^{-1}}$
λ	thermal conductivity, $\mathrm{W\,m^{-1}\,K^{-1}}$
ν	stoichiometric coefficient
ρ	cell bulk density, $\mathrm{kg\,m^{-3}}$
σ	electrical conductivity, $\mathrm{S\,m^{-1}}$ (or see σ_V and σ_T)
σ_T	temperature measurement standard deviation, K
σ_V	voltage measurement standard deviation, V
τ	time constant, s
Φ	state transition matrix
ϕ	electric potential, V (or basis function in Section 3.1 only)
Ω	computational domain
ω	angular frequency, $\mathrm{rad\,s^{-1}}$

Subscripts

amb	ambient
app	applied
conv	convection
ctc	contact
D	diffusional
e	electrolyte
gen	generation
id	identified
ohm	ohmic
r	radial
rev	reversible

rxn	reaction
s	solid-phase (or separator for N_s)
sol	solvent
sr	side reaction
surf	surface
tot	total
x	(referring to) differential states
z	(referring to) algebraic states (or 'axial' in Section 2.3.2 only)
0	initial value or linearisation point
1	anode domain
2	separator domain
3	cathode domain
+	cation, or cathode in Chapter 5
−	anion, or anode in Chapter 5

Superscripts

avg	average
cc	current collector
d	diffusion
eff	effective
k	kinetic
lin	linearised
r	micro-scale particle domain
ref	reference
surf	surface
th	theoretical
0	initial value or linearisation point
0 %	at 0 % SoC

100 %	at 100 % SoC
–	prior estimate

Chapter 1

Introduction

1.1 Research motivations and objectives

Lithium-ion batteries are widely used in electric vehicles (EVs) and hybrid electric vehicles (HEVs) due to their high energy and power density compared to other battery chemistries. Furthermore, the cost of lithium-ion battery packs has been decreasing rapidly over the last decade by about 8 % annually [6], which also makes lithium-ion batteries of increasing interest in grid applications [7, 8]. However, scaling up the size of battery packs for automotive and other applications raises new safety and reliability challenges that require the development of novel sophisticated battery management systems (BMSs). A BMS consists of hardware and embedded algorithms that ensure the safe and reliable operation of a pack by monitoring cells and estimating their states, such as state-of-charge (SoC) and state-of-health (SoH) [9]. The SoC expresses the remaining cell energy compared to a fully charged cell and is therefore the 'fuel gauge' of EVs, whereas SoH expresses the cell reduced performance (capacity, power capability, etc.) compared to a pristine cell. In order to infer these unmeasurable states from the available measurements of voltage, current and temperature, a battery model must be solved in the BMS. In automotive applications, the model should accurately

describe behaviour under the wide range of operating conditions encountered, including high current, extreme temperatures and highly dynamic loads. In addition, diagnosis and prognosis of degradation in terms of capacity and power fade is an acute challenge.

Battery models used in current BMS technology usually consist of empirically-fitted equivalent electrical circuits that have an analogue current-voltage relation to the lithium-ion cell for which they have been parametrised. However, the limited validity range of such empirical models and their lack of physical significance make these model insufficient for the next generation of BMSs. In order to improve the performance of a battery pack, researchers are investigating the application of electrochemical models in the BMS [10], for example to enable electrochemical control of fast charging [11–14] or advanced health-conscious management algorithms [15]. This is a challenging research area both from the modelling and numerical solution perspective, but also the application perspective. Key challenges include reducing the computational cost of electrochemical models to enable their use in embedded applications and whether such models are observable and identifiable, and can be used for state estimation at both the cell and battery pack levels.

The objectives of this dissertation are to provide novel techniques to solve and use electrochemical models for advanced control and monitoring algorithms in next-generation BMSs. Therefore, this work is not about deriving fundamentally new battery models, but rather developing new algorithms to bring the benefits of electrochemical modelling to embedded applications. Specifically, this work focuses on the fast yet accurate solution of electrochemical models and their state estimation to enable electrochemistry-aware battery monitoring. Because the value of such approaches relies heavily upon the accuracy of these models, the trustworthy parametrisation of electrochemical models from experimental data is also investigated.

The remainder of this introductory chapter provides the necessary lithium-ion battery fundamentals and reviews the existing literature upon which this work is developed. An overview of the present work is then given, along with the organisation of the dissertation.

1.2 Background and literature review

1.2.1 Li-ion battery fundamentals

A battery is an electrochemical device that can store chemical energy and convert it into electrical energy to power a load. Perhaps surprisingly, the operating principle of modern electrochemical cells, including lithium-ion batteries, has not fundamentally changed since the invention of the voltaic pile by Alessandro Volta in 1800; only the cell components, namely the electrodes, separator and electrolyte, have been improved from metallic discs, paper and brine to more advanced materials.

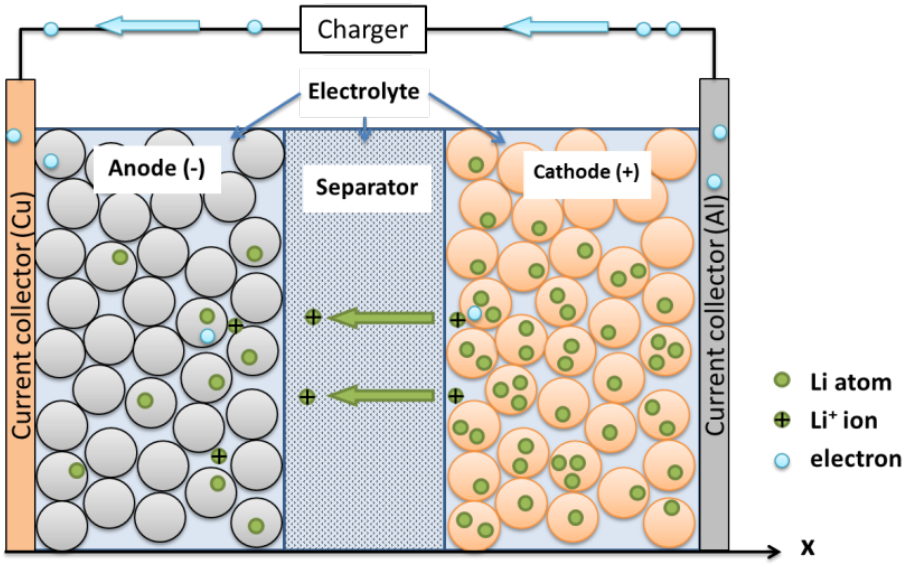

Fig. 1.1 Structure and operating principle of a lithium-ion cell.

As shown on Figure 1.1 a lithium-ion battery consists of two electrodes, a negative electrode (anode) and a positive electrode (cathode[1]), made of porous materials that can store lithium within their crystalline structure. These two electrodes are electronically-insulated from each other by a micro porous separator film. Electrodes and separator are soaked into an electrolyte solution that allows the passage of dissolved lithium ions from the anode to the cathode and *vice versa*. During battery discharge, lithium stored in the anode is de-inserted from the material and travels as lithium ions in the electrolyte through the separator to insert in the cathode active material. Simultaneously, electrons are forced to travel through the battery external circuit to balance charges giving rise to an electric current that powers a load. This process is reversible and an opposite mechanism occurs during battery charging.

A variety of cathode materials have been developed since the commercialisation of the first lithium-ion battery by Sony in 1999. Active materials used for the anode typically consists of graphitic carbons whereas the cathode can be made of various lithium metal oxides such as $LiCoO_2$ (LCO), $LiMn_2O_4$ (LMO), $LiFePO_4$ (LFP), $LiNiMnCoO_2$ (NMC), $LiNiCoAlO_2$ (NCA) [16]. Note that the name of the cathode material is commonly used to distinguish between different lithium-ion cell chemistries. The anode and cathode materials are adhered to metallic current collector sheets using a conductive binder. Micro porous polyethylene or polypropylene films with a thickness on the order of tens of microns are typically used as separator material. Commonly employed liquid electrolytes consist of highly concentrated solutions of lithium salts (*e.g.* $LiPF_6$) in a mixture of organic solvents such as propylene carbonate (PC), ethylene carbonate (EC), dimethyl carbonate (DMC), ethyl methyl carbonate (EMC) [16]. The electrochemical cell obtained by combining the anode, separator and cathode is usually rolled or stacked and assembled into a cylindrical case, a prismatic case or a pouch. The

[1]Note that we refer to anode and cathode when discharging as a convention for the negative and positive electrode

reader is referred to the literature such as [16] for further details on the design of lithium-ion batteries.

1.2.2 Battery modelling

Battery state estimation and control in current BMSs typically employs low-order empirical models, such as equivalent-circuit models (ECMs) [17–19], which are parametrised using time- [20, 21] or frequency-domain [22–24] experimental data. These ECMs consist of a network of resistors, capacitors or more advanced elements, such as the constant-phase element (CPE) [25, 23], which imitates the observed relation between current and voltage of a battery. These models have very low computational demands but are only valid within the narrow operating conditions in which they have been parametrised. Because the parameters of such models have little direct physical significance, broadening their validity range requires a large amount of experimental data under a wide range of operating conditions. Furthermore, these ECMs only relate current and voltage and have no prediction capabilities for internal electrochemical states of the battery.

Alternatively, physics-based models describing the cell thermodynamics, reaction kinetics and transport of lithium ions within the cell, are valid over a wide range of operating conditions and could be directly coupled to degradation models. Physics-based models have been widely used for battery design [26–29] but are usually too computationally intensive for the limited resources of an embedded BMS. The so-called pseudo two-dimensional (P2D) electrochemical model developed by John Newman and his colleagues at UC Berkeley [26, 28] is probably the most widely used lithium-ion battery model of this type. The model is built upon the porous electrode theory developed by Newman and Tiedemann [30] and is discussed extensively in [31]. The P2D electrochemical model is composed of a one-dimensional macro-scale model describing the evolution of lithium concentration and electric potential in the electrolyte across the anode,

separator and cathode, together with micro-scale models for the electrodes. The pseudo-second dimension arises from these coupled one-dimensional micro-scale models describing the solid-phase diffusion of lithium in the electrode porous active material. A detailed description of the P2D model equations and structure is given in Section 2.1. By modelling diffusion and kinetics limitations, the P2D model is able to accurately describe lithium-ion battery dynamics over a wide operating range [32]. Furthermore, the P2D model has been extended by numerous researchers to account for more physical phenomena over the last two decades, such as double-layer capacitance [33–35], thermal effects [36–43], or degradation side reactions [44–46]. The P2D electrochemical model therefore constitutes an ideal candidate for advanced control and monitoring algorithms for the next generation of BMSs. However, the computational cost of the P2D model is prohibitive in comparison to ECMs for embedded applications. A review of the literature on reduced order electrochemical models and their application for control and monitoring purposes is provided in the subsequent section.

1.2.3 Fast electrochemical modelling for BMSs

Several attempts at performing state estimation on simplified models derived from the P2D model have been reported in the literature. A common simplification, known as the single particle (SP) model [47, 48], assumes that each electrode can be represented by a unique solid-phase particle and neglects concentration gradients in the electrolyte. State estimation using the SP model and similar approximations has already been reported in the literature and includes the use of an extended Kalman filter (EKF) algorithm [49], or a backstepping PDE state estimator [50]. In [51], the EKF was applied to an averaged electrochemical model similar to the SP model to estimate SoC and critical concentration at the surface of the electrodes. However, these approaches are inherently limited due to the low current validity range of the SP model. Other approaches include state estimation

on reduced-order models derived from the P2D model. In [52, 53], Kalman filtering is performed on a reduced-order state variable model computed by residue grouping [54, 55] from transcendental transfer functions that approximate each equation of the P2D model assuming quasi-linear behaviour. In [56], the EKF is applied to a state space reduced-order model computed from the P2D model using a discrete-time realization algorithm [57–59]. However, the parameters of such reduced-order models may be difficult to interpret or have no direct physical meaning, which makes accounting for degradation effects difficult. Recent works have shown that using spectral numerical methods to discretise the P2D model, instead of the commonly used finite-difference method, requires far fewer discretisation nodes and thus results in significantly reduced model complexity, whilst maintaining accuracy and physical significance of parameters. Dao *et al.* used the Galerkin spectral method on sinusoidal basis functions to discretise the electrolyte diffusion equation [60], while Cai and White applied orthogonal collocation on finite elements to all the equations of the P2D model [61]. Orthogonal collocation enforced at zeros of Jacobi polynomials was also applied to the full P2D model in [62] and solved using Maple and DASSL solvers using cosine basis functions and more recently Chebyshev polynomial basis functions for improved convergence at high currents [14]. State estimation of the full P2D model solved using the approach discussed in [62] has recently been reported using the optimisation-based moving-horizon estimation technique [63] and a tethered particle filter algorithm[2] [64].

1.2.4 Model parameter estimation

The performance of model-based state estimation and control algorithms for lithium-ion batteries relies heavily on the accuracy of the underlying battery model. The reliable estimation of model parameters from experimental data therefore becomes crucial in such control applications. In the literature, the

[2]The P2D model used in [64] assumed the simplified parabolic profile approximation from [65] for the solid-phase diffusion model, therefore limiting its validity to relatively low currents.

parametrisation of lithium-ion battery models has been thoroughly investigated in the context of ECMs [66–69] due to their empirical nature; however, by comparison the parameter estimation of electrochemical models remains relatively unexplored. This is perhaps because electrochemical models have been originally used for fundamental understanding and design optimization studies of batteries, for which relative effects of model parameters on battery performance were more important than absolute parameter values. In recent years, the parameter estimation of electrochemical models (SP and P2D models) from experimental data has been increasingly investigated and remains to this date an active research topic driven by the need for better electrochemical model-based control algorithms and battery degradation prognostics.

The estimation of electrochemical model parameters usually involves finding a set (or a subset) of parameters that minimises the error between the measured and model predicted voltage (as well as temperature possibly) in the least-square sense for a given current input. This is however not a trivial task because electrochemical models contain a large number of parameters and are usually over-parametrised. The P2D model for instance typically contains about 28 parameters, excluding the OCP fitted functions and parameter temperature- and concentration-dependencies. In practice, the optimisation problem for identifying all these parameters is (i) extremely computationally intensive and (ii) often ill-conditioned because some parameters are unidentifiable, *i.e.* some parameters have very little influence on the voltage or temperature output but may have significant impact on internal states.

To overcome this computational burden, a common approach in the literature consists of only optimising for a subset of parameters assuming the remaining parameter values are known. In [70], a subset of five parameters was optimised for both the SP and P2D models based on constant-current data at several C-

rates[3]. Confidence intervals on these parameters were computed by deriving the Fisher-information matrix numerically[4]. Although most parameters were estimated with relatively narrow confidence intervals, the value of the anode solid-phase diffusivity was found to have no impact on the cell voltage. The approach was later extended to investigate degradation in LCO cells [72] by tracking changes in initial stoichiometries and active material losses with cycling. Speltino *et al.* [73] identified nine parameters of the SP model against constant-current discharge cycles featuring high intensity current pulses to excite the model dynamics. The identified parameters yielded good agreement between simulated and predicted voltage but the uncertainty on parameters was not evaluated. A parameter estimation of a P2D model reformulated using polynomial approximations was performed in [74, 75] to investigate battery degradation on five parameters originally, but later restricted to only two parameters (anode diffusivity and reaction rate constant) because of parameter unidentifiability. In addition, it was reported that Monte-Carlo simulations were required to compute accurate parameter confidence intervals. In contrast to the results reported in [70], only the anode diffusivity could be estimated with high confidence in [75].

These early results showed that the identifiability of electrochemical models is challenging even when only a small subset of parameters is considered and that this nonlinear optimisation problem features several local minima. The Levenberg–Marquardt [70, 72] and Gauss–Newton [74, 75] optimisation methods

[3]The C-rate refers to the current intensity that discharges a battery in one hour; for instance, a battery of 2.1 A h capacity is discharged at $1C$ under a 2.1 A current and at $2C$ under a 4.2 A current. This normalised current intensity allows comparisons between batteries of different capacities.

[4]The Fisher-information matrix F measures the information contained in the dataset on the unknown parameters and its inverse is often used as an approximate for the covariance matrix using the so-called Cramer–Rao lower bound [71]. Under the maximum likelihood estimation framework, it can be shown that the Fisher-information matrix is equal to the Hessian H of the cost function at the parameter estimate, which can be approximated by $\mathrm{H} = \mathrm{J}\mathrm{J}^{\mathsf{T}}$ with J the Jacobian of the cost function with respect to the parameters evaluated at the parameter estimate.

were used in these early studies[5]; however, such Jacobian-based methods may not be well suited for such optimisation problems because the algorithm will likely converge to a local minimum. Alternative optimisation techniques have later been investigated to deal with these identifiability issues including genetic [76, 32], homotopy [77] and particle swarm [78] optimisation algorithms. Although results in [77] showed good convergence behaviour on the four identified parameters, uncertainties on these estimates were not investigated and emulated 'experimental' data were used, therefore limiting conclusions with regard to identification from actual experimental data. Similarly in [78], only four parameters were identified with no quantification of uncertainty and different parameter estimates were found for charge and discharge data.

Forman *et al.* [76, 32] attempted to estimate all parameters of the P2D model, including all coefficients for the OCP fitting functions and concentration-dependency of the electrolyte conductivity. Despite the use of parallel processing and quasi-linearisation of algebraic constraints to increase the computational speed, the simultaneous estimation of these 88 parameters from dynamic drive cycle experimental data required about three weeks of computation. Confidence intervals computed based on the Fisher-information approach revealed that the cathode OCP function was generally identifiable compared to the corresponding OCP curve for the anode and that the concentration-dependency of electrolyte conductivity could not be identified. Only 11 parameters were deemed identifiable out of the 17 actual parameters of the P2D model considered, including the electrolyte and anode solid-phase diffusivities despite almost 300 % relative confidence intervals. The identification of all P2D model parameters (except OCP) was also later investigated using multi-objective optimization in [79] and a sequential identification procedure in [80].

[5] A gradient-free optimisation method was employed in [73] but the exact technique is not indicated.

In the aforementioned studies, either all parameters or a subset of parameters chosen by intuition were identified. In [81] however, the SP model parameters were divided into capacity- and resistance-related subsets and identified from different experimental datasets accordingly. Schmidt *et al.* [82] investigated the parametrisation of an improved SP model with thermal and electrolyte effects from voltage and temperature measurements. The identifiability of the 33 parameters considered (including the OCP function coefficients) was assessed by solving sensitivity equations alongside the model to infer parameter variances based on the Fisher-information matrix and systematically exclude unidentifiable parameters from the optimisation. Their study revealed that 11 to 27 parameters of the model were identifiable depending on the experimental dataset considered (low or high C-rate, constant or varying current and temperature). Interestingly, the case in which most parameters were considered identifiable (27 out of 33 parameters) corresponds to the experimental dataset with the largest maximum current ($16\,C$) and cell temperature variation ($62\,^{\circ}\mathrm{C}$), clearly suggesting the importance of informative experimental data for model identifiability. In a recent publication [83, 84], it is argued that accounting for parameter sensitivity in the identification algorithm can reduce the estimation error by an order of magnitude. However, this study only considered the identification of a small parameter subset of a simplified P2D model against emulated 'experimental' data under constant-current operation. In [85], different computational frameworks available for evaluating parameter variances and identifiability ranging from local Fisher-information to Monte-Carlo simulations are summarised.

Table 1.1 summarises the literature to date on the parameter estimation of the SP and P2D electrochemical models, and shows how many and which parameters were identified, the cell chemistry considered and the type of identification data used, constant current (CC), pulse current (PC) or drive cycle (DC). A short description of the different techniques employed to quantify parameter uncertainty

is also given. Results reported in the previous literature were mainly based on *ad hoc* and unprincipled approaches, which highlight the importance of using a set of experiments that is sufficiently informative for the parameters under investigation and accounting for parameter identifiability in the estimation algorithm.

1.3 Overview of the present work

Chapter 2 of this dissertation introduces the mathematical models used throughout this thesis, namely the SP [47, 48] and P2D [26, 28] electrochemical models. The partial-differential equations (PDEs) constituting the P2D model are discussed in details and the interdependencies between these equations are scrutinized to reveal the differential-algebraic nature of the P2D model. The SP model is naturally introduced as a simplification to the P2D model. Specifically, we show how the SP model retains some similarities with the P2D model but not its differential-algebraic nature, which makes its solution and use within control algorithms much more convenient. Finally, a short overview of the literature on the coupling of thermal and electrochemical models is presented and the bulk thermal model approximation used in this work is introduced.

The fast solution of the P2D electrochemical model developed in this work is presented in Chapter 3. Similar to Northrop *et al.* [86], an advanced spectral numerical method, so-called *orthogonal collocation*, is used to spatially discretise the P2D model. However, unlike the approach in [86], the algorithm presented here is more flexible because the whole P2D model is discretised using orthogonal collocation rather than using different techniques for the micro-scale solid-phase diffusion model, namely a low-order polynomial approximation [87] for low C-rates and a finite-difference method at high C-rates [88]. The computational domain decomposition required to solve the P2D model and the practical model implementation in MATLAB® are also thoroughly discussed. The accuracy and

Table 1.1 Summary of the literature on the parameter estimation of electrochemical lithium-ion battery models.

Ref.	Model	#	Identified parameters	Cell chem.	Identification Data	Uncertainty quantification
[70]	SP/P2D	5	$D_{\mathrm{s},3}$, k_i, x_i^0	LCO	CC	Local Fisher-info.
[72]	SP/P2D	8	$D_{\mathrm{s},3}$, k_i, x_i^0, w_i	LCO	CC	Local Fisher-info.
[73]	SP	9	$c_{\mathrm{s},i}^{\max}$, $D_{\mathrm{s},i}$, $a_{\mathrm{s},i}$, A, R_{ctc}, k	LCO	CC/PC	n/a
[74]	P2D	5 (2)	$D_{\mathrm{s},i}$, k_i, D_{e} ($D_{\mathrm{s},1}$, k_1)	n/a	CC	χ-square statistics, F-statistics and Monte-Carlo.
[82]	SP	33	all parameters, except geometry	n/a	CC/PC	Local Fisher-info.
[75]	P2D	5	$D_{\mathrm{s},i}$, k_i, D_{e}	n/a	CC	χ-square statistics, F-statistics, Monte-Carlo.
[76]	P2D	88	all parameters.	LFP	DC	Eigenvalues of Hessian as identifiability criteria.
[32]	P2D	88	all parameters.	LFP	DC	Local Fisher-info.
[81]	SP[1]	6	x_i^0, $\epsilon_{\mathrm{s},i}$, $D_{\mathrm{s},i}$	n/a	CC	n/a
[79]	P2D[2]	25	all parameters, except OCV.	LFP LCO	PC	n/a
[80]	P2D[2]	18	all, except OCV.	NMC	CC	One-at-a-time sensitivity (ANOVA).
[77]	P2D	4	$\epsilon_{\mathrm{s},2}$, t_+, σ_1, $c_{\mathrm{e}}^{\mathrm{avg}}$	n/a	CC	n/a
[85]	P2D	8	$D_{\mathrm{s},i}$, D_{e}, k_i, b, R_{ctc}, t_+	LMO	CC	Local Fisher-info, Monte-Carlo.
[78]	P2D[3]	4	$D_{\mathrm{s},i}$, k_i	LCO	CC	n/a
[83]	P2D[3]	8	$D_{\mathrm{s},i}$, k_i, x_i^0, S_i	LCO	CC	Local sensitivity based on Jacobian.
[84]	P2D[3]	8	$D_{\mathrm{s},i}$, k_i, x_i^0, S_i	LCO LMO LFP	CC	Local sensitivity based on Jacobian.

#: number of identified parameters.
CC: Constant current, PC: Pulse current, DC: Drive cycle.
[1]Improved SP model accounting for electrolyte effects and OCV hysteresis.
[2]The P2D model was coupled to a 1D thermal model.
[3]Simplified P2D model.

performance of this efficient model implementation are then compared to a high-fidelity finite-element model implemented in COMSOL®.

The fast implementation of the P2D model developed in Chapter 3 enables the state estimation of the full P2D model using a modified extended Kalman filter (EKF) algorithm for DAEs. Chapter 4 first presents the theory underlying the modified Kalman filtering algorithm developed in the present work. The convergence of state estimates (concentration-based SoC, electrolyte concentration, etc.) is then investigated using numerical experiments. A graphical abstract of the approach to the P2D model state estimation originally published in [2] is shown in Figure 1.2.

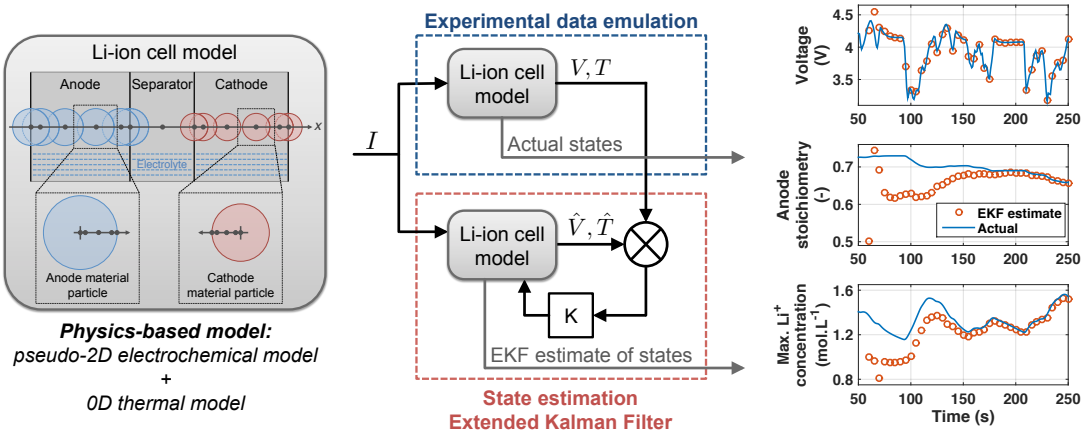

Fig. 1.2 Graphical abstract of the P2D model state estimation approach [2].

In the present work, the fast solution and state estimation of the P2D model is investigated based on model parameters for an LCO cell from the literature. However, the accurate identification of model parameters is key to enabling the use of electrochemical models in real-life applications for the control and monitoring of commercial cells. The existing literature on parameter estimation shows that standard optimisation techniques fail in practice at estimating reliable parameters due to unidentifiability issues. In Chapter 5, we attempt a rather different approach compared to the literature and investigate the SP model identifiability in principle by inspecting the model equations. The insightful results obtained

by performing this *structural identifiability* analysis are then used to guide the parameter estimation of the SP model from frequency-domain experimental data obtained by electrochemical impedance spectroscopy (EIS).

Finally, Chapter 6 summarises the outcomes and contributions of this work and proposes possible directions for future research.

Chapter 2

Li-ion battery physics-based models

This chapter discusses the different lithium-ion battery mathematical models used throughout this dissertation. The subsequent two sections are devoted to first-principle electrochemical models describing mass transport, thermodynamics and reaction kinetics in lithium-ion cells. Section 2.1 gives a detailed explanation of the so-called pseudo two-dimensional (P2D) model developed by Newman and his co-workers [26, 28]. In Section 2.2 a simplification of the P2D model is introduced, which neglects electrolyte dynamics. This simplified model is commonly referred to as the single-particle (SP) model in the literature and is only valid for low current operation. However, the SP model has proven to be an ideal 'test-case' model prior to developing state and parameter estimation algorithms based on the P2D model, due to its simpler albeit similar structure. Although the P2D and SP models do not account for temperature effects *per se*, these models can relatively easily be coupled to thermal models due to their first-principle nature. It has been shown in the literature through extensive experimental testing that temperature has indeed a substantial effect on battery performance [89] and degradation [90].

Section 2.3 discusses the thermal model used in this dissertation and its coupling to the P2D electrochemical model.

2.1 The pseudo-two dimensional model

This section thoroughly discusses the P2D electrochemical model and its mathematical structure. First, the multi-scale nature of the model is explained along with the corresponding model computational domains and variables of interest in section 2.1.1. In subsequent sections, the model equations governing transport of lithium (section 2.1.2), electrode kinetics (section 2.1.3) and thermodynamics of the cell (section 2.1.4) are introduced. Finally, the dependencies between these model equations are highlighted in section 2.1.5 to reveal the differential-algebraic nature of the model. In particular, the flowchart in figure 2.3 shows graphically these interdependencies between model equations and may be helpful to the reader throughout section 2.1 in comprehending the overall P2D model structure.

2.1.1 A multi-scale model

The P2D electrochemical model is a multi-scale continuum model describing the electrochemical processes occurring within the cell at macro- and micro-scale levels. The model describes the transport of lithium ions, the cell thermodynamics and the reaction kinetics at the electrode/electrolyte interfaces. As discussed in Section 1.2.1, a lithium-ion cell consists of two porous electrodes composed of an active material that can store lithium intercalated in the solid material, and a separator that allows the passage of ions but not electrons. The porous electrodes and the separator are soaked in an electrolyte, which allows the transport of ions. During discharge, lithium stored in the anode is de-inserted from the active material and released as ions in the electrolyte. Driven by diffusion (concentration gradient) and migration (electric potential gradient), lithium ions travel through

the separator to the cathode where they are inserted in the lattice of the cathode active material. Simultaneously, electrons travel from the anode to the cathode through the external circuit, powering a load, to ensure electro-neutrality. This process is reversed during battery charging.

The multiple scale nature of the P2D model arises because the transport of lithium is modelled at two different length scales. On the one hand, lithium transport in the electrolyte occurs at the macro-scale across the cell sandwich *anode–separator–cathode* of thickness on the order of a few hundreds of microns. On the other hand, diffusion of lithium ions in the active material of each electrode occurs at the micro-scale level across a typical length in the order of a few microns. From a mathematical modelling perspective, most of the model differential equations are solved on a macro-scale unidimensional domain spanning the cell sandwich, except the diffusion equations describing the micro-scale diffusion in the active material of each electrode, which are solved in spherical particles, as shown on figure 2.1. The radius of these spherical particles represents the typical length that lithium ions must diffuse in the porous active material of the electrode, *i.e.* the size of the material pores. A unidimensional Fickian diffusion equation is solved in each of these micro-scale particles distributed along the macro-scale cell sandwich in each electrode, resulting in a pseudo-second dimension, hence the *pseudo-two dimensional* nature of the model.

The computational domains of the P2D model are shown on the cell schematics in figure 2.1. The macro-scale domain of the model spans across the cell thickness L along the x-dimension and is divided into three sub-domains: anode, separator and cathode, denoted Ω_1, Ω_2 and Ω_3 respectively. In each of these domains, two phases are considered, the solid phase and the electrolyte phase, which are treated as superimposed continua using porous electrode theory [30], therefore neglecting the exact micro-structure of the electrodes. Unidimensional micro-scale domains Ω_1^{r} and Ω_3^{r} are considered at each point of the anode domain Ω_1 and cathode

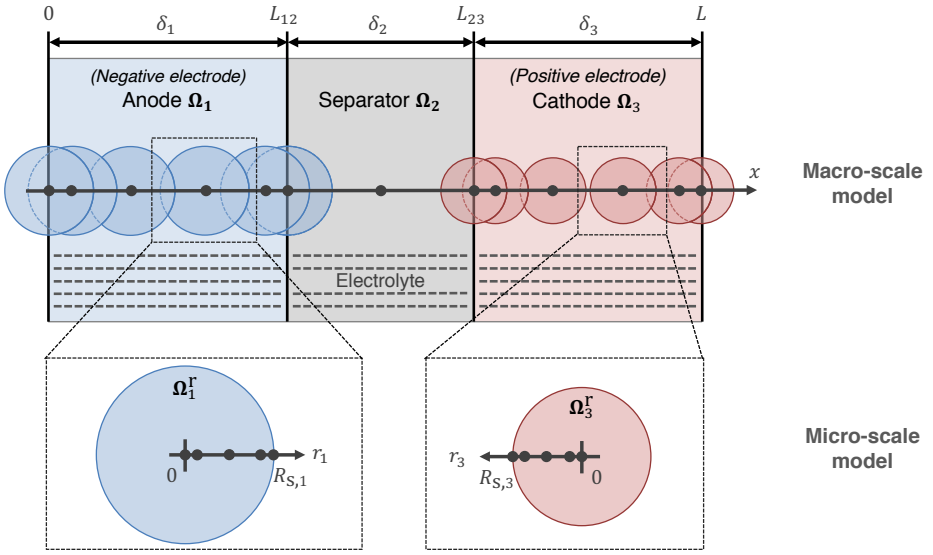

Fig. 2.1 Schematic of the cell computational domains [2].

domain Ω_3. These micro-scale domains are the spherical particles parametrised by the spherical r-coordinate.

The P2D model consists of a set of partial differential equations (PDEs) and algebraic constraints governing the evolution of lithium concentration and electric potential within the cell. The dependent variables are solid-phase concentration $c_{\mathrm{s}}(r, x, t)$, electrolyte concentration $c_{\mathrm{e}}(x, t)$, electric potential at the surface of the solid-phase particles $\phi_{\mathrm{s}}(x, t)$, electric potential in the electrolyte $\phi_{\mathrm{e}}(x, t)$ and reaction rate $j(x, t)$, which expresses the amount of lithium exchanged between the solid-phase and the electrolyte, coupling the micro- and macro-scale model equations. One can note that the solid-phase electric potential $\phi_{\mathrm{s}}(x, t)$ is considered at the surface of the solid-phase spherical particles where the interfacial reaction for lithium intercalation/de-intercalation occurs, *i.e.* at the interface between the electrode insertion material and the electrolyte. The independent variables are time t, the x-coordinate across the cell thickness and the spherical r-coordinate in the solid-phase particles.

The input of the model is the applied current I from which the applied current density $i_{\text{app}} = I/A$ is calculated knowing the electrode surface area A. Note that the surface areas of each electrode usually differ, but for simplicity have been assumed equal throughout this work. At any point within the cell, the current is either carried by electrons in the electrode material or by ions in the electrolyte. The local fractions of current density carried by the ions in electrolyte i_{e} and electrons in the solid-phase i_{s} are related to the total current density passing through the cell i_{app} by the Kirchhoff's law

$$i_{\text{s}} + i_{\text{e}} = i_{\text{app}}. \tag{2.1}$$

Since the separator is electronically insulating, the current density is carried only by ions in the separator domain Ω_2 and $i_{\text{e}} = i_{\text{app}}$. At any point in the macro-scale domain, the local reaction rate j is equal to the divergence of the electrolyte current density i_{e} according to

$$\frac{\partial i_{\text{e}}}{\partial x} = a_{\text{s}} \mathcal{F} j. \tag{2.2}$$

where the specific interfacial area $a_{\text{s}} = 3\epsilon_{\text{s}}/R_{\text{s}}$ is the surface area of electrode per unit volume of porous electrode and $\mathcal{F}$ denotes Faraday's constant. The output of the model is the cell terminal voltage V, which is equal to the difference between the solid-phase potential at the cathode current collector and that at the anode current-collector, minus the ohmic drop due to the contact resistance R_{ctc} at the current collector/electrode interfaces.

2.1.2 Transport of lithium

Lithium diffusion in the solid-phase

The transport of lithium in each spherical particle of electrode active material is described by the linear Fickian diffusion equation in spherical coordinates

$$\frac{\partial c_\mathrm{s}}{\partial t} = \frac{1}{r^2}\frac{\partial}{\partial r}\left(r^2 D_\mathrm{s}\frac{\partial c_\mathrm{s}}{\partial r}\right), \tag{2.3}$$

By symmetry considerations, this equation is subject to a homogeneous Neumann boundary condition at the centre of the particle for $r = 0$

$$\left.\frac{\partial c_\mathrm{s}}{\partial r}\right|_{r=0} = 0. \tag{2.4}$$

At the particle surface for $r = R_\mathrm{s}$, the flux of lithium going in or out of the particle due to the electrode/electrolyte interfacial reaction is modelled by the inhomogeneous Neumann boundary condition

$$D_\mathrm{s}\left.\frac{\partial c_\mathrm{s}}{\partial r}\right|_{r=R_\mathrm{s}} = -j, \tag{2.5}$$

where the reaction rate j in $\mathrm{mol\,m^{-2}\,s^{-1}}$ expresses the flux of lithium exchanged between the solid-phase and the electrolyte. The reaction rate j is the dependent variable coupling the micro-scale particle model and the macro-scale model and therefore varies along the electrode thickness depending on the local overpotential through the Butler–Volmer kinetics equation discussed in Section 2.1.3.

Lithium transport in the electrolyte

Typical electrolytic solutions for commercial lithium-ion batteries consist of a binary salt (*e.g.* $\mathrm{LiPF_6}$) dissolved in an organic solvent (*e.g.* PC/EC/DMC) and are therefore composed of three species: cations, anions and solvent molecules. On the one hand, the Guggenheim relation $z_+\nu_+ + z_-\nu_- = 0$ constrains the anion

and cation charges because the salt charges must balance when isolated from the solution; on the other hand, the solution is locally electro-neutral $z_+c_+ + z_-c_- = 0$ because the volume elements considered are large in comparison to the Debye length [4]. The combination of the Guggenheim and electro-neutrality conditions dictates that the three species concentrations are not independent. Therefore, the neutral-salt formula unit concentration $c = c_+/\nu_+ = c_-/\nu_-$ is sufficient to fully describe species transport in the liquid-phase. Because $\nu_+ = \nu_- = 1$, so that $c = c_+ = c_-$, for typical lithium-ion battery electrolytes, we denote subsequently c_e the electrolyte lithium concentration and use it in the model equations, rather than c_+ for notation consistency.

In the P2D model, electrolyte and solid-phase are treated as two superimposed continua using the porous electrode theory [30] in order to avoid considering the details of the micro-structure of the porous electrodes. Volume-averaged quantities are considered on the macro-scale level assuming volume-elements that are much larger that the microscopic pore size of the active material, but small enough that macroscopic variations of these quantities can be neglected within each element. More specifically, the lithium ion concentration considered is actually the volume-averaged concentration $\epsilon_\mathrm{e} c_\mathrm{e}$ where c_e is the lithium ion concentration in the electrolyte solution and ϵ_e is the volume fraction of the solution-phase in the domain. Therefore, the evolution of lithium concentration in the electrolyte is governed by the following diffusion equation

$$\epsilon_\mathrm{e} \frac{\partial c_\mathrm{e}}{\partial t} = \frac{\partial}{\partial x}\left(\epsilon_\mathrm{e} D_\mathrm{e}^\mathrm{eff}\left(c_\mathrm{e}\right) \frac{\partial c_\mathrm{e}}{\partial x}\right) + a_\mathrm{s}\left(1 - t_+\right) j, \tag{2.6}$$

subject to homogeneous Neumann boundary conditions (zero flux) at $x = 0$ and $x = L$, since no lithium ion can go through the current collectors. The first term on the right-hand side is the diffusion term, with $D_\mathrm{e}^\mathrm{eff} = D_\mathrm{e}\epsilon_\mathrm{e}^b$ the effective Fickian diffusivity. The effective diffusivity is an empirically corrected value of

the diffusivity D_e, which accounts for the tortuosity of the porous electrode using the so-called Bruggeman exponent b [26, 28, 91]. The electrolyte diffusivity is highly dependent on the electrolyte concentration because of excluded-volume effects in concentrated solutions as shown by equation (29) in [4] and reported experimentally in [92]. The second term on the right-hand side is the source term that accounts for the local consumption/production of lithium ions due to insertion/de-insertion in the active material of electrodes. The cation transference number with respect to the solvent velocity t_+ expresses the fraction of current carried by cations in the electrolyte.

2.1.3 Electrode kinetics

As previously mentioned, the reaction rate j is the dependent variable that couples the micro- and macro-scale models together. In the electrolyte diffusion equation (2.6) the reaction rate acts as a distributed source/sink term across each electrode, while in the micro-scale solid-phase diffusion model, it appears in the boundary condition (2.5) at the surface of each particle. The intercalation/de-intercalation of lithium is a heterogeneous charge transfer reaction occurring at the electrode/electrolyte interface, *i.e.* at the surface of each electrode particle, according to the half-reactions [93]

$$\mathrm{MO_y} + \mathrm{Li^+} + \mathrm{e^-} \leftrightharpoons \mathrm{LiMO_y} \quad \text{in the cathode} \tag{2.7}$$

$$\mathrm{LiC_6} \leftrightharpoons \mathrm{Li^+} + \mathrm{e^-} + \mathrm{C_6} \quad \text{in the anode} \tag{2.8}$$

were MO denotes the cathode metal oxide. The rate of this charge transfer reaction is given by the so-called Butler-Volmer kinetics equation [26]

$$j = \frac{i_0}{\mathcal{F}} \left[\exp\left(\frac{\alpha_a \mathcal{F}}{RT} \eta \right) - \exp\left(\frac{-\alpha_c \mathcal{F}}{RT} \eta \right) \right]. \tag{2.9}$$

The surface overpotential η that drives this Faradaic process is the difference between the electrode surface potential and the equilibrium potential. The charge transfer coefficients α_a and α_c in the Butler-Volmer equation express the symmetry of the anodic and cathodic Faradaic reactions. The exchange current density i_0 depends on the products and reactants concentrations according to

$$i_0 = k\mathcal{F}\left(c_s^{max} - c_s^{surf}\right)^{\alpha_a}\left(c_s^{surf}\right)^{\alpha_c}\left(c_e\right)^{\alpha_a} \tag{2.10}$$

where c_s^{max} is the maximal theoretical lithium concentration in the active material and c_s^{surf} is the active material surface concentration.

2.1.4 Equilibrium potential and overpotential

The overpotential η in (2.9) is the departure of the local electric potential at the surface of the electrode from the equilibrium potential U. The surface overpotential is given by the relation

$$\eta = \phi_s - \phi_e - U(x_s^{surf}) \tag{2.11}$$

with ϕ_s the solid-phase surface potential, ϕ_e the electrolyte potential and U the equilibrium potential as a function of the surface stoichiometry $x_s^{surf} = c_s^{surf}/c_s^{max}$.

Open-circuit potential

The equilibrium potential of an electrode, also referred to as *open-circuit potential* (OCP), is the potential of the electrode at rest when no current is drawn. The OCP of an electrode is highly dependent on lithium concentration in the active material. In electrochemistry, the variation of equilibrium potential of an electrode with active species composition is usually modelled using the well-known Nernst equation. However, the simple Nernst equation cannot accurately describe the OCP of lithium-ion porous electrodes due to the complexity of these active materials. Instead, the electrode OCP as a function of surface stoichiometry x_s^{surf} is

measured using a three-electrode experimental setup, where the reference electrode allows measuring the anode and cathode potential separately. In commercial cells, such a three-electrode configuration is usually not possible, but a minimally invasive technique using a wire reference electrode inserted into a commercial pouch cell has been reported recently in [94]. A model describing the OCP *vs* stoichiometry is then obtained by fitting experimental OCP data to some chosen mathematical functions, e.g. polynomial and rational functions [45], spline functions [95], etc. or some more advanced first-principle Nernst-like equations [96].

In addition, lithium-ion batteries usually exhibit a voltage *hysteresis* effect, *i.e.* the electrode voltage does not relax to the same open-circuit value after charge or discharge. This hysteresis behaviour has been observed for most electrode active materials used in lithium-ion batteries including graphite [97], LMO [98, 99], LCO [100], LFP [101] and NMC [96] and can result in significant SoC estimation inaccuracies [102]. Although hysteresis effects have not been addressed in the present work, possible modelling approaches using empirical differential equations for the hysteresis voltage have been reported in the literature [103, 102].

Solid-phase potential

The solid phase potential at the surface of the particles is governed by Ohm's law

$$\frac{i_{\mathrm{s}}}{\sigma^{\mathrm{eff}}} = -\frac{\partial \phi_{\mathrm{s}}}{\partial x}. \tag{2.12}$$

The effective conductivity $\sigma^{\mathrm{eff}} = \sigma \epsilon_{\mathrm{s}}^{b}$ of the composite material constituting the electrode is approximated using an empirical Bruggeman exponent b, similar to the effective electrolyte diffusivity in Section 2.1.2.

Electrolyte potential

Equation (2.13) governing the electrolyte potential ϕ_e — commonly referred to as the MacInnes' equation in the literature — is a modified Ohm's law that accounts for a 'diffusion overpotential' induced by local composition variations in the electrolytic solution.

$$\frac{i_e}{\kappa^{\text{eff}}(c_e)} = -\frac{\partial \phi_e}{\partial x} + \frac{2(1-t_+)RT}{\mathcal{F}} \frac{\chi}{c_T \bar{V}_0} \frac{\partial \ln c_e}{\partial x} \tag{2.13}$$

The left-hand side and the first term on the right-hand side correspond to the usual Ohm's law for a solution of concentration-dependent effective ionic conductivity $\kappa^{\text{eff}} = \kappa \epsilon_e^b$. The second term on the right is the overpotential induced by variations of species concentration in the electrolyte. The thermodynamic factor χ, which relates the electrolyte chemical potential to the electrolyte concentration, and the solute-volume effect factor $c_T \bar{V}_0$ arise from the concentrated-solution transport theory [31] because of the dependency of electrolyte density on composition [104, 4]. In most literature on lithium-ion battery modelling including [26, 28], the approximation $\chi / \left(c_T \bar{V}_0\right) = 1$ is usually made because the solvent concentration is considered to be weakly dependent on electrolyte concentration and probably also because of a lack of experimental data. This assumption is made subsequently in the present dissertation and the factor $\chi / \left(c_T \bar{V}_0\right)$ will be omitted from (2.13).

A discrepancy regarding equation (2.13) in the literature has been reported recently in [105]. In most publications [41, 106–108, 10, 109] the pre-factor $2(1-t_+)$ is used whereas in others [105, 110, 111, 2] the pre-factor $(1-2t_+)$ is employed in the MacInnes' equation. This confusion may arise from the two possible formalisms used to derive the MacInnes' equation [4]. On the one hand, the pre-factor $(1-2t_+)$ arises naturally in the equation derived from the dilute-solution theory using Nernst–Planck formalism, where species-species interactions in the electrolyte are neglected. On the other hand, the pre-factor $2(1-t_+)$ arises from

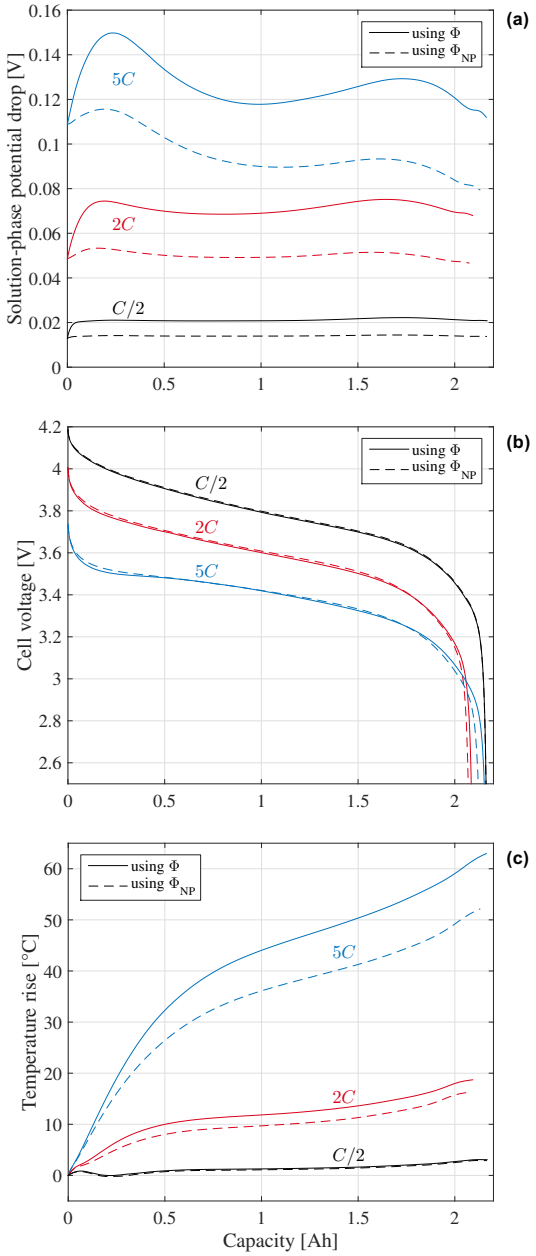

Fig. 2.2 Comparison between (a) solution-phase potential drop across the cell, (b) terminal cell voltage, and (c) temperature rise predicted by the P2D model in the limit of infinitely dilute solution using the Nernst–Planck potential Φ_{NP} and the potential defined in the Onsager–Stefan–Maxwell theory Φ as solution potential [4].

the concentrated-solution theory based on the Onsager–Stefan–Maxwell formalism. However, the electric potential defined in the Nernst–Planck theory is a theoretical construct compared to the potential defined with respect to a reference electrode in

the Onsager–Stefan–Maxwell theory. When the electrolyte potentials are defined consistently, both theories agree and the most thermodynamically meaningful pre-factor to use is $2(1-t_+)$. Detailed derivations of the MacInnes' equation using the dilute-solution theory (Nernst–Planck) and the concentrated-solution theory (Onsager–Stefan–Maxwell) are given in [4].

Figure 2.2 shows comparisons between the cell voltage, electrolyte potential drop across the cell, and temperature rise predicted by the P2D model assuming infinitely dilute-solution using the fictitious Nernst–Planck potential (denoted Φ_{NP}) and the potential arising from Onsager–Stefan–Maxwell theory (denoted Φ). Although the impact of using Φ_{NP} instead of Φ as electrolyte potential is small on the cell terminal voltage even at high C-rates (see figure 2.2b), it has a significant impact on the predicted electrolyte potential drop across the cell as shown on figure 2.2a. The discrepancy becomes particularly acute when predicting temperature rise (figure 2.2c), because reaction and ionic ohmic heat generation contributions strongly depend on the electrolyte potential.

2.1.5 A differential-algebraic problem

The P2D model consists of a set of coupled partial-differential equations (PDEs) in time and space and spatially distributed algebraic constraints, which can be cast into a semi-explicit system of differential-algebraic equations (DAEs) given in the form,

$$\dot{\mathbf{x}} = \mathbf{f}(\mathbf{x}, \mathbf{z}, u) \tag{2.14}$$

$$\mathbf{0} = \mathbf{g}(\mathbf{x}, \mathbf{z}, u) \tag{2.15}$$

where $\mathbf{f}$ and $\mathbf{g}$ are vector-valued functions (possibly nonlinear) of the state variables $\mathbf{x}, \mathbf{z}$ and some external input variable u. This system of DAEs is referred to as 'semi-explicit' because it consists of clearly distinguishable differential equations (2.14)

and algebraic equations (2.15) or constraints. Throughout this work and following common control theory practices, a state variable is viewed as a variable governed by the model equations and describing the state of the studied system at any instant. Specifically, state variables fully describe the system state at any time t_k and are sufficient to determine the system state at any future time t_{k+1} assuming that any external input u acting on the system between t_k and t_{k+1} is also known. In the semi-explicit DAEs system given by (2.14)–(2.15), the state variables can be divided into differential variables $\mathbf{x}$ whose time derivatives $\dot{\mathbf{x}}$ appear in the model equations, and algebraic variables $\mathbf{z}$ whose time derivatives do not appear in the DAEs. The remainder of this section qualitatively discusses which dependent variables of the P2D model equations are retained as differential and algebraic state variables. The semi-explicit DAEs system arising from the spatially discretised P2D model (3.80)–(3.81) is discussed in more details in section 3.3.

The micro-scale diffusion equation (2.3) and the macro-scale electrolyte transport equation (2.6) are both parabolic PDEs in time and space with an accumulation term (time derivative $\partial/\partial t$). By considering each of these equations with their respective two Neumann boundary conditions and known initial conditions (initial concentration profiles), these two initial-boundary value problems (IBVPs) have a unique solution. The accumulation term in these equations means that the solid-phase concentration and electrolyte concentration profiles are differential state variables of the P2D model.

The MacInnes' equation (2.13) describing the electrolyte potential and Ohm's law (2.12) governing the solid-phase surface potential are both first-order ordinary differential equations (ODEs) in space. Unlike the diffusion equations previously discussed, these equations do not include an accumulation term; therefore the electrolyte and solid-phase surface potentials ϕ_e and ϕ_s respectively are not differential state variables of the P2D model. Although the electric potentials ϕ_e and ϕ_s could be considered as algebraic state variables, the subsequent discussion

shows that this is not necessary and the reaction rate j and the solid-phase electric potential at the current collectors ϕ_s^{cc} are preferred as algebraic state variables in the present work. Equations (2.13) and (2.12) do not have a unique solution because electric potential must be defined relative to a reference potential. In mathematical terms, this means that electrolyte and solid-phase surface potential profiles are uniquely defined up to a constant of integration. To resolve this indetermination an arbitrary reference electric potential must be chosen without loss of generality. In the present work, the electrolyte potential at the cathode current collector was used as a reference potential and set to zero $\phi_e(x = L, t) = 0$, thus uniquely defining the potential profile in the electrolyte.

The indetermination problem remains nonetheless for the solid-phase surface potential profiles in both the anode and cathode. Although the potential gradients $\partial\phi_s/\partial x$ are implicitly known at the domain boundaries because the solid-phase current fraction i_s is equal to i_{app} at the current-collector/electrode interface and zero at the electrode interface, this does not determine the constant of integration in the anode and cathode. To overcome this lack of a boundary condition, we introduce the change of variable $\tilde{\phi}_s = \phi_s - \phi_s^{cc}$ where ϕ_s^{cc} denotes the value of the solid-phase surface potential at the current-collector in each electrode. Clearly, $\tilde{\phi}_s$ is still governed by Ohm's law (2.12), but the value of $\tilde{\phi}_s$ at each current collector is now equal to zero and $\tilde{\phi}_s$ is uniquely defined. The unknown values of the potential at the current collectors ϕ_s^{cc} in both electrodes are determined using a constraint on the integral of the reaction rate j over each electrode thickness discussed subsequently.

As previously mentioned, the reaction rate j in each electrode is related to the divergence of the electrolyte current density i_e by (2.2). Alternatively, the electrolyte current density can be expressed as a function of the integral of the reaction rate over the electrode thickness, up to a constant of integration C_i,

according to

$$i_{\mathrm{e}}(x,t) = a_{\mathrm{s}}\mathcal{F}\int_{x'=0}^{x} j(x',t)\,dx' + C_1 \quad \text{for} \quad x \in \Omega_1, \tag{2.16}$$

and

$$i_{\mathrm{e}}(x,t) = a_{\mathrm{s}}\mathcal{F}\int_{x'=L_{23}}^{x} j(x',t)\,dx' + C_3 \quad \text{for} \quad x \in \Omega_3, \tag{2.17}$$

in the anode and cathode respectively. In the anode, the electrolyte current density is zero at the current collector for $x = 0$; hence the constant of integration must be equal to zero. The solid-phase current density i_{s} vanishes to zero at the electrode/separator interface because the separator is electronically insulating; therefore according to (2.1) the electrolyte current density i_{e} is equal to the applied current density i_{app} at the electrode/separator interface for $x = L_{12}$. Evaluating (2.16) at $x = L_{12}$ the following constraint on the reaction rate is obtained in the anode domain

$$i_{\mathrm{app}}(t) = a_{\mathrm{s}}\mathcal{F}\int_{x=0}^{L_{12}} j(x,t)\,dx \quad \text{for} \quad x \in \Omega_1. \tag{2.18}$$

By recognising that $i_{\mathrm{e}}(L_{23},t) = i_{\mathrm{app}}$ and $i_{\mathrm{e}}(L) = 0$, a similar relation for the cathode is given by

$$-i_{\mathrm{app}}(t) = a_{\mathrm{s}}\mathcal{F}\int_{x=L_{23}}^{L} j(x,t)\,dx \quad \text{for} \quad x \in \Omega_3. \tag{2.19}$$

These constraints are merely charge conservation conditions, which state that the total flux of ionic charges exchanged at the surface of all particles in an electrode must be equal to the flux of electronic charges going through the external load, namely the applied current density i_{app}. Although (2.18) and (2.19) do not seem to involve the solid-phase potential ϕ_{s}, these constraints can be used to determine the unknown value of the solid-phase potential at the current collector $\phi_{\mathrm{s}}^{\mathrm{cc}}$ in each electrode. Indeed, the reaction rate is given as a function of overpotential by the Butler–Volmer equation (2.9) and in the expression for the overpotential (2.11) all

the variables are fully determined by the model equations except for the current collector solid-phase potential ϕ_s^{cc}. Therefore, the constraints on the reaction rate (2.18) and (2.19) can be interpreted as constraints on ϕ_s^{cc}. Note that using this approach, the values of ϕ_s^{cc} in the cathode and the anode become algebraic state variables of the model and the cell terminal voltage is conveniently given by the measurement equation $V = \phi_{s,3}^{cc} - \phi_{s,1}^{cc} - R_{ctc} i_{app}$, where $-R_{ctc} i_{app}$ is the ohmic drop caused by the contact resistance R_{ctc} at the current-collector/electrode interfaces, which is usually given in its normalised form in $\Omega\,\mathrm{cm}^2$.

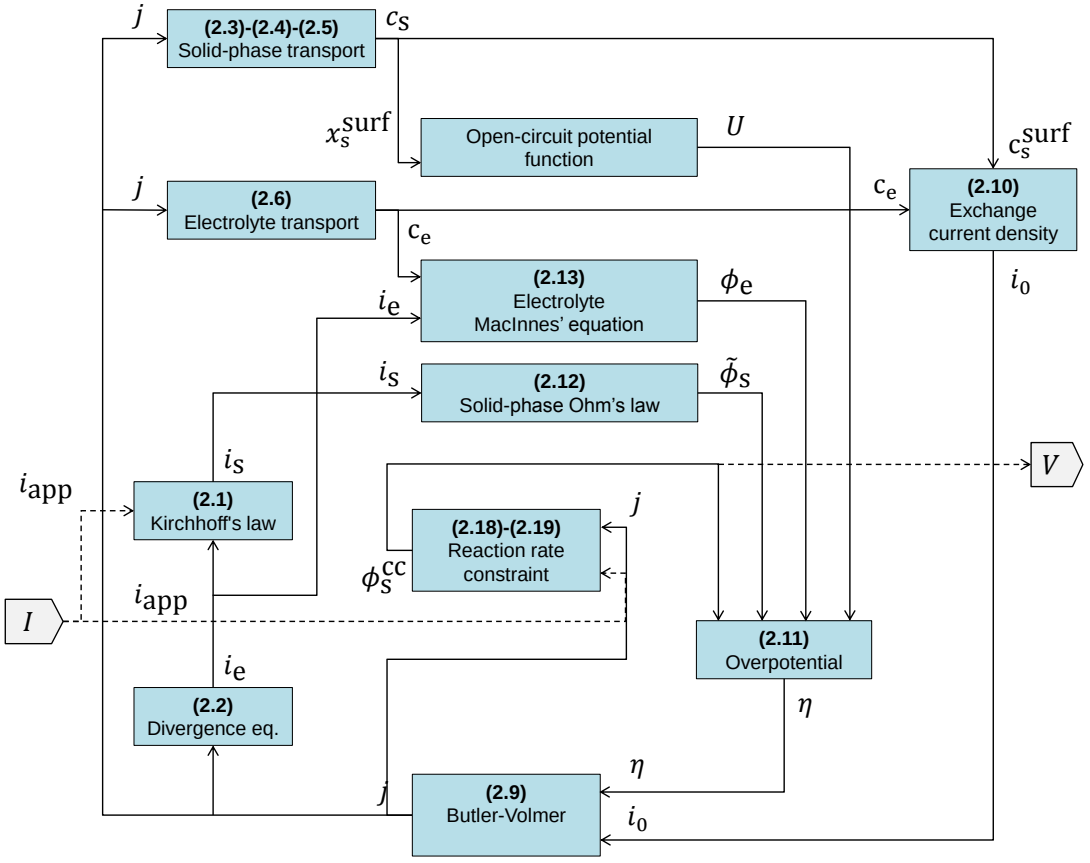

Fig. 2.3 Block diagram showing the interdependencies of the P2D model equations, dependent variables and input/output (dashed lines).

The Butler–Volmer equation (2.9) combined with (2.10) is not a differential equation since no derivative is involved, but instead an algebraic constraint

distributed along the thickness of each electrode, which relates the local reaction rate to the local overpotential. Figure 2.3 presents a block diagram showing the dependencies of the different equations of the model upon each other. Note that the cell temperature T is not represented on this diagram, but affects most model equations as discussed in Section 2.3. This diagram highlights the fact that the reaction rate j is a critical variable of the model, which is used along with the applied current density (model input) to compute all other variables. The problem made clear by figure 2.3 is that the reaction rate j must be computed from all other model variables, but is also required to compute all other variables. Note that only the integral of the reaction rate is known from the model input using (2.18) and (2.19), but the actual profile of the reaction rate across the electrode cannot be computed from the applied current density i_{app} alone. The P2D model contains so-called 'algebraic loops' and therefore consists of a set of partial-differential-algebraic equations (PDAEs). Usually the literature suggests that at least both the electrolyte and solid-phase potential profiles must be retained as algebraic variables when implementing the model [60, 112, 62]. However, by examining figure 2.3, and recalling that the constraints (2.18) and (2.19) only implicitly define $\phi_{\text{s}}^{\text{cc}}$ in terms of j and i_{app}, one can see that given the reaction rate j and the solid-phase potential at the current collector $\phi_{\text{s}}^{\text{cc}}$ all other model variables can be computed without ambiguity. Consequently a smaller number of algebraic constraints can be used compared to the literature by considering only the reaction rate profile j and the value of the solid-phase potential at the current collectors $\phi_{\text{s}}^{\text{cc}}$ as algebraic variables.

2.2 The single-particle model

The single-particle (SP) model, originally developed by Atlung *et al.* [47] for cathode insertion materials and later applied to metal-hybride [113] and lithium-

ion batteries [48] can be regarded as a simplification of the P2D model where the electrolyte dynamics are neglected. Each electrode is modelled by a single spherical particle of active material in which the linear Fickian diffusion equation (2.3) is solved. As a result, the reaction rate is assumed uniform within each electrode, which allows its direct computation from the applied current density. Unlike the P2D model, the SP model consists only of PDEs without any algebraic constraint making its time integration more tractable. For this reason, the SP model has been used throughout this work for developing state and parameter estimation algorithms before applying these to the more challenging P2D model.

2.2.1 Solid-phase diffusion model with uniform reaction rate

The Fickian diffusion model solved within the particle describing each electrode in the SP model involves the same initial-boundary-value problem (2.3)-(2.4)-(2.5) as the P2D model and is restated here for completeness. The diffusion PDE in spherical coordinate is given by,

$$\frac{\partial c_\mathrm{s}}{\partial t} = \frac{1}{r^2}\frac{\partial}{\partial r}\left(r^2 D_\mathrm{s}\frac{\partial c_\mathrm{s}}{\partial r}\right), \tag{2.20}$$

and is subject to the following Neumann boundary conditions at the particle centre and surface

$$\left.\frac{\partial c_\mathrm{s}}{\partial r}\right|_{r=0} = 0 \quad \text{and} \qquad D_\mathrm{s}\left.\frac{\partial c_\mathrm{s}}{\partial r}\right|_{r=R_\mathrm{s}} = -j. \tag{2.21}$$

The main difference between the P2D and SP model resides in the fact that the reaction rate j is assumed uniform within each electrode. Therefore, considering a uniformly distributed reaction rate (*i.e.* independent of x) in relations (2.18) and (2.19), one can derive the following expressions for the reaction rate in terms

of the applied current density in the anode and cathode respectively

$$j = \frac{+i_{\text{app}}}{a_{\text{s}}\delta\mathcal{F}} \quad \text{for} \quad x \in \Omega_1, \tag{2.22}$$

and

$$j = \frac{-i_{\text{app}}}{a_{\text{s}}\delta\mathcal{F}} \quad \text{for} \quad x \in \Omega_3. \tag{2.23}$$

It is worth recalling that the parameters a_{s} and δ depend on the electrode considered and therefore take different values in (2.22) and (2.23).

2.2.2 Voltage measurement equation

The initial-boundary value problems (2.3)-(2.4)-(2.5) for each electrode constitute the dynamic part of the SP model. The battery terminal voltage V is given by the non-linear measurement equation

$$V = U_3\left(x_{\text{s},3}^{\text{surf}}\right) - U_1\left(x_{\text{s},1}^{\text{surf}}\right) + \eta_3 - \eta_1 - R_{\text{ctc}}i_{\text{app}}. \tag{2.24}$$

This voltage equation is easily derived by considering the expression for the voltage $V = \phi_{\text{s},3}^{\text{cc}} - \phi_{\text{s},1}^{\text{cc}} - R_{\text{ctc}}i_{\text{app}}$, recalling that the solid-phase surface potential is uniform across each electrode in the SP model (*i.e.* $\phi_{\text{s}}^{\text{cc}} = \phi_{\text{s}}$), and substituting the expression for ϕ_{s} obtained using the definition of overpotential (2.11) with $\phi_{\text{e}} = 0$ since electrolyte effects are neglected.

Similar to the P2D model, the anode and cathode overpotentials η in (2.24) are governed by the Butler–Volmer equation (2.9). However, the cathodic and anodic reaction kinetics are usually considered symmetrical in the SP model by assuming that the charge transfer coefficients are equal $\alpha_{\text{c}} = \alpha_{\text{a}} = 0.5$. This approximation allows the inversion of the Butler–Volmer equation to obtain an explicit expression

for the overpotential η in terms of the reaction rate j according to

$$\eta = \frac{2RT}{\mathcal{F}} \sinh^{-1}\left(\frac{\mathcal{F}}{2i_0} j\right), \tag{2.25}$$

where the exchange current density i_0 is given by (2.10) with the electrolyte concentration c_e regarded as a constant parameter. The expression obtained by combining (2.24), (2.25) and (2.10) yields a non-linear measurement equation for the cell terminal voltage that depends only on the lithium concentration c_{s} and fixed model parameters with no dynamics involved, which means that the voltage can be computed independently of the time integration.

Once the PDEs (2.3) equipped with the boundary conditions (2.4)-(2.5) are discretised in space in both electrodes, the SP model can be cast into a standard non-linear state-space model with linear state equations arising from the discrete diffusion models, and a scalar non-linear measurement equation for the cell terminal voltage. The absence of algebraic constraint in the SP model makes its solution using standard ODE solvers much easier compared to the P2D model for which a DAE solver must be used. The spatial discretisation and practical MATLAB® implementation of both the SP model and the P2D model are discussed at length in Chapter 3.

2.3 Thermal model

Various approaches have been considered in the literature as to how to include thermal effects in battery electrochemical models such as the P2D model. The problem of coupling a thermal model to the P2D model is threefold: (i) a geometry (bulk, 1D, 2D or 3D) on which to solve the heat equation must be chosen with appropriate boundary conditions, (ii) an expression for the heat generation rate must be derived, and (iii) temperature-dependencies of model parameters should be taken into account. The following section gives an overview of the different

approaches reported in the literature. The modelling approach used in the present work, detailed in Sections 2.3.2 to 2.3.4, consists of coupling a bulk thermal model assuming uniform cell temperature and heat generation rate to the P2D model. In addition, some parameters of the P2D model are made temperature-dependent using empirical relations, which yields further couplings between the thermal and P2D models.

2.3.1 Overview of literature

Prediction of heat generated during battery operation is of utmost importance when modelling thermal effects in a cell. Many mechanisms can contribute to the total heat generated in a lithium-ion cell, such as Joule heating due to contact resistances, reversible entropic heat generation arising from chemical reactions, ohmic heating resulting from transport of lithium. By considering a general energy balance on a battery system under the assumption of uniform temperature, Bernardi *et al.* [114] derived a comprehensive expression for the heat generated in a cell using thermodynamic arguments, which is given in its simplified form[1] by

$$\dot{q}_{\text{gen}} = I\left(U - V - T\frac{dU}{dT}\right). \tag{2.26}$$

The term $I\,(U - V)$ is the irreversible contribution due to the cell overpotential (polarization term) and the term $IT\,(dU/dT)$ is the reversible contribution arising from the chemical reaction (entropic term). Equation (2.26) was used in several subsequent works to predict heat generation in battery cells using experimental voltage discharge curves [115–117], or the voltage predicted by the P2D model under isothermal galvanostatic discharge [36, 37] for instance. Temperature-dependent ionic diffusivity and conductivity were also used in [36, 37], but the P2D electrochemical model and the thermal model remained decoupled in practice

[1] In this simplified expression, a single chemical reaction is considered and heat contributions due to mixing, phase changes and variations of heat capacities are neglected.

because the heat generation predicted during isothermal simulations were used to predict cell temperature for non-isothermal operation.

An alternative approach for calculating the heat generated in insertion cells at uniform temperature was introduced by Rao and Newman [118] based on kinetics and transport considerations. By relating thermal energy to local potentials and reaction currents integrated over each cell domain this approach allows attributing contributions to specific sources (ohmic and reaction overpotential) and quantifying contributions from the anode, separator and cathode. The expression for the heat generation derived in [118] was later used in bulk [38] and two-dimensional [40] thermal models coupled to the P2D model to study the effect of cell design parameters and thermal management on the cell thermal behaviour.

Using a volume-averaging technique, Gu and Wang [39] later derived an expression for the local heat generation rate (*i.e.* defined at any point in the cell domain) in terms of local reaction currents and potentials. The local heat generation rate discussed in [39] was used in a 2D coupled thermal-electrochemical model in [42] to investigate 2D temperature effects in large form-factor batteries, and with a 1D thermal model coupled to the P2D model in [86] to investigate temperature gradients across an 8-cell lithium-ion battery stack.

Under certain conditions discussed in Section 2.3.2, the cell temperature can be considered uniform and a common approximation found in the literature consists of coupling the P2D model to a bulk thermal model where both the temperature and the heat generation rate are assumed uniform within the cell [106, 119]. An expression consistent with [118] for such a uniform heat generation rate can be derived by averaging the local heat generation over the cell volume [39], see equations (2.35) through (2.37).

The fully coupled solution of a multi-dimensional thermal model along with the electrochemical P2D model is computationally intensive. This usually requires a multi-scale multi-physics approach [43, 120] where the thermal model is solved on

the cell domain and temperature-dependent P2D models are solved simultaneously on a smaller scale electrode domain to predict the cell local electrochemical behaviour and local heat generation. Since the focus of this work is on the fast solution of the P2D electrochemical model rather than advanced thermal modelling, the bulk thermal model and average heat generation approach [39, 106, 119] is used and discussed in the subsequent sections.

2.3.2 Bulk thermal model

The distribution of temperature T within a lithium-ion battery can be described by a multi-dimensional heat equation considered on an elementary volume [39] according to

$$\rho c_{\mathrm{p}} \frac{dT}{dt} = \nabla \cdot \lambda \nabla T + \dot{q}'''_{\mathrm{gen}}. \tag{2.27}$$

Since a lithium-ion battery is composed of multiple materials, the density ρ, the specific capacity c_{p} and the thermal conductivity λ in (2.27) are volume-averaged values weighted according to the volume fraction of each material [39, 119]. The first term on the right $\nabla \cdot \lambda \nabla T$ is the heat conduction term, which describes how the heat diffuses within the material, while the second term on the right $\dot{q}'''_{\mathrm{gen}}$ is the rate of heat generation per volume unit, which will be discussed in section 2.3.3. Equation (2.27) must be considered with appropriate boundary conditions. A common approach consists of modelling the heat exchanged with the surroundings by Newton's law of convective cooling at the cell surface according to

$$\lambda \nabla T = \dot{q}''_{\mathrm{conv}}, \tag{2.28}$$

with the convective heat removal per unit area given by

$$\dot{q}''_{\mathrm{conv}} = -h \left(T_{\mathrm{surf}} - T_{\mathrm{amb}} \right), \tag{2.29}$$

where h is the convective heat transfer coefficient in $\mathrm{W\,m^{-2}\,K^{-1}}$.

As previously mentioned, a bulk thermal model is considered in the present work in order to minimise the model computational cost, hence assuming uniform temperature within the cell. Under this assumption, conductive heat transfer within the cell is assumed infinitely large and the thermal model (2.27)–(2.28) reduces to the bulk thermal model

$$\rho c_{\mathrm{p}} \frac{dT}{dt} = \dot{q}'''_{\mathrm{gen}} + \dot{q}'''_{\mathrm{conv}}, \tag{2.30}$$

where the temperature T is a scalar value. The rate of heat removal by convection per unit volume is given by the expression

$$\dot{q}'''_{\mathrm{conv}} = -\frac{hA_{\mathrm{cell}}\left(T - T_{\mathrm{amb}}\right)}{V_{\mathrm{cell}}}, \tag{2.31}$$

where A_{cell} is the cell surface area exposed to convective cooling and V_{cell} the cell volume. The expression for the heat generation rate $\dot{q}'''_{\mathrm{gen}}$ in the cell is given in section 2.3.3.

The validity of the assumption of uniform temperature can be assessed by considering the Biot number, a dimensionless quantity that compares internal conductive thermal resistance to convective thermal resistance at the surface of the cell [121].

$$\mathrm{Bi} = \frac{hL_{\mathrm{c}}}{\lambda} \tag{2.32}$$

The characteristic length L_{c} in (2.32) is defined as the ratio of cell volume to cell surface area exposed to cooling $V_{\mathrm{cell}}/A_{\mathrm{cell}}$. For values of the Biot number much smaller than one, heat transfer by conduction within the cell is much greater than convective heat transfer at the surface; hence, the temperature may be assumed uniform within the cell. In practice, when $\mathrm{Bi} < 0.1$, the error remains small [36, 121] and the assumption of uniform temperature is considered valid.

Using the Biot number definition along with the condition Bi < 0.1, the maximum value of heat transfer coefficient for which the approximation remains valid may be calculated for a given cell according to

$$h < \frac{0.1\lambda}{L_\mathrm{c}}. \tag{2.33}$$

The thermal conductivity λ is usually highly anisotropic due to the layered structure of lithium-ion batteries; the succession of electrode/separator interfaces can yield orders of magnitude lower through-plane conductivities than in-plane ones [122]. An 18650 cylindrical cell geometry has been assumed for the thermal model throughout this work. Drake *et al.* [122] investigated the anisotropic thermal properties of an 18650[2] LFP[3] cell and reported experimental values $\lambda_r = 0.20\,\mathrm{W\,m^{-1}\,K^{-1}}$ and $\lambda_z = 30.4\,\mathrm{W\,m^{-1}\,K^{-1}}$ for the radial and axial thermal conductivities respectively. Temperature gradients in the radial direction are therefore predominant in cylindrical cells. Assuming convective heat transfer with the surroundings only through the lateral surface, the characteristic length is given by the ratio of cell volume to lateral surface area $L_\mathrm{c} = 4.5 \times 10^{-3}\,\mathrm{m}$ for an 18650 cylindrical cell. Evaluating (2.33) using these properties yields an approximate value $h = 4.4\,\mathrm{W\,m^{-2}\,K^{-1}}$ for the maximum acceptable convective heat transfer coefficient under which the assumption of uniform cell temperature remains valid. Typical heat transfer coefficients for a body surrounded by air range from 2 to 25 $\mathrm{W\,m^{-2}\,K^{-1}}$ for free convection and from 25 to 250 $\mathrm{W\,m^{-2}\,K^{-1}}$ for forced convection [121]. The bulk thermal model approximation is therefore acceptable under mild free convection only. The assumption of uniform cell temperature may not hold however for high C-rate operation under forced convection or for larger cylindrical cells [123, 124]. Significant temperature gradients may also occur in

[2] 18650 refers to a standardized cylindrical cell form factor of diameter 18 mm and height 65 mm.

[3] Most simulations presented in this work assumed an 18650 LCO cell; however, the thermal properties of an LFP cell of the same form factor should provide a good approximation for those of the LCO cell.

large prismatic or pouch cells because of highly non-uniform heat generation due to larger currents experienced in the vicinity of the cell tabs [125–127, 43, 128]. Despite its limited validity range, the assumption of uniform temperature for computational simplicity is common in the literature [106, 119]. The coupling of a multi-dimensional cell thermal model to the electrochemical model is not a trivial task because the one-dimensional assumption of the P2D model must be lifted. Aware of the limitations of our thermal modelling approach, the approximation of uniform temperature is made in the present work because the focus of this dissertation is on the fast electrochemical modelling of lithium-ion batteries. Considerations of cell temperature distributions are beyond the scope of this thesis and left as an open-question for further improvements. Possible avenues of research include the consideration of a multi-dimensional cell thermal model with uniform heat generation coupled to a P2D model solved at an averaged cell temperature, or more advanced multi-scale methods as investigated in [43, 120].

2.3.3 Heat generation rate

The total heat generation rate per unit volume $\dot{q}'''_{\text{gen}}$ is assumed uniform and attributed to four main contributions according to

$$\dot{q}'''_{\text{gen}} = \dot{q}'''_{\text{rxn}} + \dot{q}'''_{\text{rev}} + \dot{q}'''_{\text{ohm}} + \dot{q}'''_{\text{ctc}} \tag{2.34}$$

where $\dot{q}'''_{\text{rxn}}$ is the reaction heat generation rate, $\dot{q}'''_{\text{rev}}$ is the reversible heat generation rate due to entropy changes in the electrode active material during lithium intercalation/de-intercalation, $\dot{q}'''_{\text{ohm}}$ is the electronic and ionic ohmic heat generation rate due to the transport of lithium, and $\dot{q}'''_{\text{ctc}}$ is the Joule ohmic heat due to the contact resistance R_{ctc} at the current collector/electrode interfaces. The volume-averaged heat generated by each of these per unit volume [39, 129, 119, 106] is

given by

$$\dot{q}'''_{\text{rxn}} = \frac{1}{L}\int_0^L a_{\text{s}}\mathcal{F}j\left(\phi_{\text{s}} - \phi_{\text{e}} - U\right)dx \tag{2.35}$$

$$\dot{q}'''_{\text{rev}} = \frac{1}{L}\int_0^L a_{\text{s}}\mathcal{F}j\left(T\frac{\partial U}{\partial T}\right)dx \tag{2.36}$$

$$\dot{q}'''_{\text{ohm}} = \frac{1}{L}\int_0^L \left[\sigma^{\text{eff}}\left(\frac{\partial \phi_{\text{s}}}{\partial x}\right)^2 + \kappa^{\text{eff}}\left(\frac{\partial \phi_{\text{e}}}{\partial x}\right)^2 + \kappa_{\text{D}}^{\text{eff}}\left(\frac{\partial \ln c_{\text{e}}}{\partial x}\right)\left(\frac{\partial \phi_{\text{e}}}{\partial x}\right)\right]dx \tag{2.37}$$

$$\dot{q}'''_{\text{ctc}} = \frac{R_{\text{ctc}}}{AV_{\text{cell}}}I^2 \tag{2.38}$$

with the diffusional effective conductivity defined as

$$\kappa_{\text{D}}^{\text{eff}} = \frac{2\left(1 - t_+\right)RT}{\mathcal{F}}\kappa^{\text{eff}}. \tag{2.39}$$

Note that the polarization term (2.35) and entropic term (2.36) correspond to the terms $I\left(U - V\right)$ and $IT\left(dU/dT\right)$ respectively in the simplified equation (2.26).

2.3.4 Temperature-dependent electrochemical parameters

During high C-rate operation, the cell temperature can increase significantly and affect the cell physical and chemical properties. Therefore, the coupling between the thermal and electrochemical model must include the temperature dependency of the model parameters. A common approach found in the literature [39, 106, 119, 2] consists of assuming a temperature dependency for a parameter ψ that follows Arrhenius' law according to

$$\psi = \psi^{\text{ref}}\exp\left[\frac{E_{\text{act}}^{\psi}}{R}\left(\frac{1}{T^{\text{ref}}} - \frac{1}{T}\right)\right] \tag{2.40}$$

where ψ^{ref} is the value of the parameter at the reference temperature T^{ref} and E_{act}^{ψ} denotes the activation energy associated with this parameter. Arrhenius' law (2.40) has been used to model the temperature-dependency of the solid-phase diffusivity D_{s} and the reaction rate constant k in particular.

Electrolyte transport properties such as diffusivity D_e and conductivity κ_e are also strongly dependent on temperature, as well as electrolyte concentration c_e. Experimentally fitted relations giving the temperature- and concentration-dependency of diffusivity and conductivity of a common lithium-ion battery electrolyte ($LiPF_6$ in PC/EC/DMC) have been reported in [92] and commonly used in the literature [129–131, 2] and throughout this work.

Finally, temperature also has an important impact on the open-circuit potential of the electrodes. However, experimental data for the simultaneous variation of open-circuit potential with temperature and stoichiometry are not readily available in the literature. Instead, experimentally fitted relations for the entropy change coefficient $(\partial U/\partial T)$ as a function of stoichiometry x_s [132, 133] can be used to obtain an approximation for the dependency of open-circuit potential on temperature using a first-order Taylor series expansion. The entropy change coefficient $(\partial U/\partial T)$ is related to the entropy change ΔS according to

$$\left(\frac{\partial U}{\partial T}\right) = \frac{\Delta S}{n\mathcal{F}} \tag{2.41}$$

where $n = 1$ is the number of electrons exchanged in the chemical reaction. Taking the first-order Taylor series expansion of the open-circuit potential with respect to the temperature gives the following expression for the open-circuit potential U as a function of stoichiometry x_s and temperature T,

$$U\left(x_\mathrm{s}, T\right) = U^\mathrm{ref}\left(x_\mathrm{s}\right) + \left(T - T^\mathrm{ref}\right)\frac{\Delta S(x_\mathrm{s})}{n\mathcal{F}}, \tag{2.42}$$

where U^ref is the open-circuit potential at T^ref and $\Delta S(x_\mathrm{s})$ is the measured entropy change as a function of stoichiometry.

Chapter 3

Fast solution of electrochemical models using orthogonal collocation

In this chapter the fast solution of the P2D model using the so-called *orthogonal collocation on Chebyshev polynomials* spectral method is discussed. Chebyshev orthogonal collocation is introduced in Section 3.1 and its application to the discretisation of the P2D model equations is presented in Section 3.2. Section 3.3 is devoted to the time integration of the differential-algebraic system of equations resulting from the spatial discretisation of the P2D model in MATLAB®. Finally in Section 3.4, the performance of the P2D model solution using orthogonal collocation are discussed.

3.1 Chebyshev orthogonal collocation

3.1.1 Chebyshev polynomials approximation

Spectral methods consist of expanding the solution u of a differential equation in terms of chosen orthogonal basis functions and determining the coefficients of this

expansion to satisfy the differential equation. For problems with periodic boundary conditions, sinusoidal functions are a natural choice of basis functions. However, for non-periodic boundary conditions, discontinuities introduced at the boundaries result in Gibbs phenomena that drastically impede spectral accuracy. This can be circumvented by adding linear and/or quadratic terms to the Fourier series expansion to enforce the boundary conditions as in [62]. However, Chebyshev polynomials are a more natural choice for the solution of differential equations with non-periodic boundary conditions such as the P2D model [134, 135]. The solution $u(x,t)$ of the PDE is therefore approximated by the truncated Chebyshev expansion:

$$u_N(x,t) = \sum_{k=0}^{N} \hat{u}_k(t) T_k(x), \quad x \in [-1,1] \tag{3.1}$$

where $\hat{u}_k(t)$ are the $N+1$ Chebyshev coefficients of the expansion that need to be determined and T_k denotes the Chebyshev polynomial of the first-kind of degree k. In the present work, the coefficients are determined by the so-called orthogonal collocation method, also sometimes referred to as the pseudo-spectral method. The coefficients $\hat{u}_k(t)$ are calculated by forcing the Chebyshev series (3.1) to satisfy the differential equation exactly at the discretisation nodes x_i given by:

$$x_i = \cos\left(\frac{i\pi}{N}\right) \quad i = 0, 1, ..., N. \tag{3.2}$$

By choosing the coefficients $\hat{u}_k(t)$ so that $u_N(x_i,t) = u(x_i,t)$, it can be shown [136] that the polynomial u_N can be expressed in terms of the discrete values of the solution at the collocation nodes $u_j(t) = u(x_j,t) = u_N(x_j,t)$ according to,

$$u_N(x,t) = \sum_{j=0}^{N} u_j(t) \phi_j(x), \quad x \in [-1,1] \tag{3.3}$$

where the functions ϕ_j are given by:

$$\phi_j(x) = \frac{(-1)^{j+1}(1-x^2)T'_N(x)}{\bar{c}_j N^2(x-x_j)}, \quad x \in [-1,1] \tag{3.4}$$

with $\bar{c}_j = 2$ for $j = 0$ and $j = N$ and $\bar{c}_j = 1$ otherwise.

3.1.2 Differentiation

When implementing the orthogonal collocation method for the solution of PDEs, the coefficients $\hat{u}_k$ of the series expansion are rarely computed explicitly but the differentiation of u is usually performed using a differentiation matrix. The p^{th} derivative of the solution u with respect to x evaluated at the collocation points can be expressed by:

$$u_N^{(p)}(x_i) = \sum_{j=0}^{N} d_{i,j}^{(p)} u_N(x_j), \quad i = 0, 1, ..., N \tag{3.5}$$

where the coefficients $d_{i,j}^{(p)}$ can be determined by evaluating the p^{th} derivative of the interpolant (3.3) at the collocation nodes (3.2). The coefficients $d_{i,j}^{(p)}$ are the elements of the so-called differentiation matrix D_N^p, which is the discrete approximation to the p^{th} derivative operator $\partial^p/\partial x^p$. The derivative of u evaluated at the collocation nodes $\mathbf{u}^{(p)}$ can be expressed in terms of the value of u at the collocation nodes $\mathbf{u}$ with:

$$\mathbf{u}^{(p)} = \mathrm{D}_N^p \mathbf{u} \tag{3.6}$$

The MATLAB® function *chebdif.m* provided by Weideman and Reddy in [136] was used to compute the Chebyshev orthogonal collocation differentiation matrices. Note that the value of the independent variable u at any point in the domain can be computed from the vector $\mathbf{u}$ of values at the collocation nodes by recalling the underlying Chebyshev interpolant. In practice, the interpolating MATLAB® function *chebint.m* in [136] was used in the present work.

These differentiation matrices $\mathrm{D}_N^p \in \mathbb{R}^{(N+1)\times(N+1)}$ do not satisfy any particular boundary conditions. When discretising boundary-value problems such as the equations composing the electrochemical models discussed in Chapter 2, one must make sure that the boundary conditions are taken into account. In the present work, the boundary conditions are accounted for by reducing the size of the differentiation matrix, since each boundary condition gives an additional constraint that can be used to express the value of the solution at a chosen collocation node in terms of the solution values at all the other collocation nodes. This reduces the size of the differentiation matrix by one row and one column for each boundary condition considered. This leads to reduced differentiation matrices that automatically satisfy the boundary conditions. The derivation of such discrete differential operators that account for boundary conditions is presented in details in Section 3.2 for the discretisation of the SP and P2D electrochemical models.

3.1.3 Integration and Quadrature

Chebyshev orthogonal collocation is also a powerful tool to perform numerical integration and quadrature. An intuitive explanation for the integration capabilities of orthogonal collocation can be directly derived from the differentiation matrices discussed by Trefethen in [135]. Consider the problem of computing the indefinite integral $I(x)$ of a function f on the domain $[-1\,,\,+1]$ according to

$$I(x) = \int_{x'=-1}^{x} f\left(x'\right) dx'. \tag{3.7}$$

This integral equation can be cast into the equivalent boundary-value problem

$$u'(x) = f\left(x\right) \quad \text{subject to} \quad u\left(-1\right) = 0. \tag{3.8}$$

Using the differentiation matrix approach discussed in Section 3.1.2, a discrete approximation to this BVP is given by

$$\tilde{\mathrm{D}}'_N \tilde{\mathbf{u}} = \tilde{\mathbf{f}}, \tag{3.9}$$

where $\tilde{\mathbf{u}}, \tilde{\mathbf{f}} \in \mathbb{R}^N$ denote the vectors of values taken by u and f respectively at the Chebyshev collocation nodes except at the boundary $x = -1$, and $\tilde{\mathrm{D}}'_N \in \mathbb{R}^{N \times N}$ is the differential operator obtained by deleting the last row and column of the first-derivative Chebyshev differentiation matrix D'_N to satisfy the Dirichlet boundary condition $u(-1) = 0$. A discrete approximation for the indefinite integral in (3.7) is therefore given by

$$I(x) \approx \tilde{\mathbf{u}} = \tilde{\mathrm{I}}_N \tilde{\mathbf{f}} \tag{3.10}$$

where the Chebyshev integration matrix $\tilde{\mathrm{I}}_N = \left(\tilde{\mathrm{D}}'_N\right)^{-1}$ is defined as the inverse of the Chebyshev differential operator $\tilde{\mathrm{D}}'_N$. Similarly, the definite integral

$$I = \int_{-1}^{+1} f(x)\, dx, \tag{3.11}$$

obtained by evaluating the indefinite integral (3.7) at $x = +1$, can be computed numerically using the quadrature formula

$$I \approx \tilde{\mathbf{w}}_N^{\mathrm{T}} \tilde{f}, \tag{3.12}$$

where the quadrature weights $\tilde{\mathbf{w}}_N^{\mathrm{T}}$ are obtained by extracting the first row of the integration matrix $\tilde{\mathrm{I}}_N$. However, the inversion of the differentiation matrix is not the most appropriate approach to computing the Chebyshev integration matrix and quadrature weights because it neglects the value $f(-1)$ and introduces numerical approximations. In practice, the Clenshaw–Curtis quadrature [137] is used, which is a more principled approach based on applying the Fast Fourier Transform to the Chebyshev polynomial approximation [135].

In the present work, the function *cumsummat.m* from the *Chebfun* package [138] is used to compute the integration matrix $\mathrm{I}_N \in \mathbb{R}^{(N+1)\times(N+1)}$. Note that the rows of the integration matrix returned by *cumsummat.m* must be flipped[1] to ensure that the definite integral is equal to zero at $x = -1$ rather than $x = +1$ when used in conjunction with the *chebdif.m* function from [136]. The Clenshaw–Curtis quadrature weights $\mathbf{w}_N^{\mathrm{T}} \in \mathbb{R}^{N+1}$ are computed using the *clencurt.m* function given by Trefethen in [135].

3.2 Spatial discretisation of the P2D model

This section discusses the practical application of the Chebyshev orthogonal collocation presented in Section 3.1 to the spatial discretisation of PDEs constituting the P2D and SP models. The changes of scale and the domain decomposition technique required to discretise the micro- and macro-scale model equations of the P2D model are introduced in Section 3.2.1. The discretisation of the solid-phase diffusion (for both the P2D and SP models) and the electrolyte diffusion equation (for the P2D model only) are discussed in Sections 3.2.2 and 3.2.3 respectively. Finally, the computation of the current density and potential profiles in both the solid- and liquid-phase as well as the reaction rate are discussed in Section 3.2.4 through 3.2.6.

3.2.1 Computational domain decomposition

A major advantage of spectral methods is their fast rate of convergence, often referred to as *spectral accuracy* in the literature [135], compared to the finite-difference method for example. This fast convergence behaviour allows reaching the same solution accuracy than finite-difference but with a highly reduced number of

[1] This is because by convention the integration matrix in *cumsummat.m* returns an integral of zero for the first element of the vector of function values at the collocation nodes, which corresponds to $x = +1$ when using the *chebdif.m* function.

discretisation nodes required, typically by a factor of 10 to 100. However, spectral accuracy is achieved provided that the solution is 'sufficiently smooth' on the domain considered and discontinuities can highly impede spectral accuracy. In

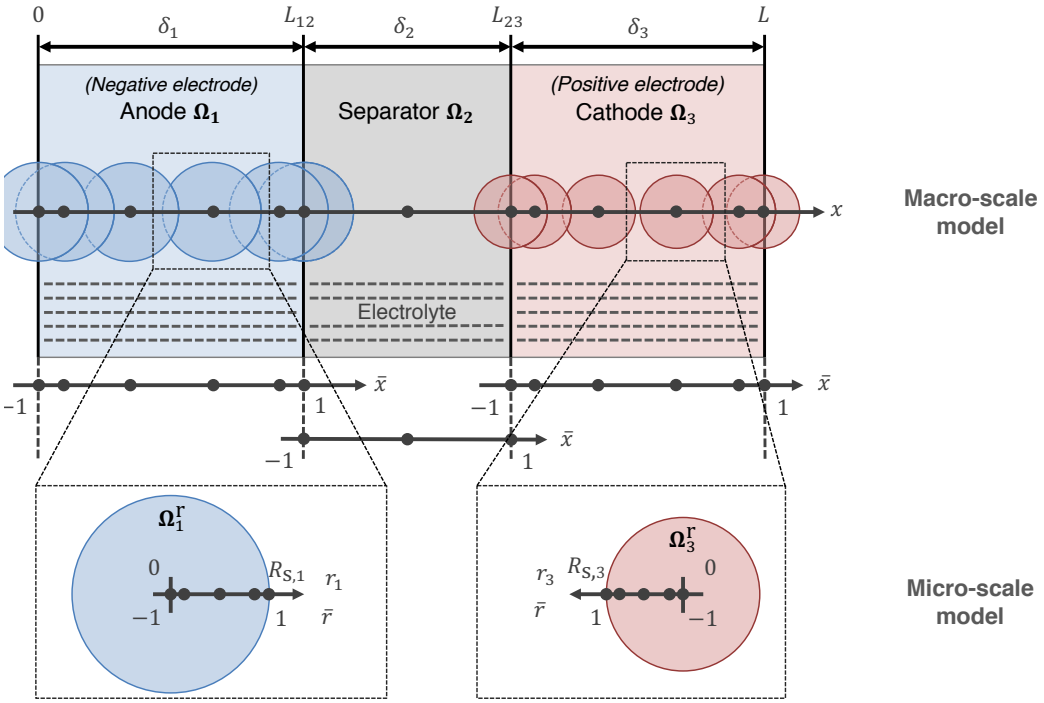

Fig. 3.1 Schematic of the cell domain decomposition into sub-domains and their mapping onto the Chebyshev nodes computational domains $\bar{r}, \bar{x}$ [2].

the P2D model, such discontinuities appear at each electrode/separator interfaces for $x = L_{12}$ and $x = L_{23}$ due to the sudden change in material properties. The cell domain is therefore decomposed into three sub-domains denoted Ω_1, Ω_2 and Ω_3 for the anode, separator and cathode sub-domains respectively, where the model equations are solved on distinct sets of Chebyshev collocation nodes $\bar{x}$ as shown on figure 3.1. As a result, additional boundary conditions must be considered at each electrode/separator interface to ensure the continuity of the dependent variables and the conservation of fluxes between two consecutive sub-domains. Furthermore, the PDEs constituting the P2D model must be rescaled on the domain $[-1\,,\,1]$ where the Chebyshev nodes $\bar{x}$ and $\bar{r}$ are defined. The subsequent sections give

detailed explanation on the model reformulation into sub-domains and the model discretisation using Chebyshev orthogonal collocation.

3.2.2 Solid-phase diffusion model

The diffusion equation in spherical coordinates (2.3) governing the concentration of lithium in the solid-phase c_s can be reformulated as

$$\frac{\partial c_s}{\partial t} = D_s \left(\frac{\partial^2 c_s}{\partial r^2} + \frac{2}{r} \frac{\partial c_s}{\partial r} \right) \tag{3.13}$$

subject to the Neumann boundary conditions given in (2.4) at the centre of the particle and (2.5) at the surface.

Change of variable

In order to simplify the model discretisation, the change of variable $u_s = r c_s$ is introduced, which yields the relations

$$\frac{\partial c_s}{\partial r} = \frac{1}{r} \frac{\partial u_s}{\partial r} - \frac{c_s}{r} \tag{3.14}$$

$$\frac{\partial^2 c_s}{\partial r^2} = \frac{1}{r} \frac{\partial^2 u_s}{\partial r^2} - \frac{2}{r} \frac{c_s}{\partial r}. \tag{3.15}$$

Under this change of variable, the diffusion equation (3.13) takes the simpler form

$$\frac{\partial u_s}{\partial t} = D_s \frac{\partial^2 u_s}{\partial r^2}. \tag{3.16}$$

The homogeneous Neumann boundary condition at the particle centre (2.4) is replaced by the simpler homogeneous Dirichlet boundary condition (3.17) to ensure that $c_s = u_s / r$ remains finite as $r \to 0$.

$$u_s \left(r = 0 \right) = 0 \tag{3.17}$$

The Neumann boundary condition (2.5) at the surface becomes the mixed boundary condition

$$\frac{1}{R_\mathrm{s}}\left.\frac{\partial u_\mathrm{s}}{\partial r}\right|_{r=R_\mathrm{s}} - \frac{u_\mathrm{s}\left(r=R_\mathrm{s}\right)}{R_\mathrm{s}^2} = \frac{-j}{D_\mathrm{s}}. \tag{3.18}$$

Coordinate transformation

The reformulated PDE (3.16) and boundary conditions (3.17)-(2.5) are defined on the domain $r \in [0\,,\, R_\mathrm{s}]$. However, the discretisation using orthogonal collocation on Chebyshev nodes requires rescaling the domain on $[-1\,,\, 1]$ using the coordinate transformation

$$\bar{r} = \frac{2}{R_\mathrm{s}}\left(r - \frac{R_\mathrm{s}}{2}\right). \tag{3.19}$$

Under this coordinate transformation, one can easily show with the chain rule that

$$\frac{\partial}{\partial r} = \frac{2}{R_\mathrm{s}}\frac{\partial}{\partial \bar{r}} \quad \text{and} \quad \frac{\partial^2}{\partial r^2} = \frac{4}{R_\mathrm{s}^2}\frac{\partial^2}{\partial \bar{r}^2}. \tag{3.20}$$

Using this coordinate transformation to rescale the boundary value problem (3.16)-(3.17)-(3.18) therefore yields the reformulated solid-phase diffusion equation

$$\frac{\partial u_\mathrm{s}}{\partial t} = \frac{4D_\mathrm{s}}{R_s^2}\frac{\partial^2 u_\mathrm{s}}{\partial \bar{r}^2}, \tag{3.21}$$

subject to the homogeneous Dirichlet boundary condition at the centre

$$u_\mathrm{s}(\bar{r} = -1) = 0, \tag{3.22}$$

and the inhomogeneous mixed boundary condition at the surface

$$\left.\frac{\partial u_\mathrm{s}}{\partial \bar{r}}\right|_{\bar{r}=1} - \frac{u_\mathrm{s}\left(\bar{r}=1\right)}{2} = -\frac{R_\mathrm{s}^2}{2D_\mathrm{s}}j \tag{3.23}$$

An alternative approach to discretising the solid-phase diffusion in the spherical particles is discussed in Appendix B, which consists in mapping the domain

$r \in [-R\,,\,R]$ instead of $r \in [0\,,\,R]$ to the computational domain $\bar{r} \in [-1\,,\,1]$ and discarding half of the Chebyshev nodes using a symmetry argument. An advantage of this alternative approach is that the Chebyshev nodes are clustered at the surface of the particle where sharp concentration gradients occur, whereas fewer nodes are employed at the centre of the particle where the concentration profile remains flat.

Differentiation matrices including boundary conditions

The spherical particle domain $\bar{r} \in [-1\,,\,1]$ of the reformulated boundary-value problem (3.21)-(3.22)-(3.23) is discretised using $N+1$ Chebyshev nodes, with $N \in \mathbb{N}$. In order to obtain the discrete equivalent to the diffusion equation (3.21), a discrete approximation to the linear differential operator $\partial^2/\partial\bar{r}^2$ (*i.e.* a second-derivative differentiation matrix) in (3.21) that satisfies the boundary conditions (3.22)-(3.23) must be derived.

Notation 1 *The vectors* $\mathbf{u}, \mathbf{u}', \mathbf{u}'' \in \mathbb{R}^{N+1}$ *contain respectively the values of* u_s *and the first- and second-derivative of* u_s *at the* $N+1$ *collocation nodes, with the first and last vector values* $\mathbf{u}_1$ *and* $\mathbf{u}_{N+1}$ *corresponding to the nodes* $\bar{r} = 1$ *and* $\bar{r} = -1$ *respectively. Note that in the remainder of this Section 3.2.2 the subscript* s *is omitted from the vector notation for better readability.*

Notation 2 *The first- and second derivative Chebyshev differentiation matrices of size* $(N+1) \times (N+1)$ *are denoted* D'_N *and* D''_N *respectively, with* $N \in \mathbb{N}$ *the number of Chebyshev nodes used to discretise the domain.*

Following the definition of Chebyshev differentiation matrices in Section 3.1.2, the discrete approximations to the first- and second-derivative of u_s at the $N+1$ collocation nodes are given by

$$\mathbf{u}' = \mathrm{D}'_N\mathbf{u} \quad \text{and} \quad \mathbf{u}'' = \mathrm{D}''_N\mathbf{u}. \tag{3.24}$$

Notation 3 *The i^{th} row and j^{th} column element of a matrix* M *is denoted* $[\mathrm{M}]_{i,j}$ *and a range of rows or columns is denoted $i:j$, using a convention familiar to MATLAB® programmers. For example, the column-vector obtained by extracting the elements in the k^{th} column and the i^{th} to j^{th} rows of the matrix* M *is denoted* $[\mathrm{M}]_{i:j,k}$.

The boundary condition equations (3.22) and (3.23) provide two additional constraints on the discrete values of u_{s}, allowing the size of D''_N to be reduced by two. Firstly, the centre boundary condition (3.22) states that the value of u_{s} at the centre is equal to zero, yielding $\mathbf{u}_{N+1} = 0$. Secondly, the surface boundary condition (3.23) allows the value of u_{s} at the surface $\mathbf{u}_1$ to be expressed in terms of the other values at the collocation nodes. The discrete approximation to the surface boundary condition (3.23) is given by

$$[\mathrm{D}'_N]_{1,1}\,\mathbf{u}_1 + [\mathrm{D}'_N]_{1,2:N}\,\bar{\mathbf{u}} + [\mathrm{D}'_N]_{1,N+1}\,\mathbf{u}_{N+1} - \frac{1}{2}\mathbf{u}_1 = -\frac{R_{\mathrm{s}}}{2D_{\mathrm{s}}}j \tag{3.25}$$

where $\bar{\mathbf{u}} \in \mathbb{R}^{(N-1)}$ denotes the vector containing the values of u_{s} at the inner nodes of the domains, which is obtained by removing the first and last elements of $\mathbf{u}$. Recalling that $\mathbf{u}_{N+1} = 0$ from (3.22), the value of u_{s} at the surface is therefore given by

$$\mathbf{u}_1 = \frac{1}{1 - 2\,[D'_N]_{1,1}}\left(2\,[D'_N]_{1,2:N}\,\bar{\mathbf{u}} + \frac{R_{\mathrm{s}}^2}{D_{\mathrm{s}}}j\right) \tag{3.26}$$

Using (3.24) and recalling that $\mathbf{u}_{N+1} = 0$, an expression for the second-derivative of u_{s} at the inner nodes of the domain only $\bar{\mathbf{u}}''$ is given by

$$\bar{\mathbf{u}}'' = [D''_N]_{2:N,1}\,\mathbf{u}_1 + [D''_N]_{2:N,2:N}\,\bar{\mathbf{u}} \tag{3.27}$$

Substituting $\mathbf{u}_1$ by its expression (3.26) yields the relation

$$\bar{\mathbf{u}}'' = \bar{\mathrm{D}}''_N\bar{\mathbf{u}} + \bar{\mathbf{d}}^{\mathrm{bc}}_N j, \tag{3.28}$$

where the second-derivative differentiation matrix $\bar{\mathrm{D}}''_N \in \mathbb{R}^{(N-1)\times(N-1)}$ accounting for the homogeneous boundary conditions is given by

$$\bar{\mathrm{D}}''_N = \left[D''_N\right]_{2:N,2:N} + \frac{2\left[D''_N\right]_{2:N,1}\left[D'_N\right]_{1,2:N}}{1-2\left[D'_N\right]_{1,1}}, \tag{3.29}$$

and the vector $\bar{\mathbf{d}}^{\mathrm{bc}}_N \in \mathbb{R}^{N-1}$ arising from the non-homogeneous mixed boundary condition at the particle surface is given by

$$\bar{\mathbf{d}}^{\mathrm{bc}}_N = \frac{\left[D''_N\right]_{2:N,1}}{1-2\left[D'_N\right]_{1,1}}\frac{R_{\mathrm{s}}^2}{D_{\mathrm{s}}}. \tag{3.30}$$

Linear state-space model representation

A discrete approximation to the reformulated solid-phase diffusion equation (3.21) that satisfies the boundary conditions (3.22)-(3.23) can be obtained by substituting the continuous (linear) differential operator $\partial^2/\partial\bar{r}^2$ in (3.21) by its discrete approximation (3.27) according to

$$\frac{\partial\bar{\mathbf{u}}}{\partial t} = \frac{4D_{\mathrm{s}}}{R_{\mathrm{s}}^2}\left(\bar{\mathrm{D}}''_N\bar{\mathbf{u}} + \bar{\mathbf{d}}^{\mathrm{bc}}_N j\right). \tag{3.31}$$

This equation can be written a standard linear state-space model form

$$\frac{\partial\bar{\mathbf{u}}}{\partial t} = \mathrm{A}\bar{\mathbf{u}} + \mathbf{b}j \tag{3.32}$$

where the state matrix $\mathrm{A} \in \mathbb{R}^{(N-1)\times(N-1)}$ and input vector $\mathbf{b} \in \mathbb{R}^{N-1}$ is defined as

$$\mathrm{A} = D_{\mathrm{s}}\frac{4}{R_{\mathrm{s}}^2}\bar{\mathrm{D}}''_N \quad \text{and} \quad \mathbf{b} = \frac{4D_{\mathrm{s}}}{R_{\mathrm{s}}^2}\bar{\mathbf{d}}^{\mathrm{bc}}_N = \frac{4\left[D''_N\right]_{2:N,1}}{1-2\left[D'_N\right]_{1,1}} \tag{3.33}$$

The surface concentration can be recovered from the vector $\bar{\mathbf{u}}$ using the measurement equation

$$c_{\mathrm{s}}^{\mathrm{surf}} = \mathbf{c}^{\mathrm{T}}\bar{\mathbf{u}} + dj \tag{3.34}$$

where the row-vector $\mathbf{c}^{\mathrm{T}} \in \mathbb{R}^{N-1}$ and the scalar $d \in \mathbb{R}$ derived using (3.26) and recalling the change of variable $u_{\mathrm{s}} = rc_{\mathrm{s}}$ are given by

$$\mathbf{c}^{\mathrm{T}} = \frac{2}{R_{\mathrm{s}}} \frac{[D'_N]_{1,2:N}}{1 - 2[D'_N]_{1,1}} \quad \text{and} \quad d = \frac{R_{\mathrm{s}}}{D_{\mathrm{s}}} \frac{1}{1 - 2[D'_N]_{1,1}} \tag{3.35}$$

Therefore, the solid-phase diffusion in a spherical particle of the P2D or SP model can be cast into the standard linear state-space model

$$\begin{cases} \partial \bar{\mathbf{u}}/\partial t &= \mathrm{A}\bar{\mathbf{u}} + \mathbf{b}j \\ c_{\mathrm{s}}^{\mathrm{surf}} &= \mathbf{c}^{\mathrm{T}}\bar{\mathbf{u}} + dj \end{cases} \tag{3.36}$$

with the values of $u_{\mathrm{s}} = rc_{\mathrm{s}}$ at the inner nodes of the domain $\bar{\mathbf{u}}$ as state vector, the reaction rate j as input, and the surface concentration $c_{\mathrm{s}}^{\mathrm{surf}}$ as measurement. Note that if a thermal model is considered one may want to 'leave out' the temperature-dependent solid-phase diffusivity $D_{\mathrm{s}}(T)$ of the matrix A and scalar d to facilitate the model implementation. In the P2D model, a linear state-space model (3.36) is solved at each collocation node in the anode and cathode subdomains Ω_1 and Ω_3 respectively; whereas in the SP model, a single state-space model (3.36) is considered in each electrode.

3.2.3 Electrolyte diffusion model

The PDE governing the electrolyte concentration is the diffusion equation (2.6) defined across the anode, separator and cathode domains Ω_1, Ω_2 and Ω_3 respectively, subject to zero-flux boundary conditions at the current collectors. Recalling that the effective electrolyte diffusivity given by $D^{\mathrm{eff}} = \epsilon^b D$ is concentration-dependent and using the chain rule, equation (2.6) can be reformulated as

$$\frac{\partial c}{\partial t} = \epsilon^b D \frac{\partial^2 c}{\partial x^2} + \epsilon^b \frac{\partial D}{\partial c} \left(\frac{\partial c}{\partial x} \right)^2 + \frac{a_{\mathrm{s}}(1 - t_+)}{\epsilon} j \tag{3.37}$$

Notation 4 *Throughout this section only (Section 3.2.3), the subscript* e *referring to the electrolyte is dropped for the sake of readability. Therefore the variables* c*,* D *and* ϵ *employed in this section refer to the electrolyte concentration* c_e*, the electrolyte diffusivity* D_e *and the electrolyte volume fraction* ϵ_e*.*

The reformulated diffusion equation (3.37) features two linear differential operators, the first- and second-derivative operators $\partial/\partial x$ and $\partial^2/\partial x^2$ respectively, for which a discrete approximation can be derived using the Chebyshev orthogonal collocation differentiation matrices introduced in Section 3.1.2.

Domain decomposition

Because the electrolyte diffusion equation is solved on three distinct sets of Chebyshev nodes $\bar{x}$, as shown in figure 3.1, equation (2.6) is decomposed onto the three sub-domains of the cell according to:

$$\begin{cases} \frac{\partial c_1}{\partial t} = \epsilon_1^{b_1}\left(D\frac{\partial^2 c_1}{\partial x^2} + \frac{\partial D}{\partial c_1}\left(\frac{\partial c_1}{\partial x}\right)^2\right) + \frac{a_{s,1}}{\epsilon_1 \mathcal{F}}\left(1-t_+\right) j_1 & \text{for} \quad x \in [0, L_{12}] \\ \frac{\partial c_2}{\partial t} = \epsilon_2^{b_2}\left(D\frac{\partial^2 c_2}{\partial x^2} + \frac{\partial D}{\partial c_2}\left(\frac{\partial c_2}{\partial x}\right)^2\right) & \text{for} \quad x \in [L_{12}, L_{23}] \\ \frac{\partial c_3}{\partial t} = \epsilon_3^{b_3}\left(D\frac{\partial^2 c_3}{\partial x^2} + \frac{\partial D}{\partial c_3}\left(\frac{\partial c_3}{\partial x}\right)^2\right) + \frac{a_{s,3}}{\epsilon_3 \mathcal{F}}\left(1-t_+\right) j_3 & \text{for} \quad x \in [L_{23}, L] \end{cases} \tag{3.38}$$

One can see that there is no chemical reaction occurring in the separator; therefore the diffusion equation does not feature any source term in the separator domain Ω_2. The notations used in this chapter for the macro-scale domain decomposition into three sets of Chebyshev nodes are summarised and illustrated in figure 3.2.

Notation 5 *Following the convention introduced in Chapter 2, the model variables (concentration, reaction rate, etc.) considered in each sub-domain separately are indexed with the subscripts* 1*,* 2 *and* 3 *in the anode* Ω_1*, separator* Ω_2 *and cathode* Ω_3 *sub-domains respectively.*

At each current collector, the boundary condition remains a zero-flux boundary condition according to

$$\left.\frac{\partial c_1}{\partial x}\right|_{x=0} = 0 \quad \text{and} \quad \left.\frac{\partial c_3}{\partial x}\right|_{x=L} = 0. \tag{3.39}$$

The electrolyte concentration must be continuous across the cell, thus the concentration values are equal at the boundaries of the two contiguous domains at each electrode/separator interface, yielding the continuity conditions

$$c_1(x = L_{12}) = c_2(x = L_{12}) \quad \text{and} \quad c_2(x = L_{23}) = c_3(x = L_{23}). \tag{3.40}$$

Additionally, at the electrode/separator interface, the flux of lithium ions exiting a domain must be equal to the flux entering the contiguous domain according to the interface boundary conditions

$$\epsilon_1^{b_1} D \left.\frac{\partial c_1}{\partial x}\right|_{x=L_{12}} = \epsilon_2^{b_2} D \left.\frac{\partial c_2}{\partial x}\right|_{x=L_{12}} \quad \text{and} \quad \epsilon_2^{b_2} D \left.\frac{\partial c_2}{\partial x}\right|_{x=L_{23}} = \epsilon_3^{b_3} D \left.\frac{\partial c_3}{\partial x}\right|_{x=L_{23}}. \tag{3.41}$$

Owing to the continuity conditions (3.40) the concentration-dependent electrolyte diffusivity D must also equate in both domains at the electrode/separator interface; hence the diffusivities on either side of equations (3.41) are equal and cancel each other out.

Coordinate transformation

In order to apply the Chebyshev orthogonal collocation discretisation, equations (3.38) must be rescaled on the computational domain $\bar{x}$ using the following changes

of variable, which map each sub-domains to $[-1, 1]$.

$$\begin{cases} \bar{x} = \frac{2}{\delta_1}\left(x - \frac{\delta_1}{2}\right) & \text{for} \quad x \in [0, L_{12}] \\ \bar{x} = \frac{2}{\delta_2}\left(x - \frac{\delta_2}{2}\right) + L_{12} & \text{for} \quad x \in [L_{12}, L_{23}] \\ \bar{x} = \frac{2}{\delta_3}\left(x - \frac{\delta_3}{2}\right) + L_{23} & \text{for} \quad x \in [L_{23}, L_3] \end{cases} \tag{3.42}$$

Considering the changes of variable (3.42) and using the chain rule, one can show that

$$\frac{\partial}{\partial x} = \frac{2}{\delta_i}\frac{\partial}{\partial \bar{x}} \quad \text{and} \quad \frac{\partial^2}{\partial x^2} = \frac{4}{\delta_i^2}\frac{\partial^2}{\partial \bar{x}^2}. \tag{3.43}$$

Therefore, under the coordinate transformation (3.42) the diffusion equations (3.38) become:

$$\begin{cases} \frac{\partial c_1}{\partial t} = \frac{4\epsilon_1^{b_1}}{\delta_1^2}\left(D\frac{\partial^2 c_1}{\partial \bar{x}^2} + \frac{\partial D}{\partial c_1}\left(\frac{\partial c_1}{\partial \bar{x}}\right)^2\right) + \frac{a_{s,1}}{\epsilon_1 \mathcal{F}}\left(1 - t_+\right) j_1 \\ \frac{\partial c_2}{\partial t} = \frac{4\epsilon_2^{b_2}}{\delta_2^2}\left(D\frac{\partial^2 c_2}{\partial \bar{x}^2} + \frac{\partial D}{\partial c_2}\left(\frac{\partial c_2}{\partial \bar{x}}\right)^2\right) \\ \frac{\partial c_3}{\partial t} = \frac{4\epsilon_3^{b_3}}{\delta_3^2}\left(D\frac{\partial^2 c_3}{\partial \bar{x}^2} + \frac{\partial D}{\partial c_3}\left(\frac{\partial c_3}{\partial \bar{x}}\right)^2\right) + \frac{a_{s,3}}{\epsilon_3 \mathcal{F}}\left(1 - t_+\right) j_3 \end{cases} \tag{3.44}$$

Similarly, the zero-flux boundary conditions at the current collectors (3.39) is written

$$\left.\frac{\partial c_1}{\partial \bar{x}}\right|_{\bar{x}=-1} = 0 \quad \text{and} \quad \left.\frac{\partial c_3}{\partial \bar{x}}\right|_{\bar{x}=+1} = 0, \tag{3.45}$$

the continuity conditions (3.40) remain

$$c_1(\bar{x} = +1) = c_2(\bar{x} = -1) \quad \text{and} \quad c_2(\bar{x} = +1) = c_3(\bar{x} = -1), \tag{3.46}$$

and the interface flux equality conditions (3.41) are given by

$$\frac{2\epsilon_1^{b_1}}{\delta_1} D \left.\frac{\partial c_1}{\partial \bar{x}}\right|_{\bar{x}=+1} = \frac{2\epsilon_2^{b_2}}{\delta_2} D \left.\frac{\partial c_2}{\partial \bar{x}}\right|_{\bar{x}=-1} \quad \text{and} \quad \frac{2\epsilon_2^{b_2}}{\delta_2} D \left.\frac{\partial c_2}{\partial \bar{x}}\right|_{\bar{x}=+1} = \frac{2\epsilon_3^{b_3}}{\delta_3} D \left.\frac{\partial c_3}{\partial \bar{x}}\right|_{\bar{x}=-1}. \tag{3.47}$$

Domain patching using boundary conditions

The anode Ω_1, separator Ω_2 and cathode Ω_3 sub-domains rescaled on $\bar{x} \in [-1\,,\,1]$ are discretised using different numbers of Chebyshev nodes $M+1$, $K+1$ and $Q+1$ respectively, with $M, K, Q \in \mathbb{N}$, yielding a total number of $M+K+Q+3$ collocation points across the cell as shown on figure 3.2.

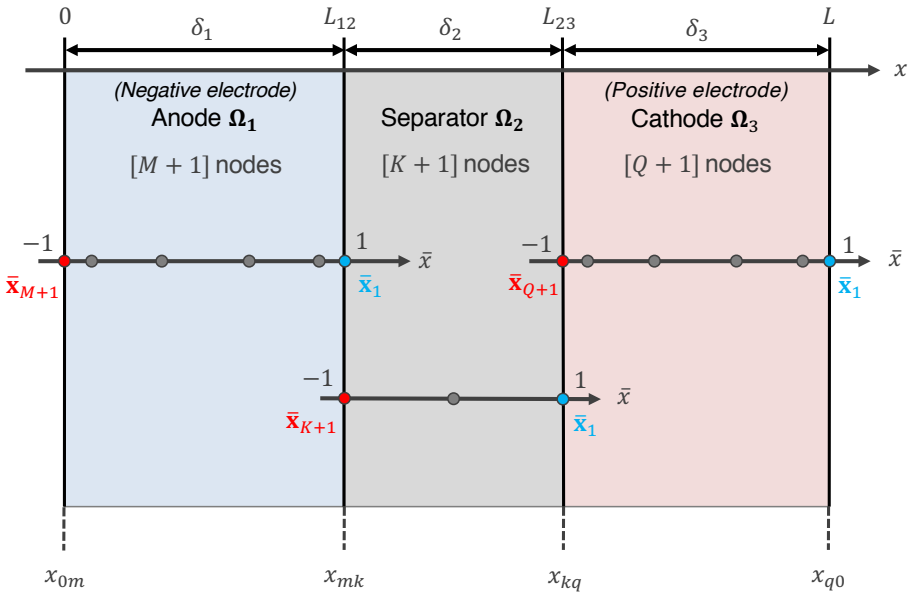

Fig. 3.2 Schematic of the three sub-domains of the macro-scale model discretised with $M+1$, $K+1$ and $Q+1$ Chebyshev nodes $\bar{x}$ in the anode Ω_1, cathode Ω_2 and separator Ω_3 sub-domains respectively.

Notation 6 *The vectors containing the concentration, first- and second-derivative values at the collocation nodes are denoted respectively* $\mathbf{c}_m, \mathbf{c}'_m, \mathbf{c}''_m \in \mathbb{R}^{M+1}$ *in the anode,* $\mathbf{c}_k, \mathbf{c}'_k, \mathbf{c}''_k \in \mathbb{R}^{K+1}$ *in the separator and* $\mathbf{c}_q, \mathbf{c}'_q, \mathbf{c}''_q \in \mathbb{R}^{Q+1}$ *in cathode sub-domains.*

The discrete approximation to the first- and second-derivative of the concentration at the collocation nodes are given respectively in the rescaled anode, separator

and cathode domains by

$$\mathbf{c}'_m = \mathrm{D}'_M \mathbf{c}_m \quad \text{and} \quad \mathbf{c}''_m = \mathrm{D}''_M \mathbf{c}_m \tag{3.48}$$

$$\mathbf{c}'_k = \mathrm{D}'_K \mathbf{c}_k \quad \text{and} \quad \mathbf{c}''_k = \mathrm{D}''_K \mathbf{c}_k \tag{3.49}$$

$$\mathbf{c}'_q = \mathrm{D}'_Q \mathbf{c}_q \quad \text{and} \quad \mathbf{c}''_q = \mathrm{D}''_Q \mathbf{c}_q \tag{3.50}$$

where the first- and second-derivative Chebyshev differentiation matrices on $[-1\,,\,1]$ are denoted $\mathrm{D}'_M, \mathrm{D}''_M$ in the anode, $\mathrm{D}'_K, \mathrm{D}''_K$ in the separator and $\mathrm{D}'_Q, \mathrm{D}''_Q$ in the cathode sub-domains following the convention in Notation 2. By considering the six equations at the boundaries of the sub-domains, the two boundary conditions (3.45), the two continuity conditions (3.46) and the two interface flux equality conditions (3.47), the number of discrete concentration values to be considered can be reduced by six from $M + K + Q + 3$ to $M + K + Q - 3$. Firstly, a single concentration value common to two contiguous domains can be considered at each electrode/separator interface according to the continuity equations (3.46), hence reducing the number of discrete concentration values by two.

Notation 7 *The concentration values at the anode and cathode current collectors are subsequently denoted c_{0m} and c_{q0} respectively and the concentration values common to two contiguous domains are denoted c_{mk} and c_{kq} at the anode/separator and separator/cathode interfaces respectively.*

Notation 8 *The vectors containing the values of concentration at the inner nodes of each sub-domain, obtained by removing the boundary values, are denoted $\bar{\mathbf{c}}_m$, $\bar{\mathbf{c}}_k$ and $\bar{\mathbf{c}}_q$ in the anode, separator and cathode.*

Secondly, the four remaining flux boundary conditions (3.45)– (3.47) can be used to express four discrete concentration values at the Chebyshev nodes in terms of all the others. A natural choice consists in expressing the concentration values at the anode current collector c_{0m}, the anode/separator interface c_{mk}, the

separator/cathode interface c_{kq} and the cathode current collector c_{q0} as a function of the concentration values at the inner nodes of each sub-domain denoted $\bar{c}_m$, $\bar{c}_k$ and $\bar{c}_q$. The scaled first-derivative Chebyshev differentiation matrices that account for the domain length δ_i and porosity $\epsilon_i^{b_i}$ are defined according to

$$\tilde{\mathrm{D}}'_M = \frac{4\epsilon_1^{b_1}}{\delta_1^2}\mathrm{D}'_M \quad , \quad \tilde{\mathrm{D}}'_K = \frac{4\epsilon_2^{b_2}}{\delta_2^2}\mathrm{D}'_K \quad \text{and} \quad \tilde{\mathrm{D}}'_Q = \frac{4\epsilon_3^{b_3}}{\delta_3^2}\mathrm{D}'_Q. \tag{3.51}$$

Therefore, the discrete version of the boundary conditions at the current collectors (3.45) are given by

$$\left[\tilde{\mathrm{D}}'_Q\right]_{1,1} c_{q0} + \left[\tilde{\mathrm{D}}'_Q\right]_{1,Q+1} c_{qk} = -\left[\tilde{\mathrm{D}}'_Q\right]_{1,2:Q} \bar{\mathbf{c}}_q \tag{3.52}$$

$$\left[\tilde{\mathrm{D}}'_M\right]_{M+1,M+1} c_{m0} + \left[\tilde{\mathrm{D}}'_M\right]_{1,M+1} c_{km} = -\left[\tilde{\mathrm{D}}'_M\right]_{1,2:M} \bar{\mathbf{c}}_m. \tag{3.53}$$

Similarly, the discrete version of the flux equality conditions at the separator/cathode and anode/separator interfaces (3.47) are given respectively by

$$\left[\tilde{\mathrm{D}}'_Q\right]_{Q+1,1} c_{q0} - \left(\left[\tilde{\mathrm{D}}'_K\right]_{1,1} - \left[\tilde{\mathrm{D}}'_Q\right]_{Q+1,Q+1}\right) c_{kq} \left[\tilde{\mathrm{D}}'_K\right]_{1,K+1} c_{mk} = -\left[\tilde{\mathrm{D}}'_Q\right]_{Q+1,2:Q} \bar{\mathbf{c}}_q + \left[\tilde{\mathrm{D}}'_K\right]_{1,2:K} \bar{\mathbf{c}}_k \tag{3.54}$$

and

$$\left[\tilde{\mathrm{D}}'_K\right]_{K+1,1} c_{kq} - \left(\left[\tilde{\mathrm{D}}'_M\right]_{1,1} - \left[\tilde{\mathrm{D}}'_K\right]_{K+1,K+1}\right) c_{mk} - \left[\tilde{\mathrm{D}}'_M\right]_{1,M+1} c_{0m} = -\left[\tilde{\mathrm{D}}'_K\right]_{K+1,2:K} \bar{\mathbf{c}}_k + \left[\tilde{\mathrm{D}}'_M\right]_{M,2:M} \bar{\mathbf{c}}_m. \tag{3.55}$$

Equations (3.52)-(3.53)-(3.54)-(3.55) form a linear system of four equations relating the four boundary values of concentration c_{0m}, c_{mk}, c_{kq} and c_{q0} to the concentration values at the inner nodes of the sub-domains $\bar{c}_m$, $\bar{c}_k$ and $\bar{c}_q$. This linear system of

equations can be written more concisely using the matrix notation

$$\mathrm{A}\begin{bmatrix} c_{q0} \\ c_{kq} \\ c_{mk} \\ c_{0m} \end{bmatrix} = \mathrm{B}\begin{bmatrix} \overline{\mathbf{c}}_q \\ \overline{\mathbf{c}}_k \\ \overline{\mathbf{c}}_m \end{bmatrix}, \tag{3.56}$$

where the matrix $\mathrm{A} \in \mathbb{R}^{4\times4}$ is given by

$$\mathrm{A} = \begin{bmatrix} \left[\tilde{\mathrm{D}}'_Q\right]_{1,1} & \left[\tilde{\mathrm{D}}'_Q\right]_{1,Q+1} & 0 & 0 \\ \left[\tilde{\mathrm{D}}'_Q\right]_{Q+1,1} & -\left[\tilde{\mathrm{D}}'_K\right]_{1,1} + \left[\tilde{\mathrm{D}}'_Q\right]_{Q+1,Q+1} & -\left[\tilde{\mathrm{D}}'_K\right]_{1,K+1} & 0 \\ 0 & \left[\tilde{\mathrm{D}}'_K\right]_{K+1,1} & -\left[\tilde{\mathrm{D}}'_M\right]_{1,1} + \left[\tilde{\mathrm{D}}'_K\right]_{K+1,K+1} & -\left[\tilde{\mathrm{D}}'_M\right]_{1,M+1} \\ 0 & 0 & \left[\tilde{\mathrm{D}}'_M\right]_{M+1,1} & \left[\tilde{\mathrm{D}}'_M\right]_{M+1,M+1} \end{bmatrix}, \tag{3.57}$$

and the matrix $B \in \mathbb{R}^{4\times(Q+K+M-3)}$ is given by

$$\mathrm{B} = \begin{bmatrix} -\left[\tilde{\mathrm{D}}'_Q\right]_{1,2:Q} & 0 & 0 \\ -\left[\tilde{\mathrm{D}}'_Q\right]_{Q+1,2:Q} & \left[\tilde{\mathrm{D}}'_K\right]_{1,2:K} & 0 \\ 0 & -\left[\tilde{\mathrm{D}}'_K\right]_{K+1,2:K} & \left[\tilde{\mathrm{D}}'_M\right]_{1,2:M} \\ 0 & 0 & -\left[\tilde{\mathrm{D}}'_M\right]_{M+1,2:M} \end{bmatrix}. \tag{3.58}$$

Assuming that A is non singular and defining the matrix $\mathrm{M} \triangleq \mathrm{A}^{-1}\mathrm{B}$ yields

$$\begin{bmatrix} c_{q0} \\ c_{kq} \\ c_{mk} \\ c_{0m} \end{bmatrix} = \mathrm{M}\begin{bmatrix} \overline{\mathbf{c}}_q \\ \overline{\mathbf{c}}_k \\ \overline{\mathbf{c}}_m \end{bmatrix}. \tag{3.59}$$

The system of equation (3.59) therefore relates the values of concentration at boundaries to the ones at the inner nodes in each sub-domain and can be used to derive a second-derivative differentiation matrix for the diffusion equations (3.44)

that automatically satisfy the boundary and interface conditions (3.45) through (3.47).

Differentiation matrices $\bar{\mathrm{D}}'_{321}$ and $\bar{\mathrm{D}}''_{321}$

Using (3.48) through (3.50), expressions for the second-derivative values of concentration at the inner nodes in each sub-domain are given by

$$\bar{\mathbf{c}}''_q = \left[\mathrm{D}''_Q\right]_{2:Q,1} c_{q0} + \left[\mathrm{D}''_Q\right]_{2:Q,2:Q} \bar{\mathbf{c}}_q + \left[\mathrm{D}''_Q\right]_{2:Q,Q+1} c_{kq} \tag{3.60}$$

$$\bar{\mathbf{c}}''_k = \left[\mathrm{D}''_K\right]_{2:K,1} c_{kq} + \left[\mathrm{D}''_K\right]_{2:K,2:K} \bar{\mathbf{c}}_k + \left[\mathrm{D}''_K\right]_{2:K,K+1} c_{mk} \tag{3.61}$$

$$\bar{\mathbf{c}}''_m = \left[\mathrm{D}''_M\right]_{2:M,1} c_{mk} + \left[\mathrm{D}''_M\right]_{2:M,2:M} \bar{\mathbf{c}}_m + \left[\mathrm{D}''_M\right]_{2:M,M+1} c_{0m}, \tag{3.62}$$

which can be written equivalently in the matrix form

$$\begin{bmatrix} \bar{\mathbf{c}}''_q \\ \bar{\mathbf{c}}''_k \\ \bar{\mathbf{c}}''_m \end{bmatrix} = \begin{bmatrix} \left[\mathrm{D}''_Q\right]_{2:Q,2:Q} & 0 & 0 \\ 0 & \left[\mathrm{D}''_K\right]_{2:K,2:K} & 0 \\ 0 & 0 & \left[\mathrm{D}''_M\right]_{2:M,2:M} \end{bmatrix} \begin{bmatrix} \bar{\mathbf{c}}_q \\ \bar{\mathbf{c}}_k \\ \bar{\mathbf{c}}_m \end{bmatrix} + \begin{bmatrix} \left[\mathrm{D}''_Q\right]_{2:Q,1} & \left[\mathrm{D}''_Q\right]_{2:Q,Q+1} & 0 & 0 \\ 0 & \left[\mathrm{D}''_K\right]_{2:K,1} & \left[\mathrm{D}''_K\right]_{2:K,K+1} & 0 \\ 0 & 0 & \left[\mathrm{D}''_M\right]_{2:M,1} & \left[\mathrm{D}''_M\right]_{2:M,M+1} \end{bmatrix} \begin{bmatrix} c_{q0} \\ c_{kq} \\ c_{mk} \\ c_{0m} \end{bmatrix} \tag{3.63}$$

Substituting the vector of boundary values by its expression (3.59) and defining the vectors $\bar{\mathbf{c}} = \left[\bar{\mathbf{c}}_q, \bar{\mathbf{c}}_k, \bar{\mathbf{c}}_m\right]^{\mathrm{T}}$ and $\bar{\mathbf{c}}'' = \left[\bar{\mathbf{c}}''_q, \bar{\mathbf{c}}''_k, \bar{\mathbf{c}}''_m\right]^{\mathrm{T}}$, the values of the second-derivative of the concentration at the inner nodes of the sub-domains are given by

$$\bar{\mathbf{c}}'' = \bar{\mathrm{D}}''_{321} \bar{\mathbf{c}} \tag{3.64}$$

with the second-derivative differentiation matrix $\bar{\mathrm{D}}''_{123}$ for the three sub-domains, a square matrix of size $M + K + Q - 3$, which automatically satisfy the boundary

and interface conditions defined as

$$\bar{\mathrm{D}}''_{321} = \begin{bmatrix} \left[\mathrm{D}''_Q\right]_{2:Q,2:Q} & 0 & 0 \\ 0 & \left[\mathrm{D}''_K\right]_{2:K,2:K} & 0 \\ 0 & 0 & \left[\mathrm{D}''_M\right]_{2:M,2:M} \end{bmatrix} + \begin{bmatrix} \left[\mathrm{D}''_Q\right]_{2:Q,1} & \left[\mathrm{D}''_Q\right]_{2:Q,Q+1} & 0 & 0 \\ 0 & \left[\mathrm{D}''_K\right]_{2:K,1} & \left[\mathrm{D}''_K\right]_{2:K,K+1} & 0 \\ 0 & 0 & \left[\mathrm{D}''_M\right]_{2:M,1} & \left[\mathrm{D}''_M\right]_{2:M,M+1} \end{bmatrix} \mathrm{M}. \quad (3.65)$$

Using a similar argument, the discrete values of the first-derivative are given by $\bar{\mathbf{c}}' = \bar{\mathrm{D}}'_{321}\bar{\mathbf{c}}$ with the first-derivative differentiation matrix $\bar{\mathrm{D}}'_{321}$ of size $M+K+Q-3$

$$\bar{\mathrm{D}}'_{321} = \begin{bmatrix} \left[\mathrm{D}'_Q\right]_{2:Q,2:Q} & 0 & 0 \\ 0 & \left[\mathrm{D}'_K\right]_{2:K,2:K} & 0 \\ 0 & 0 & \left[\mathrm{D}'_M\right]_{2:M,2:M} \end{bmatrix} + \begin{bmatrix} \left[\mathrm{D}'_Q\right]_{2:Q,1} & \left[\mathrm{D}'_Q\right]_{2:Q,Q+1} & 0 & 0 \\ 0 & \left[\mathrm{D}'_K\right]_{2:K,1} & \left[\mathrm{D}'_K\right]_{2:K,K+1} & 0 \\ 0 & 0 & \left[\mathrm{D}'_M\right]_{2:M,1} & \left[\mathrm{D}'_M\right]_{2:M,M+1} \end{bmatrix} \mathrm{M} \quad (3.66)$$

Therefore, the first- and second-derivative differentiation matrices $\bar{\mathrm{D}}'_{321}$ and $\bar{\mathrm{D}}''_{321}$ constitute the discrete approximations to linear differential operators $\partial/\partial x$ and $\partial^2/\partial x^2$ in the diffusion equation (3.37). These matrices can be used to write the discrete approximation of the electrolyte diffusion equation according to

$$\frac{\partial \bar{\mathbf{c}}}{\partial t} = \epsilon^b \mathrm{diag}\left(\bar{\mathbf{D}}\right)\left(\mathrm{D}''_{321}\bar{\mathbf{c}}\right) + \epsilon^b \mathrm{diag}\left(\bar{\mathbf{D}}'_{\mathbf{c}}\right)\left(\mathrm{D}'_{321}\bar{\mathbf{c}}\right)^2 + \frac{a_\mathrm{s}\left(1-t_+\right)}{\epsilon}\bar{\mathbf{j}}. \quad (3.67)$$

where $\bar{\mathbf{c}}, \bar{\mathbf{j}}, \bar{\mathbf{D}}, \bar{\mathbf{D}}'_{\mathbf{c}} \in \mathbb{R}^{M+K+Q-3}$ are the vectors containing the concatenated values at the inner Chebyshev nodes of each sub-domains of electrolyte concentration c, reaction rate j, concentration-dependent diffusivity D and partial derivative of

diffusivity w.r.t. concentration $\partial D/\partial c$ respectively. For clarity, the parameters ϵ, b and a_s in (3.67) have been written as constant scalars; however the value of these parameters are actually different in each sub-domain and these must therefore be defined as diagonal matrices of the appropriate size in (3.67).

3.2.4 Electrolyte and solid-phase current densities

As shown by the divergence equation (2.2), the electrolyte current density i_e can be computed directly from the reaction rate j. However, in order to minimise the number of algebraic variables required to implement the model, the integral forms of (2.2) given by (2.16) in the anode (with the integration constant equal to zero) and (2.17) in the cathode (with the integration constant equal to i_app) are preferred, since these equations give explicit expressions for i_e in terms of j. Note that the integration constants in (2.16) and (2.17) are equal to zero and i_app in the anode and cathode respectively, because the electrolyte current density is equal to i_app across the separator. Using the Chebyshev integration matrices I_M and I_Q defined in Section 3.1.3 for the anode and cathode domains respectively, the electrolyte current densities in the anode and cathode domains are given by

$$\mathbf{i}_{\mathrm{e},1} = a_{\mathrm{s},1}\mathcal{F}\frac{\delta_1}{2}\left(\mathrm{I}_M\,\mathbf{j}_1\right) \tag{3.68}$$

$$\mathbf{i}_{\mathrm{e},3} = a_{\mathrm{s},3}\mathcal{F}\frac{\delta_3}{2}\left(\mathrm{I}_Q\,\mathbf{j}_3\right) + \mathbf{i}_\mathrm{app} \tag{3.69}$$

where $\mathbf{i}_{\mathrm{e},1}, \mathbf{j}_1 \in \mathbb{R}^{M+1}$ and $\mathbf{i}_{\mathrm{e},3}, \mathbf{j}_3 \in \mathbb{R}^{Q+1}$ denote the vectors of electrolyte current density i_e and reaction rate j values at the collocation nodes in the anode and cathode domains respectively. All the elements of the vector $\mathbf{i}_\mathrm{app} \in \mathbb{R}^{Q+1}$ are equal to the applied current density i_app. Note that the factor $\delta/2$ appearing in both equation arises from the rescaling of the model equation on $[-1\,,\,1]$. The computation of the solid-phase current density values in both electrodes is

straightforward from the electrolyte current density using Kirchhoff's law (2.1) according to $\mathbf{i}_{\mathrm{s}} = \mathbf{i}_{\mathrm{app}} - \mathbf{i}_{\mathrm{e}}$.

3.2.5 Solid-phase and electrolyte potentials

Similarly to the electrolyte current density, the Ohm's law (2.12) and MacInnes' equation (2.13) governing the solid-phase and electrolyte potential respectively are used in their integral form rather than differential to minimize the number of algebraic constraints in the model implementation. Therefore, the Ohm's law in the anode and cathode (2.12) domains become respectively

$$\tilde{\phi}_{\mathrm{s}}(x) = \frac{-1}{\sigma^{\mathrm{eff}}} \int_{x'=0}^{x} i_{\mathrm{s}}(x')\, dx' \quad \text{for} \quad x \in \Omega_1 \tag{3.70}$$

$$\tilde{\phi}_{\mathrm{s}}(x) = \frac{-1}{\sigma^{\mathrm{eff}}} \left(\int_{x'=L_{23}}^{x} i_{\mathrm{s}}(x')\, dx' - \int_{x'=L_{23}}^{L} i_{\mathrm{s}}(x')\, dx' \right) \quad \text{for} \quad x \in \Omega_3 \tag{3.71}$$

The integration constants in (3.70) and (3.71) are chosen so that the potential $\tilde{\phi}_{\mathrm{s}}$ is equal to zero at each current collectors for $x = 0$ and $x = L$. Therefore, the discrete value of solid-phase potential $\tilde{\phi}_{\mathrm{s}}$ in the anode and cathode are respectively given by

$$\tilde{\mathbf{\Phi}}_{\mathrm{s},1} = \frac{-1}{\sigma_1^{\mathrm{eff}}} \frac{\delta_1}{2} \left(\mathrm{I}_M\, \mathbf{i}_{\mathrm{s},1} \right) \tag{3.72}$$

$$\tilde{\mathbf{\Phi}}_{\mathrm{s},3} = \frac{-1}{\sigma_3^{\mathrm{eff}}} \frac{\delta_3}{2} \left(\mathrm{I}_Q - \mathbf{1}_Q \mathbf{w}_Q^{\mathrm{T}} \right) \mathbf{i}_{\mathrm{s},1} \tag{3.73}$$

where $\mathbf{1}_Q \in \mathbb{R}^{Q+1}$ denotes a column vector whose elements are all ones, and $\mathbf{w}_Q$ denotes the Clenshaw–Curtis quadrature weights[2] defined in Section 3.1.3.

As discussed in Section 2.1.5, the values of solid-phase potential at the current collectors $\phi_{\mathrm{s},1}^{\mathrm{cc}}$ and $\phi_{\mathrm{s},3}^{\mathrm{cc}}$ are obtained implicitly by solving the two algebraic constraints given by (2.18) and (2.19). In their discrete forms, these scalar algebraic

[2]Note that instead of using the the term $\left(\mathrm{I}_Q - \mathbf{1}_Q \mathbf{w}_Q^{\mathrm{T}} \right)$ in (3.73) one may use the integration matrix I_Q with flipped rows to enforce $\tilde{\phi}_{\mathrm{s}}(\bar{x} = 1) = 0$.

constraints are given in the anode and cathode respectively by

$$0 = a_{\mathrm{s},1}\mathcal{F}\frac{\delta_1}{2}\mathbf{w}_M^{\mathrm{T}}\mathbf{j}_1 - i_{\mathrm{app}} \quad \text{and} \quad 0 = a_{\mathrm{s},3}\mathcal{F}\frac{\delta_3}{2}\mathbf{w}_Q^{\mathrm{T}}\mathbf{j}_3 + i_{\mathrm{app}}. \tag{3.74}$$

The computation of the electrolyte potential is a bit more involved because the continuity of the potential must be enforce at the electrode/separator interfaces. The MacInnes' equation (2.13) in its differential form in one of the cell sub-domain i can be expressed as

$$\phi_{\mathrm{e},i}(\bar{x}) = \frac{\delta_i}{2}\int_{\bar{x}'=-1}^{\bar{x}} \frac{i_{\mathrm{e}}(\bar{x}')}{\kappa_i^{\mathrm{eff}}(\bar{x}')}d\bar{x}' + \frac{2(1-t_+)RT}{\mathcal{F}}\ln c_{\mathrm{e},i}(\bar{x}) + C_i \quad \text{in} \quad \Omega_i, \tag{3.75}$$

where C_i is the integration constant in each sub-domain i. By enforcing the continuity of the electrolyte potential, *i.e.* so that $\phi_{\mathrm{e},1}(1) = \phi_{\mathrm{e},2}(-1)$ and $\phi_{\mathrm{e},2}(1) = \phi_{\mathrm{e},3}(-1)$, and recalling that potential at the cathode current collector $\phi_{\mathrm{e},3}(1)$ is equal to zero (since it has been chosen as reference potential in Section 2.1.5), the integration constants are given by

$$C_3 = \frac{\delta_3}{2}\int_{-1}^{1} \frac{i_{\mathrm{e},3}(\bar{x})}{\kappa_3^{\mathrm{eff}}(\bar{x})}d\bar{x} - \frac{2(1-t_+)RT}{\mathcal{F}}\ln c_{\mathrm{e},3}(1) \tag{3.76}$$

$$C_2 = \frac{\delta_2}{2}\int_{-1}^{1} \frac{i_{\mathrm{e},2}(\bar{x})}{\kappa_2^{\mathrm{eff}}(\bar{x})}d\bar{x} - \frac{2(1-t_+)RT}{\mathcal{F}}\ln c_{\mathrm{e},2}(1) + \phi_{\mathrm{e},3}(-1) \tag{3.77}$$

$$C_1 = \frac{\delta_1}{2}\int_{-1}^{1} \frac{i_{\mathrm{e},1}(\bar{x})}{\kappa_1^{\mathrm{eff}}(\bar{x})}d\bar{x} - \frac{2(1-t_+)RT}{\mathcal{F}}\ln c_{\mathrm{e},1}(1) + \phi_{\mathrm{e},2}(-1). \tag{3.78}$$

The computation of the discrete values of electrolyte potential $\mathbf{\Phi}_{\mathrm{e}}$ in each sub-domain from the current densities $\mathbf{i}_{\mathrm{e}}$ and concentration $\mathbf{c}_{\mathrm{e}}$ values is straightforward by substituting the continuous variables and integral operators in (3.75) and (3.76) through (3.78) by their discrete counterparts[3] in (3.72) and (3.73).

[3]Similarly to (3.73), the definite integrals in (3.76) through (3.78) vanish if the Chebyshev integration matrix with flipped rows (as computed by *cumsummat.m*) is used.

3.2.6 Reaction rate

Finally, the reaction rate values $\mathbf{j}$ are computed by solving algebraic constraints at each of the nodes in both electrodes (see Section 2.1.5) using the Butler–Volmer equation (2.9) according to:

$$\mathbf{0} = \mathbf{j} - \frac{\operatorname{diag}(\mathbf{i}_0)}{\mathcal{F}}\left[\exp\left(\frac{\alpha_\mathrm{a}\mathcal{F}}{RT}\boldsymbol{\eta}\right) - \exp\left(\frac{-\alpha_\mathrm{c}\mathcal{F}}{RT}\boldsymbol{\eta}\right)\right], \tag{3.79}$$

where the exchange current density values $\mathbf{i}_0$ are computed from the particles surface and electrolyte concentration values $\mathbf{c}_\mathrm{s}^\mathrm{surf}$ and $\mathbf{c}_\mathrm{e}$ respectively using (2.10), and the overpotential values $\boldsymbol{\eta}$ are given by (2.11) in terms of the solid-phase potential $\tilde{\boldsymbol{\Phi}}_\mathrm{s}$, $\boldsymbol{\Phi}_\mathrm{s}^\mathrm{cc}$, the electrolyte potential $\boldsymbol{\Phi}_\mathrm{e}$ and the open-circuit potential $\mathbf{U}$, which is a function of $\mathbf{c}_\mathrm{s}^\mathrm{surf}$ as discussed in Section 2.1.4.

3.2.7 Thermal model

The thermal model presented in Section 2.3 is a bulk model assuming uniform temperature T, which is a scalar computed by integrating the ODE (2.30) in time. Although there is no need for spatial discretisation of the thermal model, the heat generation contributions given in (2.35) through (2.37) are averaged values of the distributed variables over each sub-domain of the electrochemical model. Deriving the integrals is straightforward by substituting the continuous integral operator in (2.35) through (2.37) by the discrete Clenshaw–Curtis weights for each subdomains $\mathbf{w}_M^\mathrm{T}$, $\mathbf{w}_K^\mathrm{T}$ and $\mathbf{w}_Q^\mathrm{T}$, rescaled appropriately by $\delta_i/2$.

3.3 A semi-explicit DAEs system

3.3.1 DAE state-space formulation of the discretised model

The P2D model discretised by orthogonal collocation consists of a set of non-linear differential-algebraic equations (DAEs) with respect to time. Using a state-space

representation as already introduced in section 2.1.5, the model can be conveniently written as a semi-explicit DAE system, consisting of a set of differential (3.80) and algebraic equations (3.81):

$$\dot{\mathbf{x}} = \mathbf{f}\left(\mathbf{x}, \mathbf{z}, u\right) \tag{3.80}$$

$$\mathbf{0} = \mathbf{g}\left(\mathbf{x}, \mathbf{z}, u\right) \tag{3.81}$$

where the functions $\mathbf{f}$ and $\mathbf{g}$ are non-linear mapping functions derived from the discretised model equations given in Section 3.2. The state vector $\mathbf{x} \in \mathbb{R}^{n_x}$ associated with the differential equations contains the value at the collocation points of the solid-phase concentration $u_\mathrm{s} = rc_\mathrm{s}$ and the electrolyte concentration c_e, as well as the bulk temperature T:

$$\mathbf{x} = \left[\bar{\mathbf{u}}_{\mathrm{s},3}\,,\ \bar{\mathbf{u}}_{\mathrm{s},1}\,,\ \bar{\mathbf{c}}_\mathrm{e}\,,\ T\right]^\mathrm{T} \tag{3.82}$$

The vectors $\bar{\mathbf{u}}_{\mathrm{s},3} \in \mathbb{R}^{(N-1)\times(Q+1)}$ and $\bar{\mathbf{u}}_{\mathrm{s},1} \in \mathbb{R}^{(N-1)\times(M+1)}$ combine the profiles of u_s at the inner collocation nodes (*i.e.* the vector $\bar{\mathbf{u}}$ as defined in Section 3.2.2) for all the particles in the cathode and anode respectively. The vector $\bar{\mathbf{c}}_\mathrm{e} \in \mathbb{R}^{Q+K+N-3}$ corresponds to $\bar{\mathbf{c}}$ defined in Section 3.2.3, which combines the electrolyte concentration values at the inner collocation nodes of the three sub-domains: cathode, separator and anode. Since the temperature T is a scalar, the number of differential state variables is therefore $n_x = N\left(Q + M + 2\right) + K - 4$.

The state vector $\mathbf{z} \in \mathbb{R}^{n_z}$ associated with the algebraic equations contains the values of volumetric reaction rate $\mathbf{j}_3 \in \mathbb{R}^{Q+1}$ and $\mathbf{j}_1 \in \mathbb{R}^{M+1}$ at the collocation points in the cathode and anode respectively, and the solid-phase electric potential at the cathode and anode current collector $\phi_{\mathrm{s},3}^{\mathrm{cc}}$ and $\phi_{\mathrm{s},1}^{\mathrm{cc}}$ respectively.

$$\mathbf{z} = \left[\mathbf{j}_3\,,\ \mathbf{j}_1\,,\ \phi_{\mathrm{s},3}^{\mathrm{cc}}\,,\ \phi_{\mathrm{s},1}^{\mathrm{cc}}\right]^\mathrm{T} \tag{3.83}$$

The total number of algebraic equations to solve in the model is therefore $n_z = Q + M + 4$.

The measurement vector $\mathbf{y} = [V \quad T]^{\mathrm{T}}$ containing the value of the voltage V and the temperature T is computed from the differential and algebraic state vectors according to the measurement equation (3.84). The input u is a scalar equal to the applied current I.

$$\mathbf{y} = [\mathrm{H}_x \quad \mathrm{H}_z] \begin{bmatrix} \mathbf{x} \\ \\ \mathbf{z} \end{bmatrix} + \mathrm{H}_u u \tag{3.84}$$

The derivation of matrices H_x, H_z and H_u is trivial since the temperature is a differential state of the model and the voltage computation is straightforward from the algebraic state vector and the input vector.

Equations (3.80), (3.81) and (3.84) constitute a state-space representation of the thermal-electrochemical P2D model. This representation is particularly convenient from a control engineering perspective and is useful for the design and implementation of a state estimator as discussed in Chapter 4.

3.3.2 Solution of DAE systems

As already discussed in Section 2.1.5, the system of equations (3.80)–(3.81) constituting the P2D electrochemical model is a differential-algebraic system. A system of DAEs can be expressed in its general form as [139]

$$F\left(t, y, \dot{y}\right) = 0 \tag{3.85}$$

$$y\left(t_0\right) = y_0 \tag{3.86}$$

$$\dot{y}\left(t_0\right) = \dot{y}_0 \quad , \tag{3.87}$$

where consistent values for the initial state y_0 and its first derivative with respect to time $\dot{y}_0$ must be provided. Solvers that can solve DAEs in this general form

include DASSL [140, 141], the IDA code from the SUNDIALS solver suite [142], the MATLAB® function *ode15i*, all based on backward differentiation formulas (BDFs), and RADAU5 [143] which uses implicit Range–Kutta method. It has often been reported in the battery modelling literature that these solvers fail when provided with non-consistent initial conditions [144] and many authors had to develop their own consistent initialization routines [144–146].

However, equations (3.80) and (3.81) constitute a particular form of DAEs, so-called *semi-explicit DAEs*, in which the state variables can be divided into differential $\mathbf{x}$ and algebraic $\mathbf{z}$ states. The algebraic constraint appears explicitly and the DAEs system can clearly be seen as a set of ODEs (3.80) to be solved while satisfying the constraint (3.81) on the model states. Variants of BDFs referred to as numerical differentiation formulas (NDFs) have been implemented in the MATLAB® solver *ode15s* [147], which allows solving such semi-explicit DAEs much like ODEs. The solver *ode15s* can be initialised with a non-consistent but 'close' initial guess for the model state variables and no guess for the time derivative. An initial guess for the state variables $\mathbf{x}$ and $\mathbf{z}$ of the P2D model is found relatively easily by assuming the battery at equilibrium. The initialisation of the differential variables in $\mathbf{x}$ is straightforward since the solid-phase concentration profiles c_s are uniform within each particle and equal to the initial concentration $c_\mathrm{s}^0 = x_\mathrm{s}^0 c_\mathrm{s}^\mathrm{max}$, the electrolyte concentration is uniform and equal to $c_\mathrm{e}^\mathrm{avg}$ across the cell and the initial temperature is assumed known. In regard to the state variables in $\mathbf{z}$, a good initial guess for the solid-phase potential $\phi_\mathrm{s}^\mathrm{cc}$ is given by the value of open-circuit potential at the initial stoichiometry in each electrode $U(x_\mathrm{s}^0)$, since over-potentials are null at equilibrium. A guess for the consistent initial reaction rate j is obtained by assuming uniform reaction rate within each electrode by using equations (2.22) and (2.23) of the SP model with the input current density i_app evaluated at t_{0+}. Generally, it was found that the solver *ode15s* could start and perform the P2D model integration using these values as initial guess. However, the solver failed at

integrating the model in some cases, for high C-rates especially, when the uniform reaction rate initial guess was far from the consistent values. For such cases, a consistent initial guess was provided to *ode15s* by solving the system of equations

$$\begin{cases} \mathbf{0} &= \mathbf{f}\left(t_{0+}, \mathbf{x}_0, \mathbf{z}_0\right) - \dot{\mathbf{x}}_0 \\ \mathbf{0} &= \mathbf{g}\left(t_{0+}, \mathbf{x}_0, \mathbf{z}_0\right) \end{cases} \tag{3.88}$$

for $\dot{\mathbf{x}}_0$ and $\mathbf{z}_0$ given the initial value $\mathbf{x}_0$ using the MATLAB® function *fsolve*.

The time integration of the P2D model using *ode15s* has proven fast and robust under constant current input. For discrete input values, such as the drive cycle mentioned in Section 3.4.4 however, the solution is more computationally intense because consistent initial conditions must be computed at each input discontinuity. This requires a large number of additional function calls, which can highly reduce computational speed. In order to remove these discontinuities, the input time-series was interpolated using piecewise interpolation techniques, including linear, cosine, cubic, Hermite cubic and monotone Hermite cubic splines, as shown on Figure 3.3. We found that the monotone Hermite cubic technique [148] was the most efficient at reducing the solution computational cost due to the highly smoothed interpolated current profile obtained.

3.4 P2D model performance

In this section, the performance of the MATLAB® implementation of the P2D model discretised using orthogonal collocation discussed in Section 3.2 and Section 3.3 is evaluated. The model prediction accuracy is tested against a higher-order finite-element implementation of the P2D model in the commercial software COMSOL Multiphysics®, subsequently referred to as the 'high-fidelity' model for simplicity. The implementation of the thermal-electrochemical P2D model in COMSOL® was performed using the equation-based modelling toolbox similarly

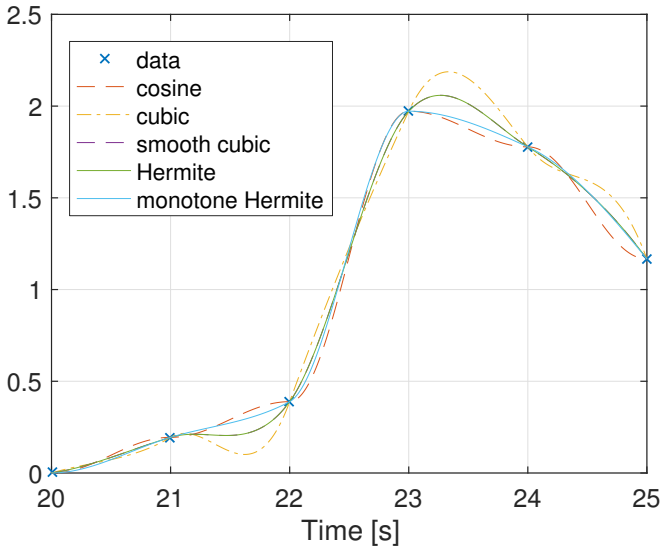

Fig. 3.3 Comparison of various piecewise interpolation techniques.

to [130] and is briefly discussed in a subsequent section. The model parameters used are taken from the literature for a typical LCO cell.

3.4.1 COMSOL® P2D model implementation

The COMSOL® implementation of the thermal-electrochemical P2D model discussed in [2] and Section 3.4 of this dissertation is similar to [130] and involves using the COMSOL® *PDE Interfaces* and the *ODE and DAE Interfaces* for equation-based modelling. The macro-scale cell model is described on a 1D geometry divided into three regions (anode, separator and cathode) in the x-direction. The micro-scale particle model is described on a 2D geometry in which the diffusion coefficients and electronic conductivities are set to zero in the x-direction [130]. This reduces the 2D geometry to a 1D geometry in the y-direction distributed along the cell thickness (x-direction) that is equivalent to the radial r-direction of the solid-phase spherical particles of the P2D model. The equations solved on the 1D and 2D geometries are coupled by projecting the local reaction rate j and the solid-phase surface concentration $c_{\mathrm{s}}^{\mathrm{surf}}$ from one geometry to the other using the *linear extrusion* COMSOL® function. The 1D geometry was discretised

using a uniformly spaced mesh with 22 elements, 8 elements and 21 elements in the anode, separator and cathode domains respectively. The 2D geometries of the electrodes were discretised using triangular elements for the core of the particles and quadrilateral elements at the surface of the particles. The anode was discretised with 890 triangular elements and 528 quadrilateral elements and the cathode with 588 triangular elements and 504 quadrilateral elements. This results in a COMSOL® finite-element model with 7,856 degrees of freedom.

3.4.2 Model parameters from literature

The cell considered in this section consists of a lithium cobalt oxide $LiCoO_2$ (LCO) cathode and a mesocarbon microbead (MCMB) anode with 1M $LiPF_6$ in propylene carbonate, ethylene carbonate and dimethyl carbonate (PC/EC/DMC) electrolyte. The parameters for this particular cell were found in the literature and are summarised in Table 3.1, while the parameters used in the bulk thermal model are given in Table 3.2. It has been shown that electrolyte properties are highly dependent on lithium concentration and cell temperature [92]. The empirical expressions for diffusivity D_e and ionic conductivity κ_e as a function of concentration and temperature reported in [92] were used and the transference number $t_+ = 0.435$ is assumed constant [129]. The reaction constants and solid-phase diffusivities are assumed temperature-dependent according to Arrhenius' law as discussed in Section 2.3.4.

3.4.3 Constant current discharge

Figure 3.4 compares the cell terminal voltage predicted by the P2D model solved using orthogonal collocation in MATLAB® and the high-fidelity COMSOL® model during constant current discharge at several C-rates ranging from $1\,C$ to $10\,C$. The chosen number of collocation nodes in the anode, separator and cathode are

Table 3.1 Parameters of the electrochemical P2D model [2].

Parameter	Units	Anode Li_xC_6	Separator $LiPF_6$	Cathode Li_yCoO_2	Ref.
δ_i	µm	73.5	25.0	70.0	[61]
R_i	µm	12.5	–	8.5	[61]
ϵ_i	–	0.4382	0.45	0.3	[129]
$\epsilon_{\mathrm{f},i}$	–	0.0566	–	0.15	[129]
α_i	–	0.5	–	0.5	[29]
k_i^{ref}	$\mathrm{m^{2.5}\,mol^{-0.5}\,s^{-1}}$	1.764×10^{-11}	–	6.667×10^{-11}	[129]
$D_{\mathrm{s},i}$	$\mathrm{m^2\,s^{-1}}$	5.5×10^{-14}	–	1.0×10^{-11}	[29]
σ_i	$\mathrm{S\,m^{-1}}$	100	–	10	[29]
b_i	–	4.1	2.3	1.5	[129]
$c_{\mathrm{s},i}^{\max}$	$\mathrm{mol\,m^{-3}}$	30 555	–	51 555	[45]
x_i^0	–	0.756	–	0.465	[61]

Table 3.2 Thermal model parameters [2].

Parameter	Units	Value	Ref.
c_{p}	$\mathrm{J\,kg^{-1}\,K^{-1}}$	750	[132]
ρ	$\mathrm{kg\,m^{-3}}$	1626	[132]
T^{ref}	K	298	[132]
h	$\mathrm{W\,m^{-2}\,K^{-1}}$	30	-
T_∞	K	298	-
$E_{\mathrm{act}}^{D_{\mathrm{s,neg}}}$	$\mathrm{kJ\,mol^{-1}}$	35	[132, 149]
$E_{\mathrm{act}}^{D_{\mathrm{s,pos}}}$	$\mathrm{kJ\,mol^{-1}}$	29	[132, 150]
$E_{\mathrm{act}}^{k_{\mathrm{neg}}}$	$\mathrm{kJ\,mol^{-1}}$	20	[132, 133]
$E_{\mathrm{act}}^{k_{\mathrm{pos}}}$	$\mathrm{kJ\,mol^{-1}}$	58	[132, 151]

$N_a = 6$, $N_s = 3$ and $N_c = 6$ respectively and the number of collocation nodes[4] in each particles of both electrodes is $N_p = 15$. The voltage predicted is in very good agreement with the high-fidelity model up to high C-rates ($10\,C$) with a root-mean square and a maximum error of 50 mV and 10 mV respectively. The solution of the model using Chebyshev orthogonal collocation is typically 30 times faster than the solution using COMSOL®. The computation of a single discharge curve on a desktop computer using a 3.40 GHz processor with 8 GB RAM is performed in about 1 s to 10 s in MATLAB® using orthogonal collocation compared to 5 min with COMSOL®. The order of magnitude of these computation times are consistent with results reported in [62], which used a Maple™ solver.

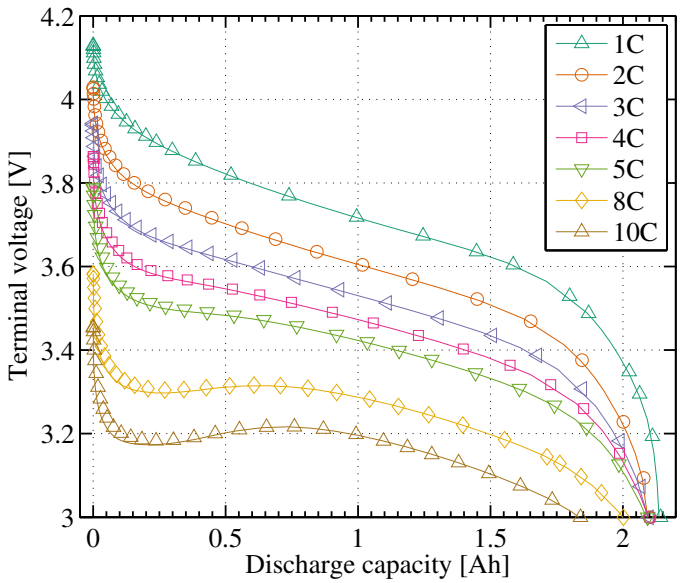

Fig. 3.4 Cell voltage under constant current discharge at several C-rates. Solid lines: COMSOL®, markers: Chebyshev orthogonal collocation in MATLAB® [2].

The number of collocation nodes required to discretise the cell domain depends on the C-rate, since higher C-rates result in larger gradients of dependent variables across the cell. In particular, the accuracy of results highly depends on the number of collocation nodes N_p in the solid-phase particles. This is due to the very sharp gradients of lithium concentration at the surface of these particles for medium

[4]Note that the number of nodes are related to the notation adopted in Section 3.2 according to $N_a = M + 1$, $N_s = K + 1$, $N_c = Q + 1$ and $N_p = N + 1$.

to high C-rates. The root-mean square and maximum absolute errors between the orthogonal collocation and the high-fidelity model for the $1C$, $2C$ and $5C$ full constant-current discharge with increasing number of nodes in the solid-phase particles are shown in Figure 3.5a and Figure 3.5b respectively. These graphs confirm that a larger number of collocation nodes results in smaller error on voltage prediction, and at higher C-rate more nodes are required. Although, it is suggested by the maximum error graph (Fig. 3.5b) that more collocation nodes are required for the $1C$ discharge cycle compared to higher C-rate, this is not representative of the whole discharge curve. The voltage maximum error arises from the very low SoC portion of the discharge curve, when the cell voltage rapidly drops due to the low concentration in the anode material. The maximum error tends to be smaller at higher C-rates compared to 1C because such a low anode concentration cannot be reached at higher C-rates.

An important state of the model for a BMS is the cell SoC. The bulk SoC of the electrode i can be defined according to:

$$SoC_i(t) = \frac{x_{\mathrm{s},i}^{\mathrm{avg}}(t) - x_{\mathrm{s},i}^{0\%}}{x_{\mathrm{s},i}^{100\%} - x_{\mathrm{s},i}^{0\%}} \tag{3.89}$$

where $x_{\mathrm{s},i}^{100\%}$ and $x_{\mathrm{s},i}^{0\%}$ denote the electrode stoichiometry at 100 % and 0 % SoC respectively. The average electrode stoichiometry $x_{\mathrm{s},i}^{\mathrm{avg}}$ is calculated by integrating the solid-phase concentration in each particle and across the cell according to (3.90). As shown in figure 3.5c, the maximum relative error on the bulk SoC in both the anode and the cathode rapidly falls below 1 % error with less than 10 nodes in the solid-phase particles and below 0.1 % with only 15 nodes up to $10C$.

$$x_{\mathrm{s},i}^{avg}(t) = \frac{3}{\delta_i R_{\mathrm{s},i}^3} \int_0^{\delta_i} \int_0^{R_{\mathrm{s},i}} r^2 \frac{c_{\mathrm{s},i}(x,r,t)}{c_{\mathrm{s},i}^{\max}} dr dx \tag{3.90}$$

The number of nodes required to discretise the macro-scale model also depends on the C-rate considered; this is because higher currents yield larger concentration

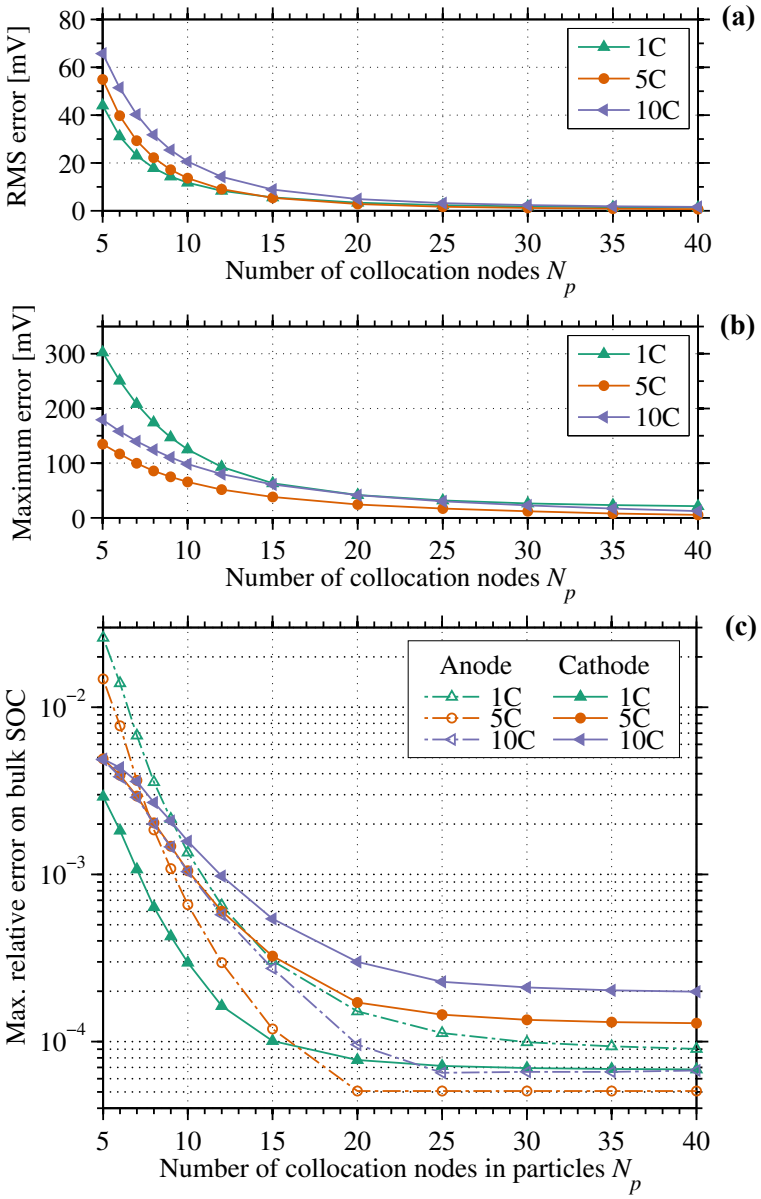

Fig. 3.5 RMS error (a) and maximum absolute error (b) on voltage, and maximum relative error on bulk SoC in both electrodes (c) predicted by the P2D model compared to the high-fidelity model under constant-current discharge at several C-rates with respect to the number of collocation nodes in each solid-phase particles N_p [2].

and potential gradients across the cell. Because of the chosen model implementation, which uses the PDEs' boundary conditions to reduce the size of differentiation matrices (see section 3.2), a minimum of three nodes per sub-domain (anode, separator or cathode) is required to run the algorithm. However, reducing the number of nodes in the anode and cathode to $N_a = 3$ and $N_c = 3$ respectively yielded significant lithium conservation issues in practice. The number of nodes $N_a = 6$, $N_s = 3$ and $N_c = 6$ used in the present work were chosen to obtain accurate results up to $10\,C$ with a relatively small number of nodes. It was found that no significant improvement on the accuracy of results was gained by further increasing these numbers of nodes.

These results confirm the accuracy of this approach. Unlike simpler models that have previously been used for battery state estimation, such as the SP model, the P2D model is able to predict local variations of internal states across the cell. Such variations become particularly acute for high C-rate operation (figure 3.6), such as discharge where a large amount of lithium is released into the electrolyte at the anode and absorbed at the cathode into the active material. Due to the relatively slow diffusion of lithium ions from the anode to the cathode, a large concentration gradient builds up in the electrolyte across the cell and reduces the cell performance. It can be seen from Figure 3.6a that during a $10\,C$ discharge, the electrolyte is almost depleted of lithium in less than 50 s. It is also worth noting that an unphysical loss of lithium occurred in the electrolyte. This loss of lithium ions remained lower than 5 % during full constant-current discharges with values of current up to $10C$. This conservation issue might be due to the fact that the model implementation employs the reformulated electrolyte diffusion equation (3.37) rather than the conservative formulation (2.6).

The SP model also assumes that the insertion reaction rate is uniform within each electrode. Figure 3.6b shows that this assumption is not valid at high C-rates. At short timescales, the reaction rate at the electrode-separator interface can

be an order of magnitude higher compared to the reaction rate at the current collector. The use of the P2D model for battery state estimation could provide valuable information on local internal states to the BMS and could be combined to degradation models, an example of which is given in Appendix A, to enable better health-conscious battery management algorithms [15].

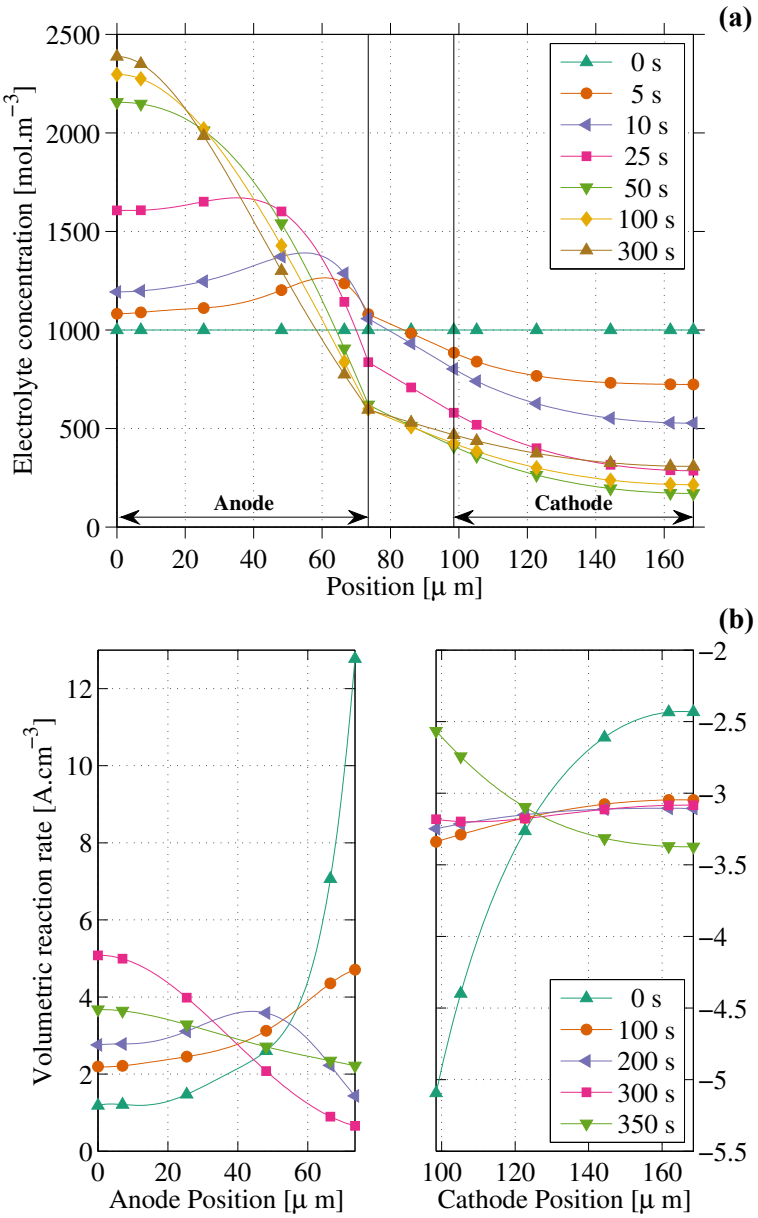

Fig. 3.6 Electrolyte concentration (a) and local volumetric reaction rate (b) profiles computed by the thermal-P2D model at several time steps estimated under a $10C$ constant-current discharge [2].

3.4.4 Dynamic current input

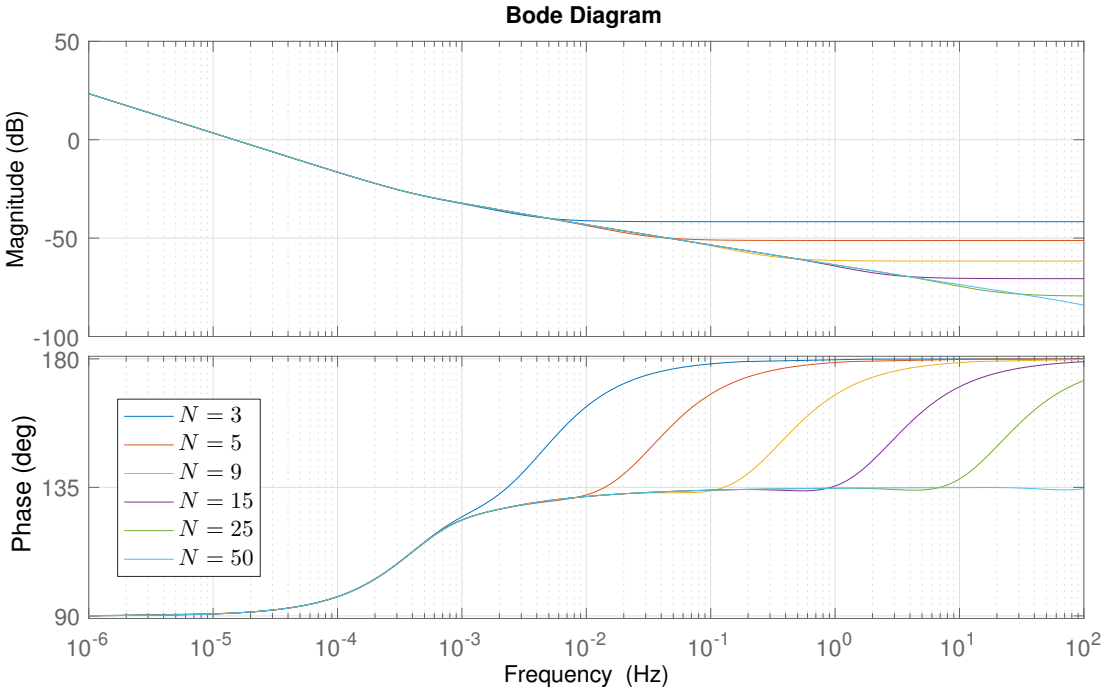

Fig. 3.7 Bode plot of the frequency response of the anode solid-phase particle model with increasing number of Chebyshev collocation nodes.

In embedded application for automotive BMSs, the state estimation would have to be performed with the dynamic current input experienced by the battery pack. The Combined ARTEMIS Driving Cycle (CADC) [152] was used to generate a dynamic current excitation profile approximately representative of an electric car (or PHEV with all-electric mode) drive cycle. It has been assumed that the cell input current was proportional to the vehicle's acceleration and that 25 % of the braking acceleration was recovered to charge the battery. We chose the scaling factor between car acceleration and input current in order to obtain a relatively aggressive load profile with peak current reaching $15\,C$, as shown on the top graph of Figure 3.8. This electric vehicle model is highly simplified to obtain an approximate but simple relation between the speed profile of the vehicle and the current applied to the battery pack. This simplistic model only considers inertia but in practice other forces applied to the vehicle, such as drag or rolling resistance, may have a significant impact on the battery current; for instance the

drag may substantially increase the power demand on the battery pack at high speed. In addition, the model should in principle relate the speed of the vehicle to the power requirement on the battery pack rather than the applied current; however, using power instead of current as input for the battery electrochemical model adds complexity because an algebraic equation is required to solve for battery current and voltage simultaneously. Since this work focuses on battery modelling rather than electric vehicle modelling, this simplistic model is sufficient as a first approximation to obtain a representative profile of applied current for an automotive battery.

For dynamic input currents such as the CADC, the input signal frequency affects the number of nodes required to discretise the model because high frequencies can yield very sharp concentration gradients at the surface of the solid-phase particles. For the set of parameters reported in Table 3.1, the limiting transport phenomenon is the diffusion of lithium in the anode active material due to its large characteristic time (low diffusivity). Figure 3.7 shows the Bode plot of the numerically simulated frequency response of the anode solid-phase diffusion state-space model (3.36) with increasing numbers of collocation nodes. The first phase shift from 90° to 135° occurring between 10^{-4} Hz and 10^{-3} Hz for all numbers of collocation nodes correspond to the physically meaningful diffusion characteristic time of the model. However, the second phase shift between 135° and 180° is unphysical and happens when the surface concentration gradient becomes too sharp compared to the order of the interpolating polynomial underlying orthogonal collocation. As shown on Figure 3.7, the appearance of this phenomenon is pushed towards high frequencies as the number of nodes increases, or equivalently higher-order interpolating polynomials. Because the sampling frequency of the CADC input profile is 1 Hz, the maximum frequency of interest in the signal should not be higher than approximately 0.1 Hz; therefore $N_p = 15$ collocation nodes should be sufficient for discretising the solid-phase diffusion model in both

electrodes in order to avoid this phenomenon. However, the sampling frequency of 1 Hz is a limitation of the input drive cycle (CADC) and is probably too low for automotive applications. The highest frequency of interest during real EV operation may be closer to 10 Hz than 0.1 Hz and more collocation nodes might therefore be required to discretise the solid-phase diffusion equation.

The model prediction of voltage and temperature for the CADC input current are shown in Figure 3.8. The model predicts that the full discharge of the battery occurs in 1700 s and that the temperature would rise up to 72 °C under these relatively aggressive conditions. The temperature elevation predicted by the model is relatively high compared to what would be experienced by cells in an automotive battery pack due to the high peaks of current and the simplistic air cooling system considered in this study. However, this simulation demonstrates that the model can be solved under highly dynamic and high C-rate operation. It is also worth recalling that the assumption of bulk thermal model probably does not accurately describe the thermal behaviour of the cell due to the temperature gradients building up in the radial directions under these conditions as explained in Section 2.3.2.

As illustrated by Figure 3.9, the main contribution to the global heat generation rate arises from the contact resistance heat generation q_{ctc} followed by the ohmic heat generation q_{ohm}, the reaction heat generation q_{rxn} and the reversible heat generation q_{rev}. Reversible heat is often neglected in the literature for high current operation due to its relatively low magnitude in comparison to other heat sources. However, it can be observed that the reversible heat cumulated over the driving cycle is not negligible.

The numerical solution of the model for a dynamic input with high amplitude current peaks is more intensive than a constant current discharge, and the computation time required by the solver is higher compared to constant-current simulations. The solution of 1700 s of simulation under the CADC considered

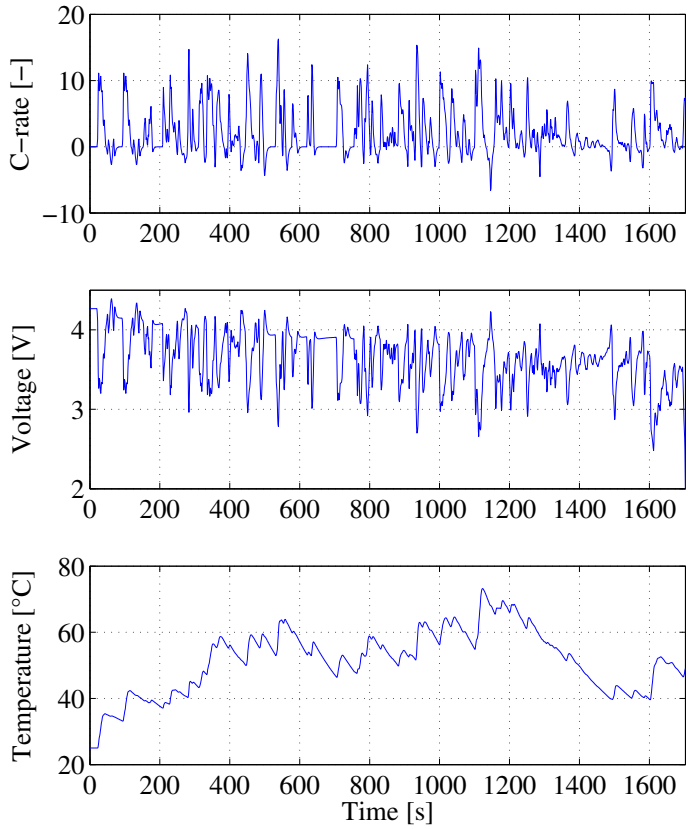

Fig. 3.8 Input current (C-rate), voltage and temperature predicted by the thermal-P2D model under a Combined ARTEMIS Driving Cycle [2].

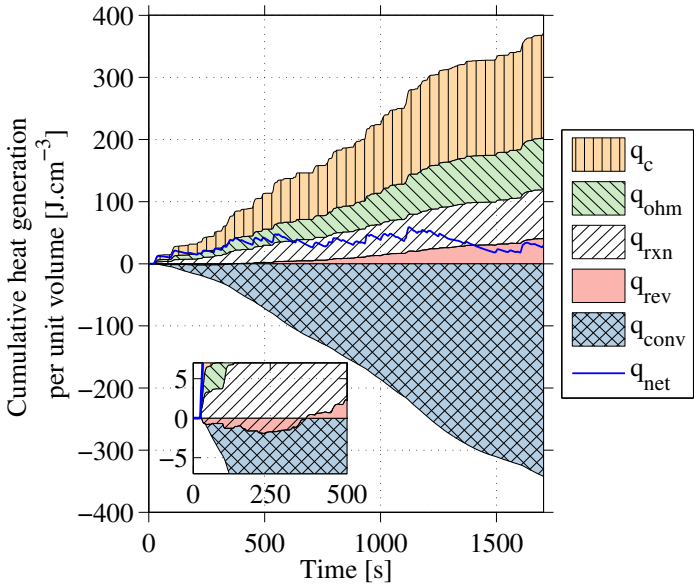

Fig. 3.9 Cumulative heat generated and convective heat removed per cell unit volume under the CADC [2].

required 285 s of computation on the desktop computer previously mentioned. However, this is still a relatively low computation time since only 168 ms were required on average to solve 1 s of simulation. This is a promising result for future work on the real-time solution of the thermal-electrochemical model for battery state estimation.

3.5 Concluding remarks

The thermal-electrochemical P2D model for lithium-ion batteries can be solved efficiently and accurately using Chebyshev orthogonal collocation and the built-in MATLAB® ODE/DAE solver *ode15s* for systems of semi-explicit differential-algebraic equations. The use of Chebyshev orthogonal collocation yields a highly reduced number of discretisation nodes compared to implementations employing the finite-difference method and the carefully considered model implementation results in a minimised number of algebraic constraints to solve. Most important, unlike most model-order reduction techniques found in the literature, the present approach does not impede the model prediction accuracy, while maintaining the physical significance of model parameters. Comparative simulations against a much higher-order finite-element model solved in COMSOL Multiphysics® confirm that the prediction accuracy is preserved even at high C-rates. Because of the relatively low number of states required in this approach, the P2D model can be combined to a state observer for the inference of battery internal states from external measurement. The implementation and performance of such a state estimation algorithm using an extended Kalman filter is discussed in the subsequent Chapter 4.

Chapter 4

State estimation using a modified extended Kalman filter

This chapter discusses the implementation of a Kalman filter for the state estimation of the P2D model discretised using orthogonal collocation presented in Chapter 2 and Chapter 3. The algorithm recovers the unmeasurable internal states of the model (3.82) and (3.83) from noisy measurements of voltage, current and temperature. The Kalman filter is a recursive algorithm that infers the battery internal states by correcting the model states in order to minimise the error between the predicted and actual measured voltage and temperature for a given current input.

Section 4.1 gives a very brief overview of the Kalman filter for linear models. A detailed explanation of the modifications required for its application to the thermal-electrochemical P2D model is then provided in Section 4.2. These modifications are motivated by the fact that the P2D model (i) is non-linear and (ii) contains algebraic constraints that cannot be handled by standard Kalman filter algorithms. More specifically, the extended Kalman filter algorithm for DAEs discussed in [153] is applied to the thermal-electrochemical P2D model. The derivation of the Kalman filter equations is not provided in this dissertation and the reader is referred to

the extensive literature on Kalman filtering such as [154–156]. The performance of the state estimation algorithms are examined in Section 4.3 against emulated experimental data using a high-order P2D model.

4.1 Kalman filtering

The Kalman filter is a computationally efficient recursive algorithm for estimating the state of dynamic systems described by a stochastic linear state-space model written in its discrete form

$$\mathbf{x}_{k+1} = \mathrm{A}\mathbf{x}_k + \mathrm{B}u_k + \mathbf{w}_k \tag{4.1}$$

$$\mathbf{y}_k = \mathrm{C}\mathbf{x}_k + \mathbf{v}_k, \tag{4.2}$$

where (4.1) is the discrete state equation governing the system dynamics with A and B the state and input matrices respectively, and (4.2) is the discrete measurement equation relating the states of the system $\mathbf{x}_k$ to the available measurements $\mathbf{y}_k$ with C the output matrix. The model input u_k is usually assumed deterministic, while the states and measurements are affected by additive uncorrelated zero-mean Gaussian process noise $\mathbf{w}_k$ and measurement noise $\mathbf{v}_k$ with covariance matrices Q and R respectively, to account for random environment disturbances and sensor noise.

At every time step $t_k = kT_s$, with sampling period T_s, an estimate of the state vector $\hat{\mathbf{x}}_k$ and the associated error covariance matrix $\hat{\mathrm{P}}_k$ are computed in two steps: the *time update* and the *measurement update*. In the time update, *a priori* estimates of the state $\hat{\mathbf{x}}^-_{k+1}$ and error covariance $\hat{\mathrm{P}}^-_{k+1}$ at t_{k+1} are calculated using

the model and the known input u_k according to (4.3) and (4.4).

$$\hat{\mathbf{x}}_{k+1}^{-} = \mathrm{A}\hat{\mathbf{x}}_k + \mathrm{B}u_k \tag{4.3}$$

$$\hat{\mathrm{P}}_{k+1}^{-} = \mathrm{A}\hat{\mathrm{P}}_k + \hat{\mathrm{P}}_k\mathrm{A}^{\mathrm{T}} + \mathrm{Q} \tag{4.4}$$

In the measurement update, *a posteriori* estimates of the state $\hat{\mathbf{x}}_{k+1}$ and error covariance $\hat{\mathrm{P}}_{k+1}$ are computed based on the error between estimated measurements $\hat{\mathbf{y}}_{k+1}^{-}$ and actual noisy measurements $\mathbf{y}_{k+1}$ according to (4.5), (4.6) and (4.7).

$$\mathrm{K}_{k+1} = \hat{\mathrm{P}}_{k+1}^{-}\mathrm{C}^{\mathrm{T}}\left(\mathrm{C}\hat{\mathrm{P}}_{k+1}^{-}\mathrm{C}^{\mathrm{T}} + \mathrm{R}\right)^{-1} \tag{4.5}$$

$$\hat{\mathbf{x}}_{k+1} = \hat{\mathbf{x}}_{k+1}^{-} + \mathrm{K}_{k+1}\left(\mathbf{y}_{k+1} - \hat{\mathbf{y}}_{k+1}^{-}\right) \tag{4.6}$$

$$\hat{\mathrm{P}}_{k+1} = \left(\mathrm{I} - \mathrm{K}_{k+1}\mathrm{C}\right)\hat{\mathrm{P}}_{k+1}^{-} \tag{4.7}$$

When considering physics-based models derived from first principles, such as the electrochemical P2D battery model, the state equation naturally arises in its continuous form (4.8) rather than its discrete form (4.1).

$$\dot{\mathbf{x}}(t) = \mathrm{A}\mathbf{x}(t) + \mathrm{B}u(t) + \mathbf{w}(t) \tag{4.8}$$

In this case, the *time update* equations of the original Kalman filter (4.3–4.4) must account for the time discretisation of the state equation and therefore become

$$\hat{\mathbf{x}}_{k+1}^{-} = \boldsymbol{\Phi}\hat{\mathbf{x}}_k + \int_{t_k}^{t_{k+1}} \boldsymbol{\Phi}\mathrm{B}u\left(\tau\right)d\tau \tag{4.9}$$

$$\hat{\mathbf{P}}_{k+1}^{-} = \boldsymbol{\Phi}\hat{\mathrm{P}}_k + \hat{\mathrm{P}}_k\boldsymbol{\Phi}^{\mathrm{T}} + \mathrm{Q}, \tag{4.10}$$

where $\boldsymbol{\Phi} = \exp\left(\mathrm{A}.T_s\right)$ is the state-transition matrix. The *measurement update* equations (4.5), (4.6) and (4.7) remain unchanged.

The Kalman filter is the optimal state estimator in the least-squares sense for minimising the state estimation error for linear systems subject to additive

Gaussian process and measurement noises. For systems described by non-linear differential equations however, the sub-optimal extended Kalman filter (EKF) is often used in the literature and basically consists of linearising the non-linear model at every time step, enabling the use of equations (4.3) through (4.7) of the standard Kalman filter [154–156]. A modified version of the extended Kalman filter suitable for semi-explicit DAEs is described in the subsequent section for the state estimation of the battery P2D model. In this modified EKF algorithm for DAEs, the linearised model is only employed for the time update of the error covariance matrix (4.4), the calculation of the Kalman gain (4.5), and the measurement update of the error covariance matrix (4.7). Specifically, the time update of the state vector (4.3) is performed by integrating the nonlinear DAE model using the *ode15s* MATLAB® solver. More advanced and accurate approaches such as higher-order EKFs or the unscented Kalman filter (UKF) are available for the state estimation of non-linear models [157]; however, the relative computational simplicity of the EKF in comparison to such advanced techniques makes it a good initial choice for the state estimation of the P2D model. Specifically, sigma-point estimators such as the UKF are not computationally tractable for the real-time estimation of large DAE models such as the P2D model because at every time step algebraic constraints must be solved for each of the $2n_x + 1$ sigma-points with n_x the number of differential states in the order of 100 for the P2D model [3].

4.2 P2D model state estimation algorithm

4.2.1 Battery stochastic state-space model

The EKF algorithm relies on a non-linear stochastic state-space model. Such a state-space representation of the P2D model can be derived from the state-space representation given by (3.80), (3.81) and (3.84) by adding process noise and measurement noise to the dynamics and measurement equations respectively

according to:

$$\dot{\mathbf{x}}(t) = \mathbf{f}\left(\mathbf{x}(t), \mathbf{z}(t), u(t)\right) + \mathbf{w}(t) \tag{4.11}$$

$$\mathbf{0} = \mathbf{g}\left(\mathbf{x}(t), \mathbf{z}(t), u(t)\right) \tag{4.12}$$

$$\mathbf{y}_k = \begin{bmatrix} \mathrm{H}_x & \mathrm{H}_z \end{bmatrix} \begin{bmatrix} \mathbf{x}_k \\ \mathbf{z}_k \end{bmatrix} + \mathrm{H}_u u_k + \mathbf{v}_k \tag{4.13}$$

Similarly to the Kalman filter discussed in Section 4.1, the process noise $\mathbf{w}$ and measurement noise $\mathbf{v}_k$ are zero-mean Gaussian additive noises uncorrelated in time with covariance matrices Q and R respectively. We assumed no noise on the input current $u(t)$.

4.2.2 DAE state-space model linearisation

The difference between the Kalman filter and the EKF consists of additional linearisation steps required between the time update and the measurement update compared to the Kalman filter algorithm for linear models. The linearisation of the differential equation (4.11) and the algebraic equation (4.12) are performed about the current state estimate $[\hat{\mathbf{x}}, \hat{\mathbf{z}}]^{\mathrm{T}}$ at every time step [153]. This allows the system of non-linear DAEs to be transformed into a system of locally linear ODEs that can be used in both the time update and measurement update steps discussed in Section 4.1. The stochastic variables $\mathbf{w}$ and $\mathbf{v}_k$ are additive and can therefore be ignored in the linearisation process.

To perform the model linearisation, we first define the following variables:

$$\tilde{\mathbf{x}} = \mathbf{x} - \hat{\mathbf{x}} \tag{4.14}$$

$$\dot{\tilde{\mathbf{x}}} = \dot{\mathbf{x}} - \dot{\hat{\mathbf{x}}} \tag{4.15}$$

$$\tilde{\mathbf{z}} = \mathbf{z} - \hat{\mathbf{z}} \tag{4.16}$$

$$\tilde{u} = u - \hat{u} \tag{4.17}$$

$$\tilde{\mathbf{y}} = \mathbf{y} - \hat{\mathbf{y}} \tag{4.18}$$

Assuming that the functions $\mathbf{f}$ and $\mathbf{g}$ are sufficiently differentiable, first-order Taylor series expansions of these functions about the current state estimate are:

$$\mathbf{f}\left(\mathbf{x}, \mathbf{z}\right) = \mathbf{f}\left(\hat{\mathbf{x}}, \hat{\mathbf{z}}\right) + \mathbf{f}_x\tilde{\mathbf{x}} + \mathbf{f}_z\tilde{\mathbf{z}} + \mathbf{f}_u\tilde{u} \tag{4.19}$$

$$\mathbf{g}\left(\mathbf{x}, \mathbf{z}\right) = \mathbf{g}\left(\hat{\mathbf{x}}, \hat{\mathbf{z}}\right) + \mathbf{g}_x\tilde{\mathbf{x}} + \mathbf{g}_z\tilde{\mathbf{z}} + \mathbf{g}_u\tilde{u} \tag{4.20}$$

where $\mathbf{f}_i$ and $\mathbf{g}_i$ denote the partial derivative of $\mathbf{f}$ and $\mathbf{g}$ respectively with respect to the variable $i = \{\mathbf{x}, \mathbf{z}, u\}$ evaluated at the current state estimate $[\hat{\mathbf{x}}, \hat{\mathbf{z}}]^{\mathrm{T}}$. The matrices $\mathbf{f}_x$, $\mathbf{f}_z$, $\mathbf{g}_x$ and $\mathbf{g}_z$ are therefore Jacobian matrices of the functions $\mathbf{f}$ and $\mathbf{g}$. A linear approximation of the DAE system is obtained by substituting (4.19) and (4.20) into (4.11) and (4.12):

$$\dot{\tilde{\mathbf{x}}} = \mathbf{f}_x\tilde{\mathbf{x}} + \mathbf{f}_z\tilde{\mathbf{z}} + \mathbf{f}_u\tilde{u} \tag{4.21}$$

$$\mathbf{0} = \mathbf{g}_x\tilde{\mathbf{x}} + \mathbf{g}_z\tilde{\mathbf{z}} + \mathbf{g}_u\tilde{u} \tag{4.22}$$

By assuming that the Jacobian matrix $\mathbf{g}_z$ is non-singular, which is equivalent to assuming that the semi-explicit DAEs system is of index 1 [141], the linearised algebraic constraint (4.20) can be rearranged to obtain an expression of the

algebraic state vector in terms of the differential state vector:

$$\tilde{\mathbf{z}} = -\mathbf{g}_z^{-1}\left[\mathbf{g}_x\tilde{\mathbf{x}} + \mathbf{g}_u\tilde{u}\right] \tag{4.23}$$

Substituting (4.23) into (4.21) gives the following linearised state equation that includes the algebraic constraint,

$$\dot{\tilde{\mathbf{x}}} = \mathrm{A}^{\mathrm{lin}}\tilde{\mathbf{x}} + \mathrm{B}^{\mathrm{lin}}\tilde{u} \tag{4.24}$$

where:

$$\mathrm{A}^{\mathrm{lin}} = \mathbf{f}_x - \mathbf{f}_z\mathbf{g}_z^{-1}\mathbf{g}_x \tag{4.25}$$

$$\mathrm{B}^{\mathrm{lin}} = \mathbf{f}_u - \mathbf{f}_z\mathbf{g}_z^{-1}\mathbf{g}_u \tag{4.26}$$

In the linearisation process, the DAE system is therefore transformed into an ODE system that can be used in a standard Kalman filter algorithm. The state-transition matrix $\mathbf{\Phi}$ of the linearised model is given by $\mathbf{\Phi} = \exp\left(\mathrm{A}^{\mathrm{lin}}T_s\right)$ and is used in the time update of the Kalman filter discussed in Section 4.1. In a similar way, substituting (4.23) into the measurement equation (4.13) gives,

$$\tilde{\mathbf{y}} = \mathrm{C}^{\mathrm{lin}}\tilde{\mathbf{x}} + \mathrm{D}^{\mathrm{lin}}\tilde{u} \tag{4.27}$$

where:

$$\mathrm{C}^{\mathrm{lin}} = \mathrm{H}_x - \mathrm{H}_z\mathbf{g}_z^{-1}\mathbf{g}_x \tag{4.28}$$

$$\mathrm{D}^{\mathrm{lin}} = \mathrm{H}_u - \mathrm{H}_z\mathbf{g}_z^{-1}\mathbf{g}_u \tag{4.29}$$

The measurement matrix $\mathrm{C}^{\mathrm{lin}}$ therefore includes the linearised algebraic constraint and can be used in the measurement update of the standard Kalman filter algorithm to compute the Kalman gain and update the error covariance estimate.

4.2.3 Summary of modified EKF for non-linear DAEs

This section provides a step-by-step description of the modified EKF for systems of DAEs. In [153], the modified EKF algorithm is based on the square-root form of the EKF for numerical stability. This guarantees that the error covariance matrix remains positive semi-definite by using the square-root of the error covariance matrix instead of the error covariance matrix itself. Although the square-root implementation is more robust in some cases, the two algorithms are mathematically equivalent and we found no difference in the results between the standard and square-root form for our problem. Only the standard version of the modified EKF is discussed for simplicity and the reader is referred to [153] regarding the implementation of the square-root EKF.

The EKF algorithm is initialised by assuming an initial differential state estimate $\mathbf{x}_0$ and error covariance matrix P_0 at time t_0. A consistent initial algebraic state vector $\mathbf{z}_0$ is computed using the MATLAB® solver *fsolve* for systems of non-linear equations. The computation of an initial error covariance matrix P_0 that accounts for the spatial correlation of the model states is crucial for the performance and convergence of the EKF for DAEs. The structure of the matrix P_0 must satisfy the spatial correlation of the error, otherwise the state estimate computed during the measurement update step may not satisfy the model PDEs and cannot guarantee conservation of lithium. The use of a diagonal initial error covariance matrix P_0 (*i.e.* no spatial correlation) results in the DAE solver failure after a few time steps. For instance, the values of concentration at two adjacent collocation nodes are clearly correlated through the diffusion equation. The concentration at any node should not be increased while the concentration values at adjacent nodes are decreased during the measurement update because this would yield a non-smooth concentration profile that does not satisfy the model PDEs. The structure of the error covariance matrix should reflect this correlation by only allowing the overall concentration profile to be corrected. In

this work, the structure of the error covariance matrix for the P2D model was obtained numerically. The model was integrated under various inputs and initial conditions to obtain a large set of possible states. These states were then used to numerically compute an error covariance matrix with the appropriate correlation structure.[1] An interesting future avenue of research would be to investigate how the structure of the error covariance matrix for the P2D model could be obtained in a more principled way.

Once the modified EKF for DAEs is initialised, the following algorithm steps are performed recursively:

1. *State time update:* The current state estimate $[\hat{\mathbf{x}}_k, \hat{\mathbf{z}}_k]^{\mathrm{T}}$ is projected forward in time to the next time step by integrating the non-linear DAEs system using the MATLAB® solver for DAEs *ode15s* from t_k to t_{k+1}. The predicted state vector at time t_{k+1} is the *a priori* state estimate $[\hat{\mathbf{x}}^-_{k+1}, \hat{\mathbf{z}}^-_{k+1}]^{\mathrm{T}}$ at time t_{k+1}.

2. *Model linearisation:* The DAE model is linearised about the current state estimate $[\hat{\mathbf{x}}_k, \hat{\mathbf{z}}_k]$ to compute the state transition matrix $\mathbf{\Phi} = \exp(\mathrm{A}^{\mathrm{lin}}.T_s)$ of the linearised model.

3. *Error covariance time update:* The error covariance $\hat{\mathrm{P}}_k$ is propagated in time using (4.10) to obtain the *a priori* error covariance estimate $\hat{\mathrm{P}}^-_{k+1}$ at time t_{k+1}.

4. *Model linearisation:* The DAE model is linearised about the *a priori* state estimate $[\hat{\mathbf{x}}^-_{k+1}, \hat{\mathbf{z}}^-_{k+1}]^{\mathrm{T}}$ in order to compute the measurement matrix $\mathrm{C}^{\mathrm{lin}}$ for the measurement update.

5. *Measurement update:* The matrix $\mathrm{C}^{\mathrm{lin}}$ previously computed is used to calculate the Kalman gain according to (4.5). The *a priori* differential state

[1] The mean of this large set of states was employed as reference to compute the error vectors used to generate the error covariance matrix.

estimate $\hat{\mathbf{x}}_{k+1}^{-}$ and error covariance estimate $\hat{\mathrm{P}}_{k+1}^{-}$ are updated to account for the measurement $\mathbf{y}_{k+1}$ according to (4.6) and (4.7) respectively. The measurement estimate $\hat{\mathbf{y}}_{k+1}$ in (4.6) is computed from the prior estimate $[\hat{\mathbf{x}}_{k+1}^{-}, \hat{\mathbf{z}}_{k+1}^{-}]^{\mathrm{T}}$ and the input u_{k+1} according to the measurement equation (3.84). The *a posteriori* differential state estimate $\hat{\mathbf{x}}_{k+1}$ and error covariance estimate $\hat{\mathrm{P}}_{k+1}$ are therefore obtained.

6. *Consistent algebraic states* The consistent *a posteriori* algebraic state estimate $\hat{\mathbf{z}}_{k+1}$ is obtained from the posterior differential state estimate $\hat{\mathbf{x}}_{k+1}$ and the input u_{k+1} using the MATLAB® *fsolve* function.

This algorithm is repeated recursively at every time step.

The last step of the proposed modified EKF for DAEs (step 6) is critical to the robustness of the algorithm. During the measurement update (step 5), the *a posteriori* differential state estimate $\hat{\mathbf{x}}_{k+1}$, which is computed from the *a priori* differential state estimate $\hat{\mathbf{x}}_{k+1}^{-}$ in light of the measurement $\mathbf{y}_{k+1}$, becomes inconsistent with the *a priori* algebraic state estimate $\hat{\mathbf{z}}_{k+1}^{-}$. Step 6 simply uses the MATLAB® solver for non-linear equations *fsolve* to recover an algebraic state $\hat{\mathbf{z}}_{k+1}$ that is consistent with the *a posteriori* differential state estimate $\hat{\mathbf{x}}_{k+1}$. Step 6 is computationally intensive because the solver *fsolve* performs iterations to recover this consistent algebraic state. However, omitting step 6 in the algorithm and performing the state time update (step 1) directly after the measurement update (step 5) means that the DAE solver *ode15s* must integrate the model from inconsistent initial conditions. Although this is possible in theory, we found that step 6 was beneficial in practice to ensure a more robust and faster algorithm.

4.3 Results and discussion

This section presents simulation results showing the performance of the modified EKF algorithm discussed in Section 4.2.3 for the state estimation of the full

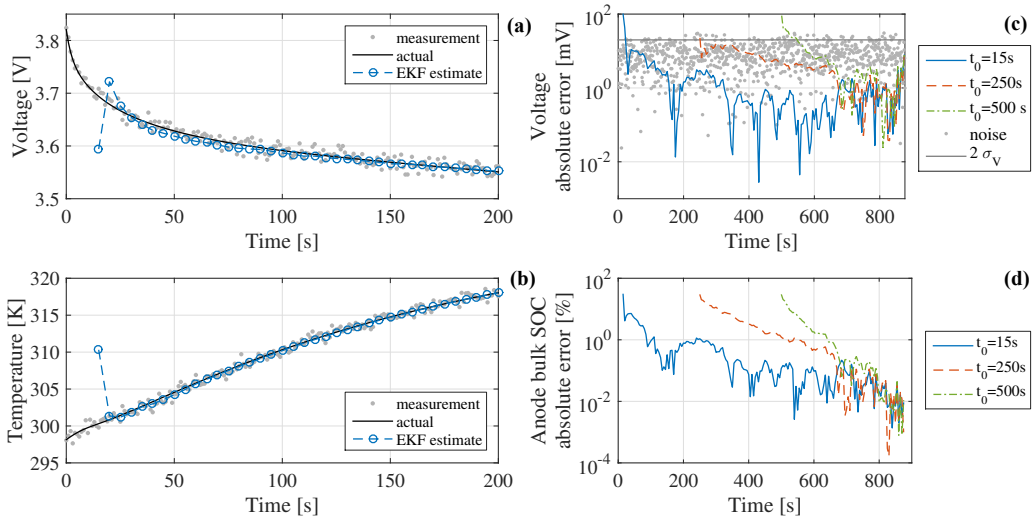

Fig. 4.1 Evolution of the voltage (a) and temperature (b) computed by the EKF compared to the actual and noisy measurements during the first 200 s of a $4C$ constant-current discharge. Evolution of the absolute error on voltage (c) and anode bulk SoC (d) estimated by the EKF compared to actual values generated by the reference simulation during the full $4C$ constant-current discharge [2].

thermal-electrochemical P2D model discussed in Chapter 2. The state estimation of a battery cell requires experimental data as inputs to the EKF, namely the applied current and the measured voltage and temperature response of the cell. Although the state estimator performance should ultimately be tested against real experimental data, due to the difficulty in verifying *in situ* the internal states in a real battery, we used the thermal-electrochemical model itself to emulate experimental results. Employing such numerical experiments is worthwhile since the state estimate error can be easily computed.

As a reference case, numerical experiments were computed by integrating the thermal-electrochemical model from 100 % SoC until the 2 V minimum cut-off voltage under constant-current discharge and the CADC discussed in Section 3.4.4. The EKF was then started from several initial conditions to check its convergence behaviour at different SoC ranging from 100 % to 50 %. For both the CADC and constant-current tests, the EKF initial guess on states assumed a cell at equilibrium (*i.e.* no concentration gradients) with an error on both the anode and

cathode SoC of 30 %[2], while the initial error on the temperature was set to 10 °C. The variances for the generation of the additive Gaussian white measurement noise were set to $\sigma_V^2 = 1 \times 10^{-4}\,\mathrm{V}^2$ and $\sigma_T^2 = 0.25\,\mathrm{K}^2$ for the voltage and temperature respectively. These variances correspond to a standard deviation $\sigma_V = 10\,\mathrm{mV}$ on the voltage and $\sigma_T = 0.5\,\mathrm{K}$ on the temperature. The measurement noise covariance matrix R of the EKF was defined using these values. No process noise was added to the state variables of the model and therefore the EKF process noise covariance matrix Q was set to zero.

4.3.1 Constant-current discharge

Figure 4.1 shows the voltage and temperature calculated by the EKF and the corresponding measurements for the first 200 s of a $4C$ constant-current discharge with a 5 s time step. The EKF voltage and temperature rapidly converge to the actual reference values in only a few time steps. The voltage absolute error for the full $4C$ discharge is shown on figure 4.1c. The EKF was started at three different initial times, 15 s, 250 s and 500 s, to check the convergence behaviour at different SoCs. The grey line represents the 95 % confidence interval on the voltage noisy measurement ($2\sigma_V$) and the grey dots are the absolute measurement error on voltage. The EKF shows similar convergence behaviour for all initial time t_0 studied and the voltage estimate falls below the 95 % confidence interval within the first few time steps. Similar results were observed for temperature measurements.

The EKF algorithm is designed to accurately fit the measurements, but this does not guarantee the convergence of the state estimates. Figure 4.1d shows the absolute error between the EKF estimated anode bulk SoC and the actual SoC for the full $4C$ constant-current discharge. Again, the EKF was started at

[2]Initialising the EKF algorithm with an error larger than 30 % on electrode SoC generally resulted in computation failure. This is probably due to the fact that the linear approximation of the modified EKF does not hold for the significant initial measurement update arising from this large initial error.

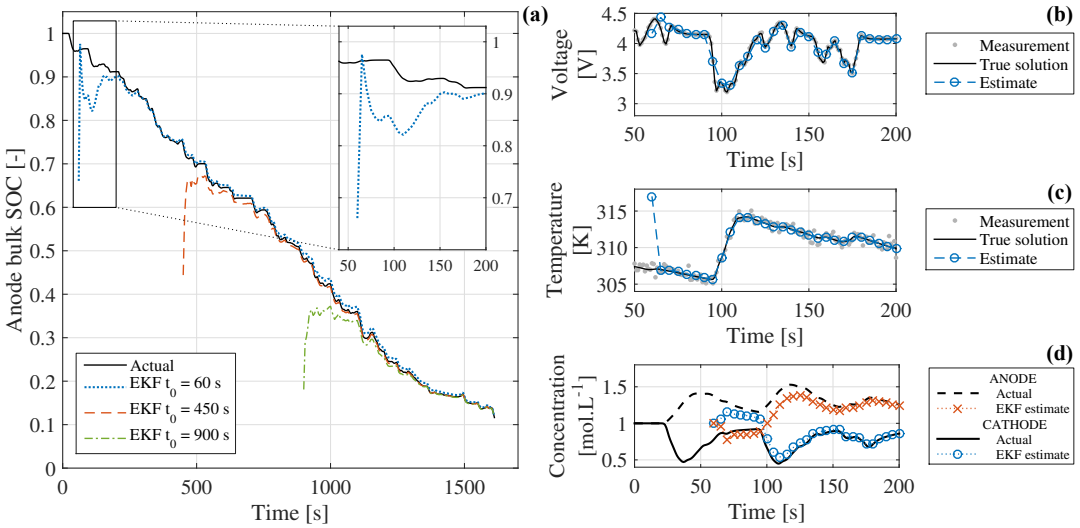

Fig. 4.2 Evolution of the anode bulk SoC estimated by the EKF compared to the actual value for CADC charge/discharge cycle (a). Evolution of the voltage (b), temperature (c) and electrolyte lithium concentration at the anode and cathode current collectors (d) computed by the EKF compared to the actual and noisy values generated by the reference simulation during the first 200 s of the CADC charge/discharge cycle [2].

different SoCs (initial times t_0) and shows a satisfactory convergence behaviour for all cases. From the 30 % initial absolute error, the anode bulk SoC estimate error falls below 1 % after less than 200 s of simulation (300 s when started at t_0 = 250 s). Similar results were observed for the cathode bulk SoC due to the conservation of lithium in the cell.

4.3.2 Dynamic current input

The EKF algorithm was then applied to the battery charge/discharge cycle under the CADC. This drive cycle is highly dynamic with large current peaks. However, the EKF was solved using a 5 s time-step to reduce the computation time. On average, the EKF under CADC was solved in 0.6 s of computation per second of simulation on the desktop computer previously mentioned. Figure 4.2b and 4.2c show the rapid convergence of both the EKF voltage and temperature compared to the measurements. Similarly to the constant-current scenario, the anode bulk

SoC also converges relatively quickly to the actual value. The absolute error on anode bulk SoC falls below 1 % by 150 s of simulation. However, this 1 % error on the final state estimate is likely to be larger when running the state estimation algorithm against real experimental battery data because of discrepancies between the actual battery behaviour and the one predicted by the model. An interesting future avenue of research, to investigate the effect of model inaccuracies on the state estimation performance, would be to test the state estimation algorithm against synthetic data generated from a battery model with altered parameters.

Another interesting state of the model is electrolyte concentration, since saturation or depletion of lithium in the electrolyte can lead to battery performance limitations at high current peaks. Figure 4.2d shows the evolution of the estimated and actual electrolyte concentration at the anode and cathode current collectors during the first few seconds of the driving cycle. This graphs shows that the algorithm is able to recover from the wrong initial conditions and track the electrolyte concentration during battery operation accurately.

4.3.3 Performance with reduced number of collocation nodes

Although the EKF can perform the state estimation of the full P2D model in real-time on a desktop computer, minimising the algorithm computational cost is beneficial for embedded applications and can be achieved by considering fewer collocation nodes. By reducing the number of nodes in the particles from $N_p = 15$ to $N_p = 8$ and $N_p = 6$, the number of model differential states n_x is reduced from 165 to 81 and 69 respectively. The number of algebraic variables remains unchanged. Figures 4.3 and 4.4 show the state estimation error on the anode bulk SoC and electrolyte concentration at the anode current collector respectively, with these reduced number of collocation nodes in the particles compared to the high-fidelity model $N_p = 15$. Although the estimation convergence is slower for

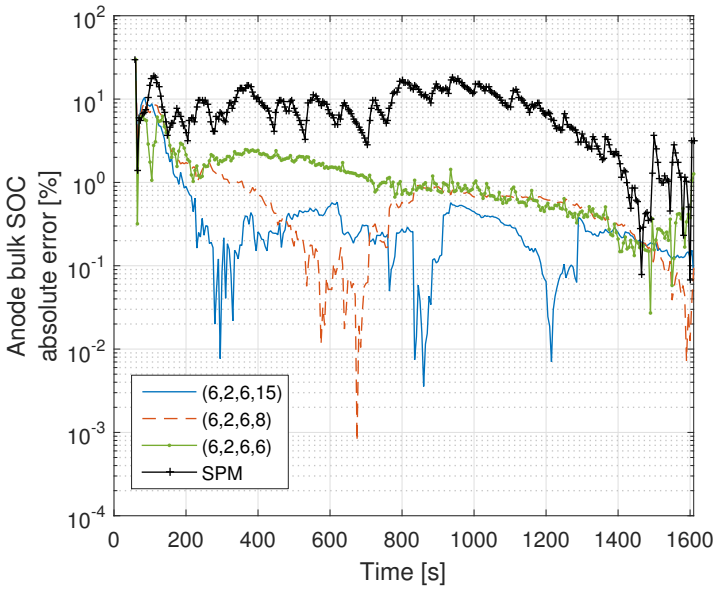

Fig. 4.3 Anode bulk SoC estimation error with reduced number of collocation nodes (N_a, N_s, N_c, N_p) and SP model-based EKF estimation [3].

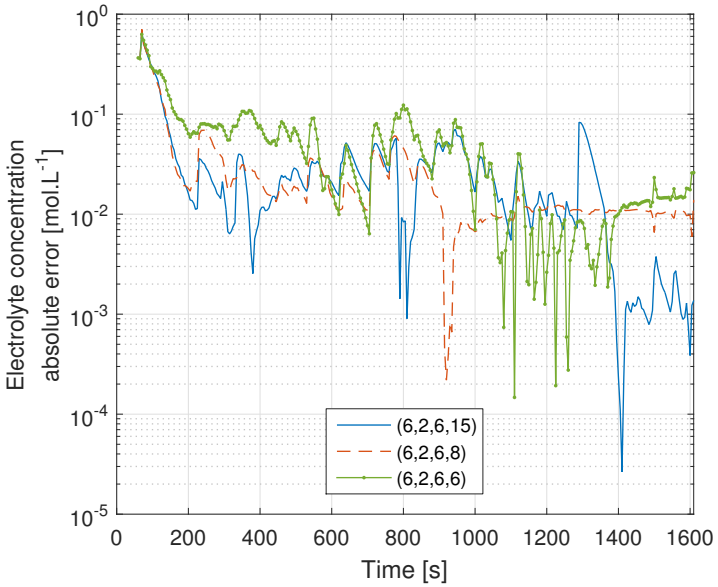

Fig. 4.4 Electrolyte concentration (at the anode current collector) estimation error with reduced number of collocation nodes (N_a, N_s, N_c, N_p) [3].

$N_p = 8$, the estimates of anode bulk SoC and electrolyte concentration remain accurate, while the computation time is reduced by a factor of three compared to the high-order model. Similarly, the computation time is reduced further for $N_p = 6$ at the expense of the estimation convergence and accuracy.

4.3.4 Comparison with SP model-based state estimation

Figures 4.3 shows the SoC estimation performance of the SP model-based EKF compared to the high-fidelity model. Similar to the P2D model discretisation, each particle of the SP model was discretised using $N_p = 15$ Chebyshev collocation nodes. Unlike the P2D model, the SP model does not feature algebraic constraints and is only composed of ODEs. The solution and state estimation of the SP model therefore requires far less computational effort and results in an EKF algorithm that is 40 times faster compared to the one using the P2D model with $N_p = 15$. However, the state estimation based on the SP model is far less accurate with a typical estimation error around 10 % compared to less than 1 % for that based on the P2D model. The poor estimation performance of the SP model-based EKF can be explained by peak values as high as $16\,C$ in the CADC current profile for which electrolyte dynamics neglected in the SP model become significant.

4.3.5 Effect of voltage measurement noise

In addition to uncertainties induced by the model, state estimation performance can be drastically impacted by the quality of measurements. In previous numerical experiments, both voltage and temperature noise levels were kept constant with standard deviations equal to $\sigma_V = 10\,\text{mV}$ and $\sigma_T = 0.5\,\text{K}$ respectively. Figure 4.5 shows the impact of increasing the voltage measurement standard deviation to $\sigma_V = 20\,\text{mV}$ and $\sigma_V = 50\,\text{mV}$ on the convergence of the P2D model state estimation with $N_a = 6$, $N_s = 3$, $N_a = 6$ and $N_p = 15$. The EKF measurement covariance matrix R was adjusted according to these noise levels. The bulk SoC estimation

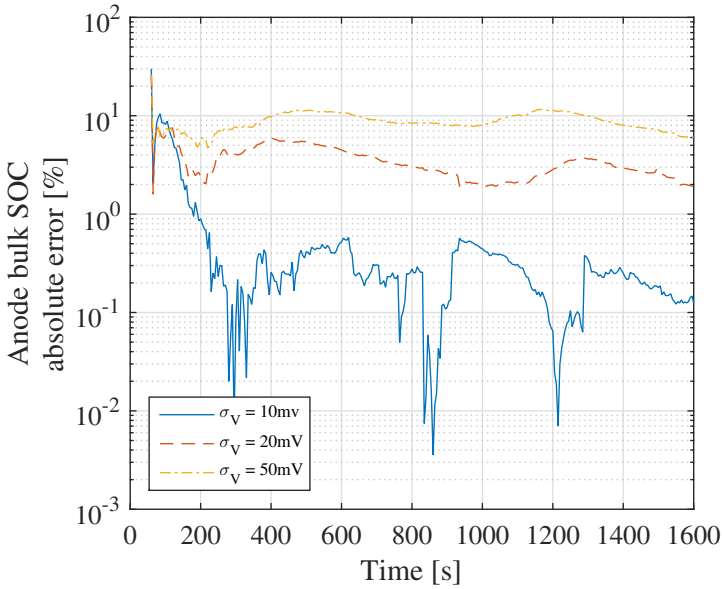

Fig. 4.5 Anode bulk SoC estimation error with increasing voltage measurement noise [3].

accuracy clearly deteriorates with increasing voltage measurement noise and less than 1 % estimation error cannot be reached under these higher noise levels.

4.4 Concluding remarks

An extended Kalman filter was developed to estimate the states of the P2D battery model due to its relatively low computational complexity compared to more advanced observers for non-linear models. This modified extended Kalman filter is able to estimate the model state and its error covariance by using a time-varying linear approximation of the model differential-algebraic equations about the state estimate at every time-step. Results indicate that the state estimation algorithm is able to quickly (less than 200 s) recover the model states even with a 30 % error on the initial SoC. Furthermore, the EKF estimation of SoC based on the P2D model is far more accurate than that based on the SP model under highly dynamic current inputs with high peak values. The use of such a P2D

model-based estimation algorithm could results in improved monitoring in fast charging and hybrid electric vehicles applications.

Chapter 5

Identifiability analysis and SP model parameter estimation

The estimation of accurate parameters from experimental data is key to enabling the use of electrochemical models for trustworthy battery diagnostics and prognosis. As discussed in Chapter 1, the relatively few authors who investigated this challenging problem in details have faced unidentifiability issues and found that the estimated parameters were highly uncertain, even though the predicted voltage fitted experimental data very well [32, 85]. Most approaches attempted the estimation of some intuitively chosen subset of parameters, or even all model parameters, using more or less advanced optimisation techniques (see Section 1.2.4). In this chapter, we take a 'step back' from the literature and take a close look at the model equations to understand in principle the unidentifiability challenges encountered in practice. This chapter first focuses on the structural identifiability of the electrochemical SP model. The practical parameter estimation is then investigated in light of the structural identifiability analysis. Results for the simpler SP electrochemical model introduced in Section 2.2 are presented in this thesis as a stepping stone towards the more involved analysis of the P2D model, which is beyond the scope of this thesis and left as future research work.

First, the SP model equations are reformulated and partially non-dimensionalised to reveal a maximum of six grouped parameters that can possibly be identified in principle. The transcendental transfer function of the SP model is then derived by linearising the voltage measurement equation about a fixed depth-of-discharge[1] (DoD) and used to study the local structural identifiability of the model. Particularly, this analysis emphasises the importance of the open-circuit potential slope with respect to DoD. Finally, the parameter estimation of the SP model from frequency-domain data (*i.e.* electrochemical impedance spectroscopy) is performed to investigate the practical identifiability of the model from emulated and actual experimental data.

Remark on notations in this chapter For better readability, the notation conventions adopted in this chapter are slightly different compared to Chapter 2 and 3. Since electrolyte dynamics are ignored in the SP model and only the solid-phase is considered, the subscript s is dropped from all variables. Additionally, the subscripts - and + are used instead of 1 and 3 to denote variables relating to the anode (negative electrode) and cathode (positive electrode) domains respectively. Numeral subscripts are used in this chapter to indicate vector elements.

5.1 SP model grouped parameters

First-principle models, such as the SP model, are usually over-parametrised in the sense that only a subset of parameters can be estimated from measured input-output data. A first necessary step towards credible parameter estimation is to reformulate the model in terms of the minimum number of parameter groups. In order to identify such groups of parameters, we first introduce the

[1]Note that in this chapter the depth-of-discharge (DoD) is used instead of SoC but these two values are simply related by DoD = 1 – SoC. Therefore, the DoD ranges from 0 % for a fully charged battery to 100 % for a fully discharged battery.

dimensionless radial coordinates[2] $\bar{r} = r_i/R_i$, and the stoichiometry $x_i = c_i/c_i^{max}$ instead of concentration in the initial-boundary value problem (2.3)–(2.4)–(2.5) governing diffusion in each electrode particle of the SP model. In addition, the change of variable $\bar{x}_i = x_i - x_i^0$ is introduced, with $x_i^0 = c_i^0/c_i^{max}$ being the initial stoichiometry in each particle i, in order to set the initial condition to zero in the governing equations. Note that the time independent variable t is kept dimensional because the diffusion time constants are different in each electrode. Introducing these dimensionless variables, the initial-boundary value problem (2.3)–(2.4)–(2.5) can be written equivalently

$$\frac{\partial \bar{x}_i}{\partial t} = \frac{D_i}{R_i^2}\frac{1}{\bar{r}^2}\frac{\partial}{\partial \bar{r}}\left(\bar{r}^2\frac{\partial \bar{x}_i}{\partial \bar{r}}\right), \tag{5.1}$$

subject to the boundary conditions

$$\left.\frac{\partial \bar{x}_i}{\partial \bar{r}}\right|_{\bar{r}=0} = 0 \quad \text{and} \quad \left.\frac{\partial \bar{x}_i}{\partial \bar{r}}\right|_{\bar{r}=1} = \frac{-R_i}{D_i c_i^{\max}} j_i, \tag{5.2}$$

with initial conditions

$$\bar{x}_i(0, \bar{r}) = 0. \tag{5.3}$$

Using (2.22) and (2.23) and recalling that the applied current density is given by $i_{\text{app}} = I/A$, the boundary condition at the surface of the particle in each electrode can also be written in terms of the input current I instead of the fluxes j_i according to

$$\left.\frac{\partial \bar{x}_+}{\partial \bar{r}}\right|_{\bar{r}=1} = +\frac{R_+^2}{D_+}\frac{I}{3\epsilon_+\delta_+ c_+^{\max}\mathcal{F}A} \tag{5.4}$$

$$\left.\frac{\partial \bar{x}_-}{\partial \bar{r}}\right|_{\bar{r}=1} = -\frac{R_-^2}{D_-}\frac{I}{3\epsilon_-\delta_- c_-^{\max}\mathcal{F}A}. \tag{5.5}$$

[2]Note that the same notation $\bar{r}$ for the radial coordinate transformation as the the one used in equation (3.19) of Section 3.2.2 is adopted here; however, the change of variable is different in this chapter and maps the radial coordinates from $[0\,,\,R_i]$ to $[0\,,\,1]$ rather than $[-1\,,\,1]$.

Similarly, using the inverted Butler-Volmer kinetics equation (2.25), the expression for the overpotential in each electrode is given by

$$\eta_+ = \frac{2RT}{\mathcal{F}} \sinh^{-1}\left(-\frac{R_+}{2k_+\sqrt{c_e}} \frac{1}{3\epsilon_+\delta_+ c_+^{\max}\mathcal{F}A} \frac{I}{\sqrt{x_+^{\text{surf}}(1-x_+^{\text{surf}})}} \right) \tag{5.6}$$

$$\eta_- = \frac{2RT}{\mathcal{F}} \sinh^{-1}\left(+\frac{R_-}{2k_-\sqrt{c_e}} \frac{1}{3\epsilon_-\delta_- c_-^{\max}\mathcal{F}A} \frac{I}{\sqrt{x_-^{\text{surf}}(1-x_-^{\text{surf}})}} \right), \tag{5.7}$$

with the the voltage measurement (2.24) expression unchanged. Six physically meaningful groups of parameters naturally arise in these equations. Indeed, one can identify three groups of parameters for each electrode: a diffusion time constant τ_i^{d}, kinetics time constant τ_i^{k} and the maximum theoretical electrode capacity Q_i^{th}. The expressions for these six physically meaningful groups of parameters are defined as follows

$$\tau_+^{\text{d}} = \frac{R_+^2}{D_+} \qquad \tau_-^{\text{d}} = \frac{R_-^2}{D_-} \tag{5.8}$$

$$\tau_+^{\text{k}} = \frac{R_+}{2k_+\sqrt{c_e}} \qquad \tau_-^{\text{k}} = \frac{R_-}{2k_-\sqrt{c_e}} \tag{5.9}$$

$$Q_+^{\text{th}} = -\epsilon_+\delta_+ c_+^{max}\mathcal{F}A \qquad Q_-^{\text{th}} = +\epsilon_-\delta_- c_-^{max}\mathcal{F}A \tag{5.10}$$

Note that for convenience the cathode theoretical capacity Q_+^{th} is defined negative to yield the same model structure in both the anode and cathode. Substituting these grouped parameters into the governing equations result in the following diffusion equation for both the cathode and anode

$$\frac{\partial \bar{x}_i}{\partial t} = \frac{1}{\tau_i^{\text{d}}} \frac{1}{\bar{r}^2} \frac{\partial}{\partial \bar{r}} \left(\bar{r}^2 \frac{\partial \bar{x}_i}{\partial \bar{r}} \right) \tag{5.11}$$

subject to the boundary conditions

$$\left.\frac{\partial \bar{x}_i}{\partial \bar{r}}\right|_{\bar{r}=0} = 0 \quad \text{and} \quad \left.\frac{\partial \bar{x}_i}{\partial \bar{r}}\right|_{\bar{r}=1} = -\frac{\tau_i^{\text{d}}}{3Q_i^{\text{th}}} I \tag{5.12}$$

with initial condition

$$\bar{x}_i(0, \bar{r}) = 0. \tag{5.13}$$

The voltage measurement equation remains

$$V = U_+\left(x_+^{\text{surf}}\right) - U_-\left(x_-^{\text{surf}}\right) + \eta_+ - \eta_-, \tag{5.14}$$

with the cathode and anode overpotentials given by

$$\eta_+ = \frac{2RT}{\mathcal{F}} \sinh^{-1}\left(\frac{\tau_+^{\text{k}}}{3Q_+^{\text{th}}} \frac{I}{\sqrt{x_+^{\text{surf}}(1 - x_+^{\text{surf}})}}\right) \tag{5.15}$$

$$\eta_- = \frac{2RT}{\mathcal{F}} \sinh^{-1}\left(\frac{\tau_-^{\text{k}}}{3Q_-^{\text{th}}} \frac{I}{\sqrt{x_-^{\text{surf}}(1 - x_-^{\text{surf}})}}\right). \tag{5.16}$$

Inspecting (5.11) through (5.16) one can identify six groups of parameters θ_i that fully parametrise the SP model given by the parameter vector $\boldsymbol{\theta} \in \mathbb{R}^6$:

$$\boldsymbol{\theta} = \begin{bmatrix} \tau_+^{\text{d}} & \dfrac{\tau_+^{\text{d}}}{3Q_+^{\text{th}}} & \dfrac{\tau_+^{\text{k}}}{3Q_+^{\text{th}}} & \tau_-^{\text{d}} & \dfrac{\tau_-^{\text{d}}}{3Q_-^{\text{th}}} & \dfrac{\tau_-^{\text{k}}}{3Q_-^{\text{th}}} \end{bmatrix}^{\text{T}}. \tag{5.17}$$

Unlike the parameters defined in (5.8)–(5.9)–(5.10), these parameters θ_i appear only once and not as a product of each other in the model equations. Moreover, one can show that there is a one-to-one mapping between the six parameter θ_i and the six parameters (5.8)–(5.9)–(5.10) defined by:

$$\begin{cases} \tau_+^{\text{d}} & = \theta_1 \\ \tau_+^{\text{k}} & = (\theta_1\theta_3)/\theta_2 \\ Q_+^{\text{th}} & = \theta_1/(3\theta_2) \\ \tau_-^{\text{d}} & = \theta_4 \\ \tau_-^{\text{k}} & = (\theta_4\theta_6)/\theta_5 \\ Q_-^{\text{th}} & = \theta_4/(3\theta_5) \end{cases} \tag{5.18}$$

Therefore, assuming that the initial electrode stoichiometries x_i^0 (i.e. state-of-charge) are known and that the open-circuit potentials are known functions of the surface stoichiometry for each electrode, the six parameters contained in $\boldsymbol{\theta}$, or equivalently the six parameters defined in (5.8–5.10), are sufficient to fully parametrise the single-particle model.

5.2 Structural identifiability

A set of six grouped parameters has been identified as sufficient to fully parametrise the SP model. However, this does not imply that these six parameters can be mathematically identified from the battery current-voltage response. Several approaches can be used to investigate the parameter identifiability of a dynamical model from input-output data. In this section, the so-called *structural identifiability* [158] of the SP model is discussed. Structural identifiability investigates the mathematical identifiability of the model irrespective of the identification data considered (which are also assumed noise-free). A definition of structural identifiability for linear time-invariant dynamic models that can be cast into a transfer function $H(s, \boldsymbol{\theta})$ parametrised by a vector of parameters $\boldsymbol{\theta}$ is given as follows [71, 159].

Definition 1 *Consider a model structure $\mathcal{M}$ with the transfer function $H(s, \boldsymbol{\theta})$ parametrised by $\boldsymbol{\theta} \in \mathcal{D} \subset \mathbb{R}^n$ where n denotes the number of parameters of the model. The identifiability equation for $\mathcal{M}$ is given by*

$$H(s, \boldsymbol{\theta}) = H(s, \boldsymbol{\theta}^*) \qquad \text{for almost all } s, \tag{5.19}$$

with $\boldsymbol{\theta}, \boldsymbol{\theta}^* \in \mathcal{D}$. The model structure $\mathcal{M}$ is said to be:

- globally identifiable *if* (5.19) *has a unique solution in $\mathcal{D}$,*
- locally identifiable *if* (5.19) *has a finite number of solutions in $\mathcal{D}$,*

- unidentifiable *if* (5.19) *has a infinite number of solutions in* $\mathcal{D}$.

The SP model is not a linear dynamical model because of its voltage measurement equation (5.14) incorporating nonlinear Butler-Volmer kinetics (5.15)–(5.16), and nonlinear OCP functions. Therefore Definition 1 cannot directly be used to investigate the SP model structural identifiability unless we first linearise the model by assuming a small perturbation around a fixed depth-of-discharge (DoD) point. Since we assume the nonlinear OCP functions are measured and known a priori (for example using the techniques described in [96, 94]), linearisation is a valid approach to obtain the parameters of the diffusion sub-models, each of which are linear, and to obtain a linearised approximation of the kinetics of the overall system. The subject of identifiability and parameter estimation of the nonlinear kinetics term in the output equation would be an interesting topic for further research.

5.2.1 Diffusion model transcendental transfer function

Definition 1 requires the model transfer function; we therefore first derive this for the spherical particle diffusion model and then combine it in subsequent sections with the transfer function of the linearised voltage measurement equation to derive the transfer function for the linearised SP model. Similarly to Section 3.2.2, in order to simplify the derivation of the diffusion model transfer function, the change of variable $\bar{u}_i = \bar{r}\bar{x}_i$ is introduced into the initial-boundary value problem (5.11)–(5.12)–(5.13) describing the diffusion in a spherical particle. Under this change of variable (5.11) can be equivalently written

$$\frac{\partial \bar{u}_i}{\partial t} = \frac{1}{\tau_i^{\mathrm{d}}} \frac{\partial^2 \bar{u}_i}{\partial r_i^2}, \tag{5.20}$$

and the boundary conditions (5.12) become

$$\bar{u}_i\left(r_i = 0\right) = 0 \quad \text{and} \quad \left.\frac{\partial \bar{u}_i}{\partial \bar{r}}\right|_{\bar{r}=1} - u(\bar{r} = 1) = \frac{-\tau_i^{\mathrm{d}}}{3C_i^{\mathrm{th}}} I. \tag{5.21}$$

As explained in Section 3.2.2, the homogeneous Neumann boundary condition at the centre of the particle is reduced to a simpler homogeneous Dirichlet boundary condition so that $\lim_{r_i \to 0} c_i(r_i)$ remains finite. The initial condition (5.13) becomes

$$\bar{u}_i(0, \bar{r}) = 0. \tag{5.22}$$

Since the initial-boundary value diffusion problem (5.20)–(5.21)–(5.22) is linear, an equivalent transfer function can be determined without loss of generality. Taking the Laplace transform of (5.20) yields

$$\frac{d^2 \bar{U}_i(s, \bar{r})}{d\bar{r}^2} - s\tau_i^{\mathrm{d}} \bar{U}_i(s, \bar{r}) = 0 \tag{5.23}$$

where s is the frequency-domain Laplace variable. The characteristic equation for this differential equation is

$$\lambda^2 - s\tau_i^{\mathrm{d}} = 0 \quad \Rightarrow \quad \lambda = \pm\sqrt{s\tau_i^{\mathrm{d}}}, \tag{5.24}$$

and its general solution is therefore

$$\bar{U}_i(s, \bar{r}) = A_i(s) e^{+\bar{r}\sqrt{s\tau_i^{\mathrm{d}}}} + B_i(s) e^{-\bar{r}\sqrt{s\tau_i^{\mathrm{d}}}} \tag{5.25}$$

with $A_i(s)$, $B_i(s)$ two functions that are independent of $\bar{r}$ to be determined using the boundary conditions (5.21). Substituting (5.25) into the particle centre boundary condition (5.21) at $\bar{r} = 0$ yields

$$B_i(s) = -A_i(s). \tag{5.26}$$

And substituting (5.25) and (5.26) into the surface boundary conditions (5.21) at $\bar{r} = 1$ yields

$$A_i(s) = \frac{\tau_i^{\mathrm{d}}}{3C_i^{\mathrm{th}}} \frac{I(s)/2}{\sinh\left(\sqrt{s\tau_i^{\mathrm{d}}}\right) - \sqrt{s\tau_i^{\mathrm{d}}}\cosh\left(\sqrt{s\tau_i^{\mathrm{d}}}\right)} \tag{5.27}$$

Substituting (5.27)–(5.26) into (5.25) yields the general solution for $\bar{U}_i(s, \bar{r})$

$$\bar{U}_i(s, \bar{r}) = \frac{\tau_i^{\mathrm{d}}}{3C_i^{\mathrm{th}}} \frac{\sinh\left(\bar{r}\sqrt{s\tau_i^{\mathrm{d}}}\right)}{\sinh\left(\sqrt{s\tau_i^{\mathrm{d}}}\right) - \sqrt{s\tau_i^{\mathrm{d}}}\cosh\left(\sqrt{s\tau_i^{\mathrm{d}}}\right)} I(s) \tag{5.28}$$

The variable of interest is the surface stoichiometry $\bar{X}_i^{\mathrm{surf}}(s)$, rather than $\bar{U}_i(s, \bar{r})$, since this is the variable involved in the voltage measurement equation. By substituting $\bar{u}_i = \bar{r}\bar{x}_i$ into (5.28), evaluating at $\bar{r} = 1$ and dividing by the input current $I(s)$, the transfer function $H_i^{\mathrm{d}}(s)$ for the spherical diffusion model is given by

$$H_i^{\mathrm{d}}(s) = \frac{\bar{X}_i^{\mathrm{surf}}(s)}{I(s)} = \frac{\tau_i^{\mathrm{d}}}{3C_i^{\mathrm{th}}} \frac{\tanh\left(\sqrt{s\tau_i^{\mathrm{d}}}\right)}{\tanh\left(\sqrt{s\tau_i^{\mathrm{d}}}\right) - \sqrt{s\tau_i^{\mathrm{d}}}}. \tag{5.29}$$

The cathode and anode diffusion transfer functions expressed in terms of the parameter vector $\boldsymbol{\theta}$ are therefore respectively

$$H_+^{\mathrm{d}}(s, \boldsymbol{\theta}) = \frac{\theta_2 \tanh\left(\sqrt{s\theta_1}\right)}{\tanh\left(\sqrt{s\theta_1}\right) - \sqrt{s\theta_1}}, \tag{5.30}$$

and

$$H_-^{\mathrm{d}}(s, \boldsymbol{\theta}) = \frac{\theta_5 \tanh\left(\sqrt{s\theta_4}\right)}{\tanh\left(\sqrt{s\theta_4}\right) - \sqrt{s\theta_4}}. \tag{5.31}$$

5.2.2 Linearisation of the voltage measurement equation

The voltage measurement equation is a nonlinear function of the input current I and of the anode and cathode surface stoichiometry x_-^{surf} and x_+^{surf} respectively. Assuming that the input current amplitude I remains small and that the battery is operated close to its initial DoD, *i.e.* the stoichiometry in both electrodes remains

close to the initial value x_i^0, the voltage equation can be linearised using a first-order Taylor series approximation about the reference point $\mathbf{x}_0 = (x_+^0, x_-^0, I_0 = 0)$ according to

$$V \approx V(\mathbf{x}_0) + \left.\frac{\partial V}{\partial x_+^{\text{surf}}}\right|_{\mathbf{x}_0} \bar{x}_+^{\text{surf}} + \left.\frac{\partial V}{\partial x_-^{\text{surf}}}\right|_{\mathbf{x}_0} \bar{x}_-^{\text{surf}} + \left.\frac{\partial V}{\partial I}\right|_{\mathbf{x}_0} I, \tag{5.32}$$

where

$$V(\mathbf{x}_0) = U_+(x_+^0) - U_-(x_-^0) \tag{5.33}$$

is the equilibrium voltage of the battery at the DoD linearisation point. Defining the deviation of the voltage from the equilibrium voltage at the linearisation point $\bar{V}^0 = V - V(\mathbf{x}_0)$ which is given by the linear approximation

$$\bar{V}^0 \approx \left.\frac{\partial V}{\partial x_+^{\text{surf}}}\right|_{\mathbf{x}_0} \bar{x}_+^{\text{surf}} + \left.\frac{\partial V}{\partial x_-^{\text{surf}}}\right|_{\mathbf{x}_0} \bar{x}_-^{\text{surf}} + \left.\frac{\partial V}{\partial I}\right|_{\mathbf{x}_0} I. \tag{5.34}$$

The partial derivative of the voltage V with respect to the input current I evaluated at the reference point is given by

$$\left.\frac{\partial V}{\partial I}\right|_{\mathbf{x_0}} = \frac{2RT}{\mathcal{F}} \left(\frac{\theta_3}{\sqrt{(1-x_+^0)x_+^0}\sqrt{1+(\theta_3 I_0)^2}} - \frac{\theta_6}{\sqrt{(1-x_-^0)x_-^0}\sqrt{1+(\theta_6 I_0)^2}} \right). \tag{5.35}$$

which simplifies to

$$\left.\frac{\partial V}{\partial I}\right|_{\mathbf{x}_0} = \frac{2RT}{\mathcal{F}} \left(\frac{\theta_3}{\sqrt{(1-x_+^0)x_+^0}} - \frac{\theta_6}{\sqrt{(1-x_-^0)x_-^0}} \right) = -R_{\text{ct}}^0(\boldsymbol{\theta}) \tag{5.36}$$

when substituting for $I_0 = 0$. This term can be interpreted as a charge transfer resistance and will therefore be denoted R_{ct}^0, resulting in the charge transfer voltage drop $\eta_{\text{ct}} = -R_{\text{ct}}^0 I$ in the voltage equation. The partial derivative with respect to

the surface stoichiometry in the cathode and anode are given respectively by

$$\left.\frac{\partial V}{\partial x_+^{\text{surf}}}\right|_{\mathbf{x}_0} = + \left.\frac{dU_+}{dx_+^{\text{surf}}}\right|_{x_+^{\text{surf}}=x_+^0} - I_0 \frac{RT}{\mathcal{F}} \frac{\theta_3\left(1-2x_+^0\right)}{\sqrt{1+\frac{\left(\theta_3 I_0\right)^2}{(1-x_+^0)x_+^0}}\left((1-x_+^0)x_+^0\right)^{3/2}} \tag{5.37}$$

and

$$\left.\frac{\partial V}{\partial x_-^{\text{surf}}}\right|_{\mathbf{x}_0} = - \left.\frac{dU_-}{dx_-^{\text{surf}}}\right|_{x_-^{\text{surf}}=x_-^0} + I_0 \frac{RT}{\mathcal{F}} \frac{\theta_6\left(1-2x_-^0\right)}{\sqrt{1+\frac{\left(\theta_6 I_0\right)^2}{(1-x_-^0)x_-^0}}\left((1-x_-^0)x_-^0\right)^{3/2}}. \tag{5.38}$$

Substituting for $I_0 = 0$ yields the simple expressions

$$\left.\frac{\partial V}{\partial x_+^{\text{surf}}}\right|_{\mathbf{x}_0} = \left.\frac{dU_+}{dx_+^{\text{surf}}}\right|_{x_+^{\text{surf}}=x_+^0} = \alpha_+^0 \quad \text{and} \quad \left.\frac{\partial V}{\partial x_-^{\text{surf}}}\right|_{\mathbf{x}_0} = - \left.\frac{dU_-}{dx_-^{\text{surf}}}\right|_{x_-^{\text{surf}}=x_-^0} = -\alpha_-^0 \tag{5.39}$$

where the α_i^0 denote the gradients of the open-circuit potential functions in each electrode, with respect to stoichiometry, at the linearisation point. Therefore, the linearised voltage measurement equation in the time domain becomes

$$\bar{V}(t) = \alpha_+^0 \bar{x}_+^{\text{surf}}(t) - \alpha_-^0 \bar{x}_-^{\text{surf}}(t) - R_{\text{ct}}^0(\boldsymbol{\theta}) I(t). \tag{5.40}$$

5.2.3 Transfer function of the linearised SP model

Taking the Laplace transform of the linearised voltage equation (5.40) and dividing by the input current I yields the transfer function of the linearised single particle model about the equilibrium point $\mathbf{x}_0 = (x_+^0, x_-^0, I_0 = 0)$

$$H^0(s, \boldsymbol{\theta}) = \frac{\bar{V}(s)}{I(s)} = \alpha_+^0 H_+^{\text{d}}(s, \boldsymbol{\theta}) - \alpha_-^0 H_-^{\text{d}}(s, \boldsymbol{\theta}) - R_{\text{ct}}^0(\boldsymbol{\theta}). \tag{5.41}$$

Substituting the anode and cathode diffusion transfer function H_+^{d} and H_-^{d} by their respective expressions (5.30) and (5.31) gives

$$H^0(s,\boldsymbol{\theta}) = \frac{\alpha_+^0\theta_2 \tanh\left(\sqrt{s\theta_1}\right)}{\tanh\left(\sqrt{s\theta_1}\right) - \sqrt{s\theta_1}} - \frac{\alpha_-^0\theta_5 \tanh\left(\sqrt{s\theta_4}\right)}{\tanh\left(\sqrt{s\theta_4}\right) - \sqrt{s\theta_4}} - R_{\mathrm{ct}}^0(\boldsymbol{\theta}) \tag{5.42}$$

One can see that only the difference between the parameters θ_3 and θ_6 describing the cathode and anode kinetics appears in the charge transfer resistance term $R_{\mathrm{ct}}(\boldsymbol{\theta})$ given by (5.36). As a result, there are clearly an infinite number of couples (θ_3, θ_6) that will yield the same transfer function and only the lumped parameter R_{ct} can be estimated using the linearised model at a given DoD. We have therefore reduced the parameter space to five parameters by combining the cathode and anode kinetics into the charge-transfer resistance term R_{ct}.

This assumes that the OCP slopes α_+^0 and α_-^0 are known parameters. However, these are not directly measurable, since in practice, OCP can be measured with respect to capacity (units Ah or Coulombs), not against stoichiometry (which is non-dimensional). By recognising that the theoretical capacity of an electrode is given by $Q_i^{\mathrm{th}} = c_i^{\max}\mathcal{F}V_i$ with $V_i = \epsilon A\delta_i$ (the volume of active material in the electrode), one can easily show that a variation of stoichiometry δx_i is proportional to a variation of charge/discharge capacity δQ according to

$$\delta x_i = \frac{\delta c_i}{c_i^{\max}} = \frac{\delta c_i \mathcal{F} V_i}{Q_i^{\mathrm{th}}} = \frac{\delta Q}{Q_i^{\mathrm{th}}}. \tag{5.43}$$

Therefore the derivative of the OCP with respect to x_i can be related to its derivative with respect to charge/discharge capacity Q, denoted β_i^0, according to

$$\beta_i^0 = \frac{\alpha_i}{Q_i^{th}} = \frac{1}{Q_i^{th}} \left.\frac{dU_i}{dx_i^s}\right|_{x_i^{s,0}} = \left.\frac{dU_i}{dQ}\right|_{x_i^{s,0}}. \tag{5.44}$$

Substituting α_i^0 for β_i^0 using (5.44) in (5.42) and recalling the expressions of Q_i^{th} in terms of θ_i in (5.18) yields the transfer function

$$H^0(s,\boldsymbol{\theta}) = \beta_+^0 f\left(s,\theta_1\right) - \beta_-^0 f\left(s,\theta_4\right) - R_{\mathrm{ct}}^0 \tag{5.45}$$

where the function f defined as

$$f\left(s,\theta_i\right) = \frac{1}{3}\frac{\theta_i \tanh\left(\sqrt{s\theta_i}\right)}{\tanh\left(\sqrt{s\theta_i}\right) - \sqrt{s\theta_i}}. \tag{5.46}$$

which is only parametrised by the electrode diffusion time constant θ_1 or θ_4 in the cathode or anode respectively. Despite the fact that only the diffusion time constants θ_1, θ_4 appear in (5.45–5.46) compared to θ_1, θ_4 as well as θ_2, θ_5 in (5.42), these equations are completely equivalent. In order to derive (5.45–5.46) from (5.42), one must express the factors $\alpha_+^0\theta_2$ and $\alpha_-^0\theta_5$ in (5.42) in terms of β_+^0 and β_-^0. For the cathode parameters $\alpha_+^0\theta_2$ for instance, this can be done by recalling that $\theta_1 = \tau_+^d$ and $\theta_2 = \tau_+^d/(3Q_+^{th})$ from (5.17), and substituting α_+^0 by $Q_+^{th}\beta_+^0$ as expressed in (5.44). A similar argument allows expressing the anode parameters $\alpha_-^0\theta_5$ in terms of β_-^0 in (5.42).

The coefficients β_+^0 and β_-^0 are the measurable and assumed known OCP gradients with respect to capacity in the cathode and anode respectively. This requires access to half-cell or reference electrode cell data, which may be obtained from commercially available cells as we have recently demonstrated [96, 94]. In the absence of individual electrode OCP data, it is not possible to parametrise the SP model directly, although it may be reasonable to use a two-electrode open-circuit voltage measurement combined with available OCP data from the literature for the graphite negative electrode to infer the positive electrode OCP function.

We have thus reduced the parameter estimation problem of the single-particle model to three independent parameters: the cathode diffusion time constant τ_+^{d}, the anode diffusion time constant τ_-^{d} and the charge-transfer resistance R_{ct}. We

will subsequently define the vector $\tilde{\boldsymbol{\theta}} \in \mathbb{R}^3$ of parameters to be identified as

$$\tilde{\boldsymbol{\theta}} = \begin{bmatrix} \tau_+^{\mathrm{d}} & \tau_-^{\mathrm{d}} & R_{\mathrm{ct}}^0 \end{bmatrix}^{\mathrm{T}}. \tag{5.47}$$

The transfer function of the linearised SP model expressed in terms of the three parameters defined in $\tilde{\boldsymbol{\theta}}$ is given by

$$H^0\left(s, \tilde{\boldsymbol{\theta}}\right) = \beta_+^0 f\left(s, \tau_+^{\mathrm{d}}\right) - \beta_-^0 f\left(s, \tau_-^{\mathrm{d}}\right) - R_{\mathrm{ct}}^0. \tag{5.48}$$

Figure 5.1 shows a Nyquist plot[3] of the SP model frequency response predicted

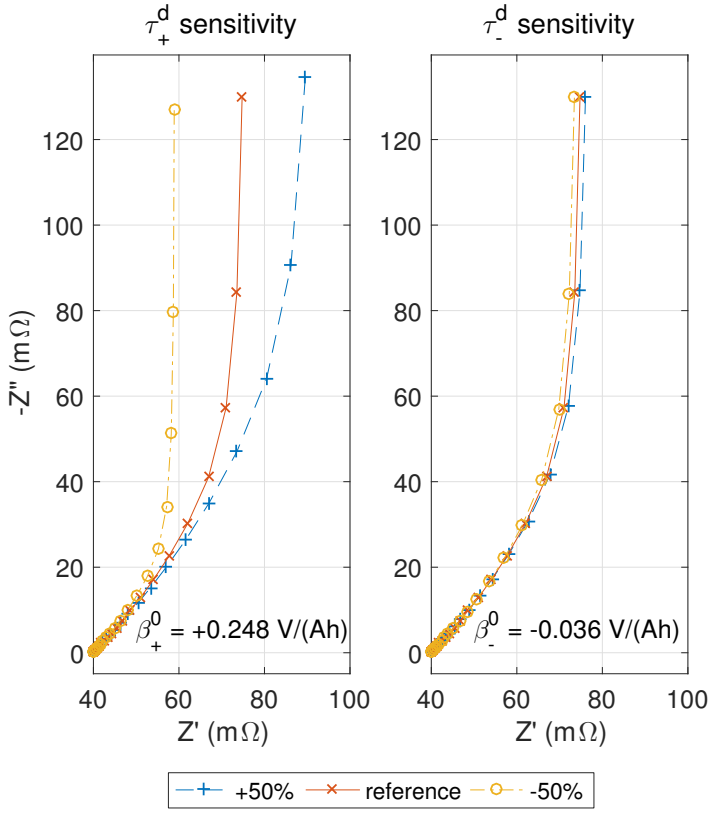

Fig. 5.1 Comparison of the Nyquist frequency response predicted by the transfer function (5.48) using the reference parameters given in Table 3.1 with (left) the cathode diffusion time constant τ_+^{d} and (right) the anode diffusion time constant τ_-^{d} varied by ±50 % from their nominal values [5].

by (5.48) at 25 % DoD for the LCO cell parameters given in Table 3.1. At low frequencies, the response shows a 45° slope, which is representative of semi-infinite linear diffusion. This 45° slope is commonly referred to as the 'diffusion tail' in the battery EIS community and is usually modelled using a so-called Warburg constant-phase element [160, 161]. The cell frequency response tends towards a capacitive behaviour with decreasing frequency as exhibited by the vertical asymptote on the Nyquist plot. This capacitive behaviour arises from the variation of the average particle concentration at low frequencies, as opposed to the surface concentration variation only, due to the finite-length nature of the diffusion problem. Although the low frequencies giving rise to this capacitive behaviour are usually avoided in the lithium-ion battery EIS literature, we argue that the departure from the semi-infinite diffusion 45° tail actually provides a more informative dataset for the parameter estimation of the SP model. Figure 5.1 also shows the effect of varying the diffusion time constant τ_+^d and τ_-^d in the cathode and anode respectively by ±50 % from their nominal values. Generally, a larger diffusion time constant (slow diffusion) yields higher cell impedance as expected. Moreover a smaller diffusion time constant (faster diffusion) results in the capacitive behaviour to happen at higher frequencies; this is because faster diffusion results in easier variations of the average particle concentration. Finally, the frequency response is much more sensitive to the cathode diffusion than the anode diffusion because of the flat anode OCP curve at this DoD, as shown by the low value of the anode OCP slope β_-^0 compared to β_+^0. This behaviour will be explained in more details in the subsequent sections.

[3] In the battery community, the frequency response of a cell measured by electrochemical impedance spectroscopy is conventionally plotted on the complex plane as its negative imaginary part $-Z''$ *vs* real part Z', which is actually the Nyquist plot of the conjugate of the frequency response. However, we will subsequently refer to this plot as the Nyquist plot of the cell frequency response for simplicity.

5.2.4 Structural identifiability analysis

Definition 1 of structural identifiability can now be applied to the SP model transfer function (5.48) parametrised by the three parameters in $\tilde{\boldsymbol{\theta}}$. Following Definition 1, to check the structural identifiability of the linearised model, we need to show that

$$\beta_+^0 f\left(s,\tau_+^{\mathrm{d}}\right)-\beta_-^0 f\left(s,\tau_-^{\mathrm{d}}\right)-R_{\mathrm{ct}}^0=\beta_+^0 f\left(s,\tau_+^{\mathrm{d}*}\right)-\beta_-^0 f\left(s,\tau_-^{\mathrm{d}*}\right)-R_{\mathrm{ct}}^{0*} \qquad \text{for almost all } s, \tag{5.49}$$

implies the equality of the parameters,

$$\begin{bmatrix}\tau_+^{\mathrm{d}} & \tau_-^{\mathrm{d}} & R_{\mathrm{ct}}^0\end{bmatrix}^{\mathrm{T}}=\begin{bmatrix}\tau_+^{\mathrm{d}*} & \tau_-^{\mathrm{d}*} & R_{\mathrm{ct}}^{0*}\end{bmatrix}^{\mathrm{T}}. \tag{5.50}$$

Because the charge transfer resistance is the only additive term independent of s on both side of the equation, we clearly have that $R_{\mathrm{ct}}^0 = R_{\mathrm{ct}}^{0*}$ and the structural identifiability equation reduces to

$$\beta_+^0 f\left(s,\tau_+^{\mathrm{d}}\right)-\beta_-^0 f\left(s,\tau_-^{\mathrm{d}}\right)=\beta_+^0 f\left(s,\tau_+^{\mathrm{d}*}\right)-\beta_-^0 f\left(s,\tau_-^{\mathrm{d}*}\right) \qquad \text{for almost all } s \tag{5.51}$$

Since f is a non-trivial function of the Laplace variable s, this equality holds in the general case for almost all s if and only if $\tau_+^{\mathrm{d}} = \tau_+^{\mathrm{d}*}$ and $\tau_-^{\mathrm{d}} = \tau_i^{\mathrm{d}*}$ and the linearised SP model is structurally identifiable. There are however a few cases where other solutions exist:

- If $\beta_+^0 = 0$ (resp. $\beta_-^0 = 0$), then any pair $(\tau_+^{\mathrm{d}}, \tau_+^{\mathrm{d}*})$ (resp. $(\tau_-^{\mathrm{d}}, \tau_-^{\mathrm{d}*})$) satisfy the identifiability equation and the linearised SP model becomes unidentifiable. This makes sense because a 'flat' open-circuit potential function hides any diffusion dynamics effect of that electrode as shown in Figure 5.1 for the anode diffusion when $|\,\beta_-^0\,| \ll |\,\beta_+^0\,|$.

- If the magnitudes of the open-circuit potential function in each electrode are equal $\beta_+^0 = -\beta_-^0 = \beta^0$, then interchanging the diffusion time constants $\tau_+^{\mathrm{d}} = \tau_-^{\mathrm{d}*}$ and $\tau_-^{\mathrm{d}} = \tau_+^{\mathrm{d}*}$ satisfies the structural identifiability equation, and the linearised SP model is structurally identifiable provided the diffusion time constants are ordered.

In conclusion, the linearised SP model is structurally identifiable in the general case. In practice, the fact that a 'flat' open-circuit potential function results in unidentifiable parameters may not be as problematic as it sounds, since identification may performed using data at several DoDs, ensuring the OCP functions have a significant slope in each electrode.

5.3 Frequency-domain parameter estimation

This section discusses the implementation of the estimation algorithm for the transfer function of the linearised SP model from frequency-domain EIS experimental data. The experimental set up is discussed in Section 5.4.2. We define the vector $\boldsymbol{\theta}_{\mathrm{id}}$ of parameters identified by the estimation algorithm. Therefore, depending on the parameter estimation algorithm considered $\boldsymbol{\theta}_{\mathrm{id}}$ could be equal to the full vector of parameters $\boldsymbol{\theta}$ given by (5.17) or a subset of parameters such as $\tilde{\boldsymbol{\theta}}$ given by (5.47). The estimation is performed by finding the best fit in the least-squares sense, *i.e.* by minimising the sum of squared error between both the real and imaginary part of the experimental and predicted impedance at several frequencies. First, the loss function for the parameter estimation at a single DoD is presented and then extended to the simultaneous estimation at several DoDs. Then, we show how the charge-transfer resistance R_{ct} at a given DoD can be estimated beforehand by simple linear regression.

5.3.1 Single DoD parameter estimation

The experimental electrochemical impedance of a cell at a given frequency ω_i is denoted by the complex number $Z_j(\omega_i) = Z'_j(\omega_i) + iZ''_j(\omega_i)$, where Z' and Z'' denote the real and imaginary part of the impedance respectively, and the subscript j denotes the DoD[4]. Similarly, the impedance predicted by the SP model will be denoted $H_j(\omega_i, \boldsymbol{\theta}_{\text{id}})$ in the subsequent sections.

In the case where parameter estimation is performed on impedance data at a single DoD denoted by the subscript j, the algorithm minimises the loss function $L_j(\boldsymbol{\theta}_{\text{id}})$ defined as

$$L_j(\boldsymbol{\theta}_{\text{id}}) = \sum_{i=1}^{N_\omega} |Z_j(\omega_i) - H_j(\omega_i, \boldsymbol{\theta}_{\text{id}})|^2 . \tag{5.52}$$

This loss function is the sum over N_ω chosen frequencies of the squared complex magnitude of the error between predicted and measured impedance. This is also equal to the sum of the squared real part and imaginary part error according to

$$L_j(\boldsymbol{\theta}_{\text{id}}) = \sum_{i=1}^{N_\omega} \left(Z'_j(\omega_i) - H'_j(\omega_i, \boldsymbol{\theta}_{\text{id}})\right)^2 + \sum_{i=1}^{N_\omega} \left(Z''_j(\omega_i) - H''_j(\omega_i, \boldsymbol{\theta}_{\text{id}})\right)^2 . \tag{5.53}$$

The optimal parameter estimate in the least-squares (maximum likelihood) sense is therefore given by the estimator $\hat{\boldsymbol{\theta}}_{id}$ which minimises the loss function according to:

$$\hat{\boldsymbol{\theta}}_{\text{id}} = \arg\min_{\boldsymbol{\theta}_{\text{id}}} L_j(\boldsymbol{\theta}_{\text{id}}) = \sum_{i=1}^{N_\omega} |Z_j(\omega_i) - H_j(\omega_i, \boldsymbol{\theta}_{\text{id}})|^2 \tag{5.54}$$

5.3.2 Combined DoDs parameter estimation

As mentioned in Section 5.2.4 and shown in Section 5.4, the estimation of the parameter $\tilde{\boldsymbol{\theta}}$ based on the impedance data at a single DoD is unidentifiable in practice due to the flatness of one of the electrode open-circuit potential func-

[4]Note that the index j denoting DoDs should not be confused with the same notation used for the reaction rate.

tions. Therefore, the parameter estimation must be performed against impedance measured at several DoDs. The loss function $L(\boldsymbol{\theta}_{\mathrm{id}})$ in this case is simply defined as the sum of the loss functions L_j defined in (5.53) over N_{DoD} levels of DoD according to

$$L(\boldsymbol{\theta}_{\mathrm{id}}) = \sum_{j=1}^{N_{\mathrm{DoD}}} L_j(\boldsymbol{\theta}_{\mathrm{id}}) = \sum_{j=1}^{N_{\mathrm{DoD}}} \sum_{i=1}^{N_\omega} |Z_j(\omega_i) - H_j(\omega_i, \boldsymbol{\theta}_{\mathrm{id}})|^2, \tag{5.55}$$

where j denotes the DoD. Again, the optimal parameter estimate is given by the argument $\hat{\boldsymbol{\theta}}_{\mathrm{id}}$ minimising the loss function according to

$$\hat{\boldsymbol{\theta}}_{\mathrm{id}} = \arg\min_{\boldsymbol{\theta}_{\mathrm{id}}} L(\boldsymbol{\theta}_{\mathrm{id}}) = \sum_{j=1}^{N_{\mathrm{DoD}}} \sum_{i=1}^{N_\omega} |Z_j(\omega_i) - H_j(\omega_i, \boldsymbol{\theta}_{\mathrm{id}})|^2. \tag{5.56}$$

5.3.3 Estimation of the charge-transfer resistance by linear regression

Although the simultaneous parameter estimation at several DoDs could in theory improve the identifiability of the estimation problem, it also adds N_{DoD} charge transfer resistances R^0_{ct} to identify because of the dependency of R^0_{ct} on stoichiometry (or equivalently DoD) in (5.36). The charge-transfer resistance R^0_{ct} is an additive purely resistive term in the transfer function describing the cell impedance. Therefore, it only shifts the impedance response along the real-axis on the Nyquist plot. In order to reduce the parameter space to be explored, the charge-transfer resistance R^0_{ct} can be estimated separately by simple linear regression and subtracted from the experimental frequency-response data. Recalling from Section 5.2.3 that the semi-infinite diffusion-driven impedance at higher frequencies feature a characteristic 45° slope, the charge-transfer resistance can be estimated by fitting a 45° straight line to the experimental response at lower frequencies, and extrapolating to find the intercept of this with the real axis on the Nyquist diagram. We assume that any high-frequency data points of the

experimental EIS where charge-transfer processes are dominant (charge-transfer semicircle), have been removed; only data points at frequencies where diffusion processes are predominant remain.

Denoting $x_i = Z'(\omega_i)$ and $y_i = -Z''(\omega_i)$ the real part and negative imaginary part respectively of the experimental impedance at frequency ω_i, the linear regression problem is

$$y_i = \beta_1 x_i + \beta_0. \tag{5.57}$$

The slope is set to 45° to represent the diffusion behaviour as discussed previously. Therefore $\beta_1 = 1$ is known and the regression problem consists of estimating β_0 only from the experimental data. The charge-transfer resistance is then determined by calculating the intercept of the linear regression with the real axis of the Nyquist plot according to $R_{\text{ct}}^0 = -\beta_0$. Defining the variable $\bar{y}_i = y_i - \beta_1 x_i$, the regression problem can be written:

$$\bar{y}_i = \beta_0. \tag{5.58}$$

This therefore constitutes an over-determined system of N_ω equations with the only unknown β_0, which can be written

$$\bar{\mathbf{Y}} = \beta_0 \mathbf{1}, \tag{5.59}$$

where $\bar{\mathbf{Y}} = [\bar{y}_1, \ldots, \bar{y}_{N_\omega}]^{\mathrm{T}} \in \mathbb{R}^{N_\omega}$ is the vector containing the values of $\bar{y}_i$ at the N_ω frequencies, and $\mathbf{1} \in \mathbb{R}^{N_\omega}$ is a vector of all ones of length N_ω. The value of β_0 can easily be determined in the least-squares sense by computing

$$\beta_0 = \mathbf{1}^\dagger \bar{\mathbf{Y}} = \frac{\mathbf{1}^{\mathrm{T}}}{N_\omega} \bar{\mathbf{Y}} \tag{5.60}$$

where the superscript $\mathbf{1}^\dagger$ denotes the pseudo-inverse of the vector $\mathbf{1}$ which is simply equal to a row vector with all components equal to $1/N_\omega$. This linear regression must be performed only using the experimental data points in the

frequency range where low-frequency capacitive effects are negligible. Therefore, low-frequency impedance data points are be discarded from the experimental dataset to perform a meaningful regression. In practice, this was achieved by performing the regression first on all data points, and then on a reduced dataset where the lowest frequency impedance data point was removed until the goodness-of-fit was satisfactory. The coefficient of determination R^2 was used as an indicator to assess the goodness-of-fit and a threshold value of 0.98 was chosen to stop the iterations.

5.4 Results and discussion

5.4.1 Parameter estimation using synthetic data

The parameter estimation algorithm was first tested against synthetic data generated using the linearised SP model with the same set of parameters for an LCO cell from the literature [2] given in Table 3.1 for the P2D model. Figure 5.2 shows contour plots of the natural logarithm of the loss function $L_j\left(\tilde{\boldsymbol{\theta}}\right)$, (5.53), at several DoDs for the synthetic data. It is assumed that the charge-transfer resistance R_{ct} is known for each DoD since, as previously explained, it can be identified separately by straightforward linear regression. Therefore the two parameters to be identified are the cathode and anode diffusion time constants τ_+^{d} and τ_-^{d} respectively. The coordinates of the minimum values of the natural logarithm of (5.53) on these contour plots represent the optimal parameter estimates in the least-squares sense as defined in (5.54). The two cases for which the linearised SP model is structurally unidentifiable, as discussed in Section 5.2.4, can be witnessed by examining figure 5.2. Firstly, when the absolute value of the OCP functions are approximately equal in the cathode and anode, $\beta_+ \approx -\beta_-$, such as 75 % DoD, the loss function clearly shows two minima: one minimum corresponds to the actual parameters, while the other minimum occurs when the anode and

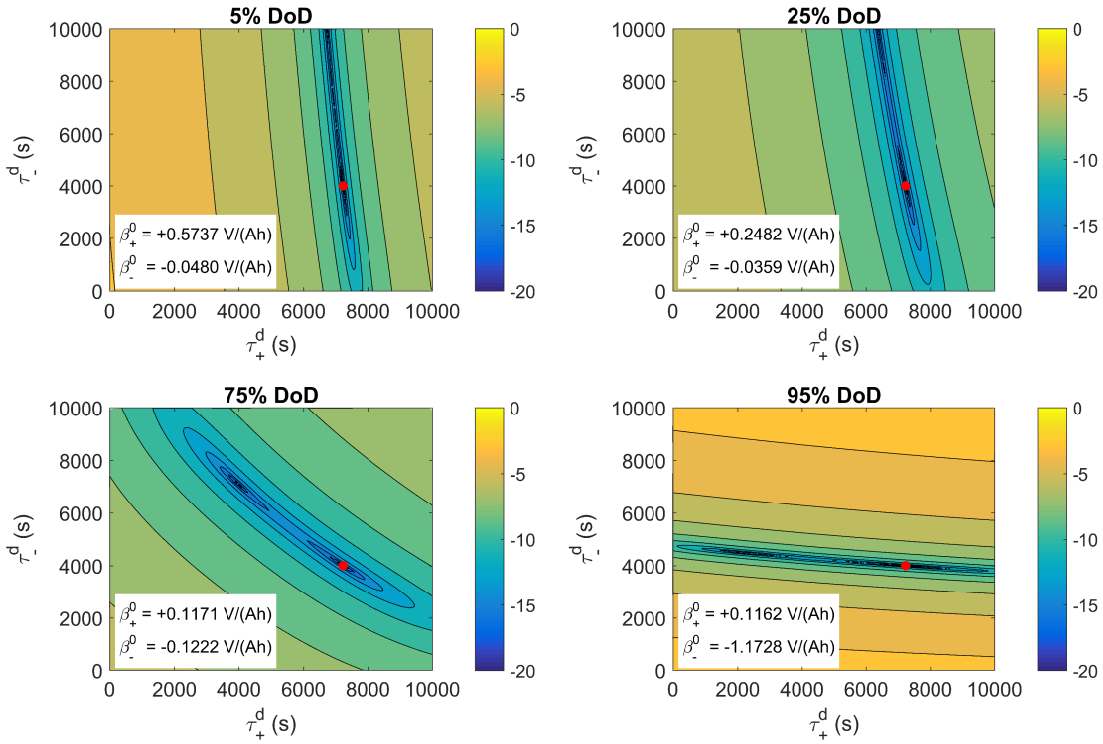

Fig. 5.2 Contour plots of $\ln L_j\left(\tilde{\boldsymbol{\theta}}\right)$ against $(\tau_+^{\mathrm{d}}, \tau_-^{\mathrm{d}})$ at several DoDs assuming the charge-transfer resistance R_{ct} is known. Synthetic EIS data were generated using the linearised SP model with reference parameters found in the literature [2] for an LCO cell (shown as a red dot on the contour plot) [5].

cathode diffusion time constants are interchanged. Moreover, even if the absolute values of the electrode OCP slopes β_-^0 and β_+^0 are distinct (e.g. 5 %, 25 % and 95 % on figure 5.2), the loss function still features two local minima, although barely visible due to the narrow loss function along one axis. Therefore, an ambiguity persists and the anode and cathode dynamics cannot be distinguished. A possible explanation for this ambiguity is that the measured voltage is the difference between the anode and cathode OCP and not the absolute voltage of the electrode with respect to a reference electrode. Secondly, in the case where one OCP slope is an order of magnitude lower in one electrode compared to the other, the diffusion time constant of this electrode becomes unidentifiable, *e.g.* 5 %, 25 % and 95 % DoD in figure 5.2. For instance at 95 % DoD, the absolute value of the cathode OCP slope β_+ is small compared to the anode one, and the

minimum of the loss function is elongated along the τ_+^{d} axis, *i.e.* provided the value of τ_-^{d} is correct, almost any value for τ_+^{d} will result in a minimum value of the loss function.

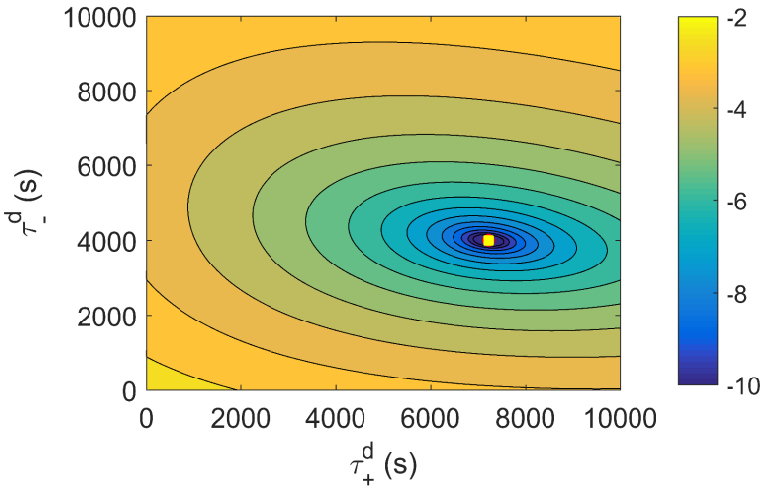

Fig. 5.3 Contour plots of $\ln L\left(\tilde{\boldsymbol{\theta}}\right)$ against $(\tau_+^{\mathrm{d}}, \tau_-^{\mathrm{d}})$ assuming the charge-transfer resistance R_{ct} is known, based on synthetic EIS data with the reference parameters from [2] for an LCO cell (shown as a yellow square on the contour plot). The loss function is the sum of the cost function L_j for four levels of DoD 5 %, 25 %, 75 % and 95 % [5].

These results suggest that the anode and cathode diffusion time constants cannot both be identified from frequency-data at a single DoD. In the best case, where the OCP slopes are equal for the chosen DoD, the values τ_+^{d} and τ_-^{d} can be determined but cannot be assigned to a specific electrode. Figure 5.3 shows the natural logarithm of the loss function $L\left(\tilde{\boldsymbol{\theta}}\right)$ combining the EIS data at 5 %, 25 %, 75 % and 95 % DoD as defined in (5.55). This loss function shows a single global minimum corresponding to the actual set of parameters used to generate the synthetic data. The two time constants of the linearised SP model can therefore only be estimated unambiguously by considering EIS data at several DoDs. More specifically, complementary DoD values where each electrode in turn presents a large OCP slope while the other is negligible should be combined to ensure better identifiability. For instance, it is clear from Figure 5.2 that combining EIS data at

5 % and 95 % DoD will result in a single minimum at the intersection of the lines of minimum loss function values for individual DoDs.

5.4.2 Parameter estimation using experimental data

This section discusses the results of the parameter estimation using EIS experimental data measured from a commercial Kokam NMC cell. First, the experimental procedure used to measure the cell impedance and the OCP for both electrodes is discussed. The estimation of the charge-transfer resistance using linear regression is then briefly considered. Finally, the practical identifiability of the model diffusion time constants from the experimental impedance data is examined.

Experimental setup

Electrochemical impedance spectroscopy experimental data were obtained for a Kokam SLPB533459H4 740 mA h NMC cell at several DoDs using a BioLogic SP-150 potentiostat. The cell was kept at a constant 20 °C temperature in a Vötsch VT4002 thermal chamber. The cell impedance was measured using single-sine Galvanostatic Electrochemical Impedance Spectroscopy (GEIS) with a peak-to-peak current amplitude of 100 mA and averaged over two periods. The impedance was measured at logarithmically-spaced frequencies with six frequencies per decade ranging from 5 kHz to 200 µHz. A resting time of 3 hours was used before any EIS measurement to ensure that the cell was close to equilibrium. The EIS measurement using this experimental setup took approximately 9 hours for each DoD because of the low frequency required. Clearly, the measurement of EIS at low frequency is quite time consuming and ultimately one should aim at using the minimum number of low-frequency data and/or DoD linearisation points to accelerate the model parametrisation. Figure 5.4 shows the measured EIS data as a Nyquist plot for several DoDs ranging from 10 % to 90 %. At high frequencies, the frequency response features a depressed semicircle, which is characteristic of

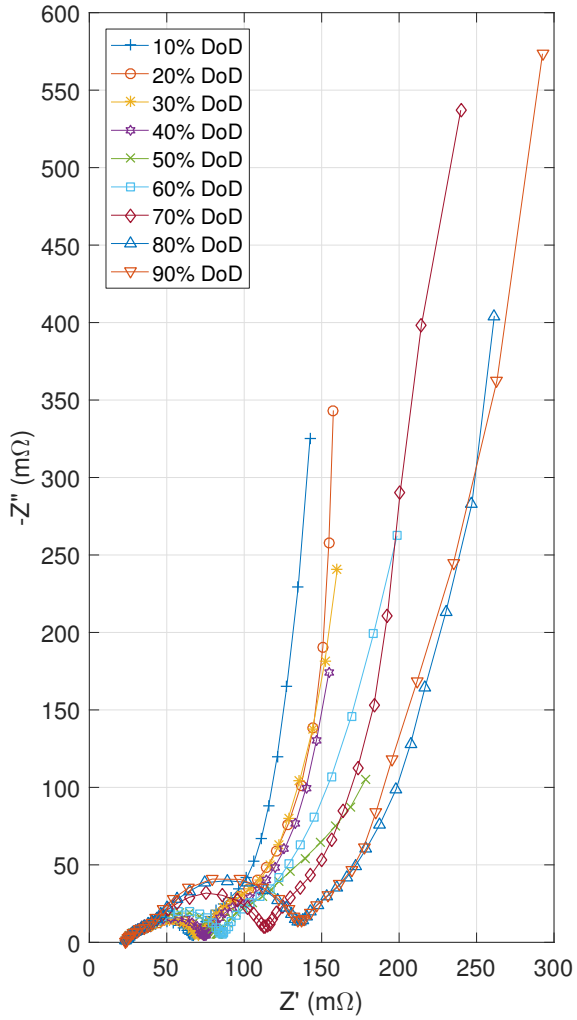

Fig. 5.4 Nyquist plot of the electrochemical impedance of a Kokam SLPB 533459H4 740 mA h NMC cell measured at 20 °C and several DoDs in the frequency range 5 kHz to 200 µHz [5].

charge-transfer processes. As discussed in Section 5.3.3, this part of the plot is discarded because charge-transfer processes are approximated by the resistor R^0_{ct} only in (5.48). As expected, in the medium range of frequency where semi-infinite diffusion is predominant, the frequency response shows the familiar 45° diffusion slope. At very low frequencies the response tends towards a capacitive vertical line due to the variations of the average particle stoichiometry.

Figure 5.6d shows the open-circuit potential of the Kokam SLPB533459H4 cell as a function of discharge capacity Q and DoD measured experimentally. In order to measure the anode and cathode potential separately, a minimally invasive reference electrode consisting of a lithium-coated copper wire was inserted into the commercial pouch cell using the technique presented in [94]. The OCV and the OCP of both electrodes were then measured using the galvanostatic intermittent titration technique (GITT) [96] by discharging the cell in 14.8 mA h increments at $C/10$ and measuring the cell open-circuit voltage after a one-hour voltage relaxation time to obtain 50 measurements points.

Charge-transfer resistance estimation

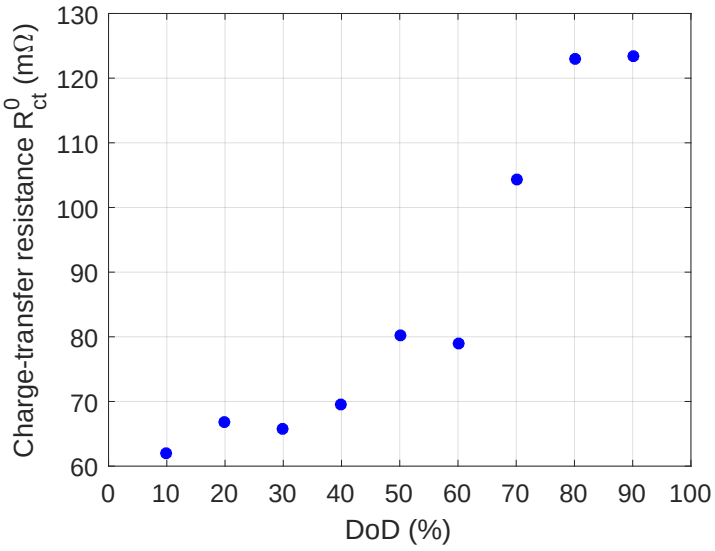

Fig. 5.5 Charge-transfer resistance against DoD estimated from experimental data by linear regression [5].

The values of the charge-transfer resistance R^0_{ct} estimated using the linear regression method discussed in Section 5.3.3 as a function of DoD are reported on figure 5.5. Note that R^0_{ct} as we have defined it includes the cell ohmic resistance, which is approximately 25 mΩ according to the intercept of experimentally measured impedance with the real-axis of the Nyquist plot at high frequencies, figure 5.4. As shown, the sum of the charge-transfer and ohmic resistances increases with DoD, which is consistent with previously reported Kokam NMC cell EIS data in the literature [162].

Parameter estimation performance

Figure 5.6 presents practical identifiability and parameter estimation results based on experimental impedance data at individual DoDs. Three characteristic values of DoD where chosen, 10 %, 50 % and 80 %, in order to demonstrate the identifiability issues discussed in Section 5.2.4. At 10 % DoD only the cathode OCP shows a significant slope, at 50 % DoD both the cathode and anode OCP are flat, and at 80 % DoD both electrodes feature a significant OCP slope. The experimental and fitted impedance responses are shown in Figures 5.6e, f and g for the chosen values of DoD. A satisfactory fit is obtained in all cases with a root-mean square error of 3.28 mΩ, 9.56 mΩ and 6.48 mΩ for 10 %, 50 % and 80 % DoD respectively.

However, the uncertainty on the parameter estimate is very large, as exhibited by the contour plots of the loss function on Figures 5.6a, b and c. At 10 % DoD, the loss function is very sensitive to the cathode diffusion dynamics, while anode dynamics have very little impact because of the very small slope of the anode OCP. Therefore the estimated anode diffusion time constant τ^{d}_{-} is highly uncertain and cannot be estimated from this data set alone. By contrast, at 80 % DoD the loss function is sensitive to both the anode and cathode dynamics because of the similar magnitude of the OCP slope in both electrodes. However, the minimum of the loss function is still relatively elongated along the anode parameter axis,

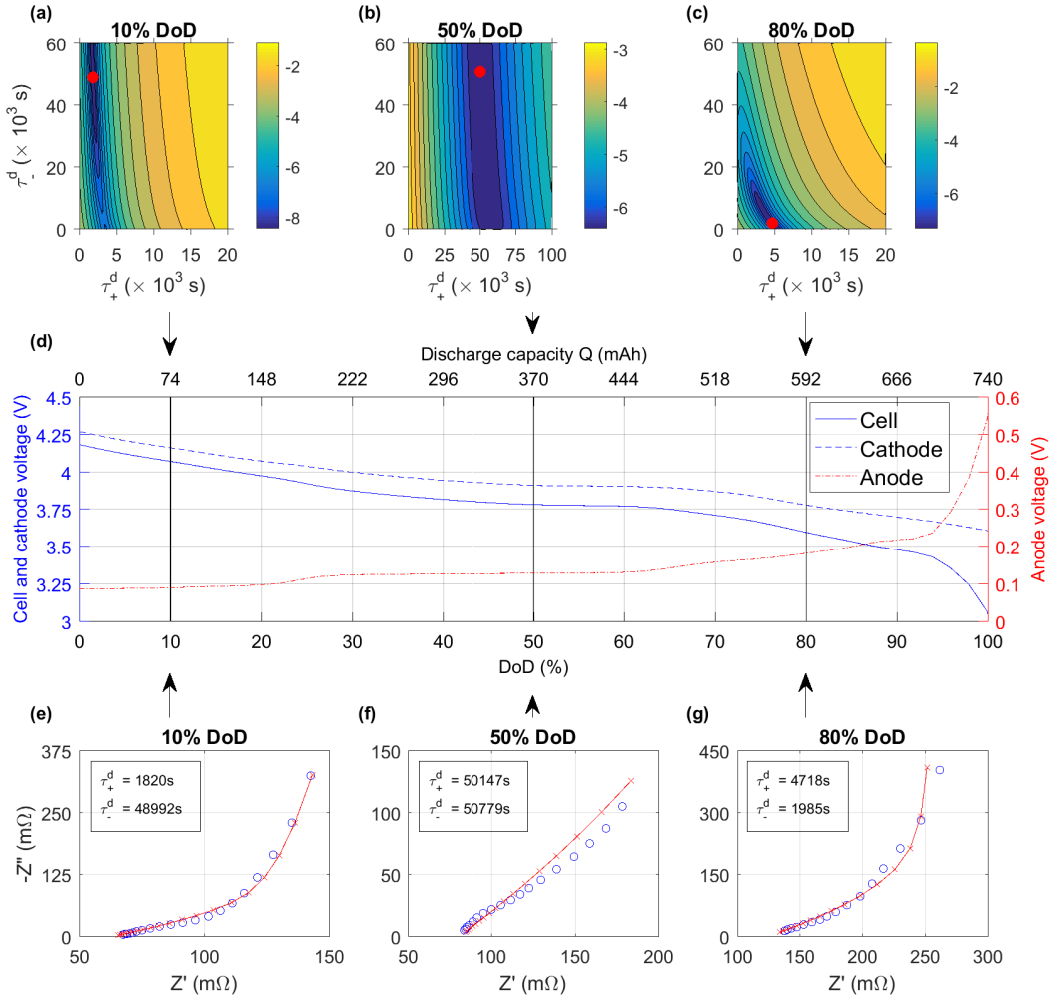

Fig. 5.6 Natural logarithm of the individual DoD loss function $L_j\left(\tilde{\boldsymbol{\theta}}\right)$ based on experimental EIS data at (a) 10 %, (b) 50 %, and (c) 80 % DoD. (d) Cathode OCP, anode OCP and cell OCV of the Kokam cell as a function of DoD measured by the GITT technique using a minimally invasive reference electrode. Cell impedance experimentally measured (circles) and predicted (solid-lines and crosses) by the linearised SP model transfer function model fitted by minimising the individual DoD loss function $L_j\left(\tilde{\boldsymbol{\theta}}\right)$ at (e) 10 %, (f) 50 %, and (g) 80 % DoD [5].

which suggests that the uncertainty on the anode parameter remains larger than the cathode one. This confirms that impedance data at several DoDs must be combined to yield trustworthy parameter estimates.

At 50 % DoD, where the OCP is flat for both electrodes, the loss function is insensitive to the anode dynamics and somewhat more sensitive to the cathode dynamics. However, the contour plot of the loss function is actually shallow along the cathode parameter as well, which means that the uncertainty on both parameters is very large. Furthermore, the minimum of the loss function happens for a cathode diffusion time constant centred around 60 000 s, Figure 5.6b. This is approximately an order of magnitude higher than the value of τ_+^{d} estimated using the other data sets at 10 % and 80 % DoD. Throughout this work, the implicit assumption was made that both diffusion time constants do not vary with DoD. However, figure 5.6b suggests that lithium diffusivity in the electrode active material could drastically change with DoD. Experimental measurements of lithium diffusivities in the active material of a Kokam NMC cell are reported in [163] and confirm that lithium diffusivity can indeed vary by an order of magnitude depending on material lithiation. More especially, both the anode and cathode diffusivities are an order of magnitude lower around 50 % DoD compared to high DoDs for instance [163]. Furthermore, another source of uncertainty that has been ignored in the model is the error related to the OCP measurement and the calculation of the OCP slopes β_+^0 and β_-^0. At 50 % DoD, the OCP slopes in both electrodes are very small and therefore the relative error on measurement is large, especially considering that numerical differentiation is highly sensitive to noise. Finally, because of the flatness of the OCP slopes both the anode and cathode diffusion dynamics have very limited effects on the cell terminal voltage at 50 % DoD. Therefore, the EIS data at 50 % DoD will be discarded from the parameter estimation using combined DoDs discussed subsequently.

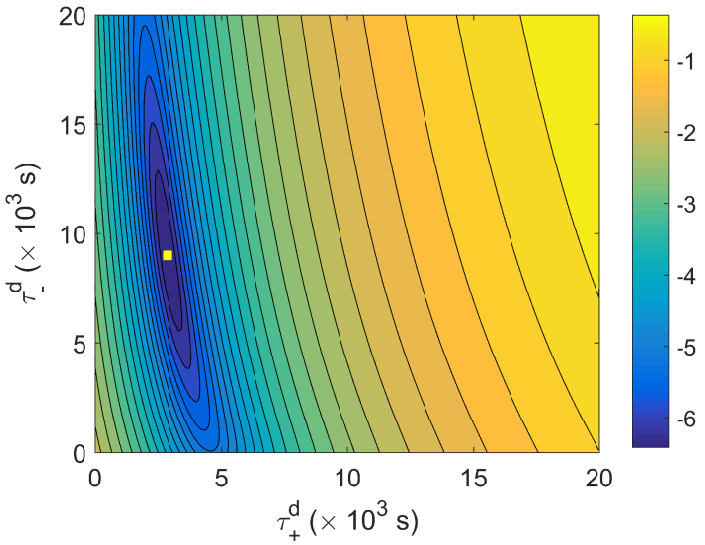

Fig. 5.7 Contour plot of the loss function $\ln L\left(\tilde{\boldsymbol{\theta}}\right)$, (5.55), based on experimental impedance data at 10 % and 80 % DoD. The yellow square indicates the estimated parameter [5].

Figure 5.7 shows the contour plot of the cost function $L\left(\tilde{\boldsymbol{\theta}}\right)$ combining the experimental impedance data measured at 10 % and 80 % DoDs. Similarly to the results on synthetic data, figure 5.3, the loss function presents a single minimum, elongated along the anode parameter axis suggesting a larger uncertainty on the anode parameter compared to the cathode one. Although figure 5.7 suggests a 'well-behaved' estimation problem with a single parameter estimate, these results must be considered with caution. Indeed, the two combined datasets at 10 % and 80 % DoDs used to perform the parameter estimation were chosen somehow arbitrarily. Although these parameter estimates yield a good impedance fit for these DoDs, it results in very approximate fitted impedance at other DoDs, e.g. 50 % DoD. Firstly, as previously mentioned the OCP slopes β_i in both electrodes are assumed fixed and perfectly known for each DoD. The sensitivity of the predicted impedance response on the OCP slopes is not negligible. On the one hand, the computation of the OCP slope is highly sensitive to measurement noise because the measured voltage variations are relatively small between each DoDs, in the other order of a few millivolts. Further numerical errors are also introduced

by interpolating between the 50 measurement points of the experimental OCP curves. Moreover, our calculation of DoD is based on Coulomb counting which is prone to integration of error over time. On the other hand, the measured OCP might not reflect closely enough the actual cell OCP. The OCP measurements were performed on a different cell which was modified by inserted a reference electrode. Although this technique is minimally invasive, it nonetheless modifies the cell behaviour. Finally, electrode OCP is affected by temperature variation and hysteresis effects [96], which introduce further uncertainties. Secondly, our parameter estimation algorithm combining experimental data at several DoDs assumes that the diffusion time constants in both electrodes remain constant with DoD. Although solid-phase diffusivities are usually assumed constant with respect to active material lithiation in the lithium-ion battery electrochemical modelling community, e.g. [2, 62, 82, 28, 132], this assumption may introduce additional inaccuracies on the parameter estimate, especially for NMC cells [163].

5.5 Concluding remarks

The analysis of parameter identifiability from experimental data is essential prior to any attempt at estimating the parameters of battery first-principle models. It has been demonstrated that the lithium-ion battery SP model is over-parametrised and that only six subgroups of parameters are necessary to fully parametrise the model. Assuming that the open-circuit potential *vs.* discharge capacity curves for each electrode are known, it is shown that the estimation of the linearised SP model parameters at a given DoD can only identify three parameters among these six subgroups of parameters, namely the cathode diffusion time constant τ_+^{d}, the anode diffusion time constant τ_-^{d} and a charge-transfer resistance R_{ct}. Finally, the study shows the crucial role of the slope of electrode OCP curves on the parameter uncertainty. A flat electrode open-circuit potential curve results in

high uncertainties on this electrode diffusion parameter. Therefore impedance data at a single DoD cannot, in general, result in accurate parameter estimation for both electrodes and experimental data at multiple DoDs must be considered. Specifically, complimentary DoDs where in turn the anode and cathode open-circuit potential gradients are significant must be chosen to yield satisfactory parameter identifiability.

Chapter 6

Conclusion

The work on battery electrochemical modelling presented in this dissertation has led to several contributions that are summarised and highlighted in this concluding chapter.

6.1 Summary of dissertation and contributions

Fast solution of the P2D electrochemical model. In Chapter 2, we presented the P2D electrochemical battery model from the literature, which is the *de facto* high-fidelity model of choice for lithium ion battery understanding and design, but is often considered too computationally costly for control and monitoring applications. The fast solution of the P2D model using the Chebyshev orthogonal collocation method in MATLAB® presented in Chapter 3 is the first major contribution of this dissertation. Unlike most model order reduction approaches reported in the existing literature, the orthogonal collocation method employed here does not affect the physical significance of the model, despite greatly reducing its computational cost. Furthermore, the solution of the P2D model using orthogonal collocation on decomposed domains is arguably as accurate as, if not more accurate than, that of finite-difference. Although a similar solution of the P2D model was proposed earlier by Northrop *et al.* [86], the implementation presented

here is advantageous on several points. First, orthogonal collocation is used for the discretisation of both the macro- and micro-scale partial-differential equations of the P2D model. Our implementation is therefore unified and more flexible in comparison, because there is no need to switch between a micro-scale model discretised using a low-order approximation for low C-rates and the finite-difference method at high C-rates; low- and high-current operations can both be modelled efficiently by simply adjusting the number of collocation nodes in the different cell domains. Second, in the present work the number of algebraic constraints is reduced from $3\left(N_{\mathrm{a}}+N_{\mathrm{c}}\right)+N_{\mathrm{s}}$ to just $N_{\mathrm{a}}+N_{\mathrm{c}}+2$ where N_{a}, N_s, N_{c} the number of collocation nodes in the anode, separator and cathode domains respectively. As explained in Chapter 3, this is because (i) explicit expressions for solid-phase and electrolyte potentials are obtained by reformulating Ohm's law and MacInnes' equation in their integral rather than differential forms, and (ii) particle surface concentration can be removed from the algebraic state vector by using the reaction rate instead. Finally, our fast solution of the P2D model is implemented in MATLAB®, and solved much like a system of ODEs using the solver *ode15s*, which hopefully makes this implementation easier to apprehend and faster to deploy in future control applications. The open-source MATLAB® implementation of the simpler SP model discretised using the Chebyshev orthogonal collocation method [164] is already available at https://github.com/adrienBizeray/Spectral_li-ion_SPM.

State estimation of the full P2D electrochemical model. Another major contribution of this dissertation is the algorithm for the recursive estimation of internal electrochemical lithium-ion battery states derived in Chapter 4, based on the fast P2D model solution proposed in Chapter 3. The P2D model state estimation has been previously reported in [63] using the optimisation-based moving horizon technique and in [64] using tethered particle filtering with a simplified solid-phase diffusion model, however the approach presented here using

the simpler EKF algorithm is much less computationally intensive while showing good performance. To our knowledge, this work is the first attempt at estimating the states of the fully spatially-distributed P2D model using the EKF algorithm. The results presented in this work show that the electrochemical SP and P2D models can be used in principle for electrochemistry-aware monitoring algorithms. The prospective applications of electrochemical model based-state estimation will be discussed in further details in Section 6.2.

Structural identifiability analysis of the SP model. The existing literature on parameter estimation presented in Chapter 1 clearly shows the limitations of standard optimisation techniques for the identification of electrochemical model parameters from experimental data. The conclusions that can be drawn from the literature are that (i) electrochemical model parameter estimation is plagued by unidentifiability issues, *i.e.* not all model parameters can be identified, and (ii) the set of parameters to identify must be carefully chosen by taking into considerations the model structure and the experimental identification data available. The structural identifiability analysis of the SP model derived in Chapter 5 gives insight regarding why, and under which conditions, some model parameters are unidentifiable from a mathematical perspective. To the extent of our knowledge, this work is the first to investigate the structural identifiability of an electrochemical battery model.

Frequency-domain parameter estimation of the SP model. In Chapter 5, a parameter estimation algorithm for the SP model is introduced based on the knowledge gained from the structural identifiability analysis. To the best of our knowledge, the present approach is the first reported attempt at directly identifying the physical parameters of the SP model from electrochemical impedance spectroscopy data. Despite the limitations of the preliminary approach presented in this work, the use of frequency-domain data instead of time-domain data may

lead to more robust and faster parameter estimation algorithms for electrochemical models.

Implementation of orthogonal collocation for BVPs. Aside from the contributions to lithium-ion battery modelling specifically, the detailed discussion in Chapter 3 of the practical implementation of orthogonal collocation for the discretisation of boundary-value problems also constitutes an important contribution of the present work. Although the incorporation of boundary conditions and computational domain decomposition for applying orthogonal collocation to more complex geometries have been discussed in principle [135], the linear algebra manipulations involved with the practical implementation of these techniques are not available in the literature.

6.2 Future work and perspectives

Research on electrochemical model-based monitoring and control of lithium-ion batteries is still in an early stage. There are still challenges to overcome before electrochemical models can be solved online in the next generation of BMSs, which also means that there are exciting research opportunities in this area. Some of these challenges and possible avenues of research for improving the approaches presented in this dissertation, along with future research perspectives, are discussed in this final section.

A first remaining challenge resides in the online solution of electrochemical models in embedded systems. Although the present work constitutes an important step towards the embedded solution of the P2D model by drastically reducing its computational cost, the differential–algebraic nature of the model remains problematic for its integration in embedded systems. This problem is illustrated by the fact that the solver *ode15s* for stiff ODEs and semi-explicit DAEs used in this work is not supported by the Embedded MATLAB® capabilities for automatically

generating embedded C code. This is because the variable time stepping approach used by *ode15s* for solving the DAE system cannot guarantee the solution convergence within the allowed time frame for real-time embedded computing. Recently, the solution of the P2D model using the so-called ε-embedded approach was proposed [77, 165]. The technique consists of solving a stiff system of ODEs, close to the original DAEs, by approximating the algebraic constraints by ODEs with very small time derivatives. Although this may be an interesting approach to explore further, the convergence to the actual solution is not guaranteed and the solution of stiff ODEs online in embedded systems remains problematic in terms of computational cost and algorithm robustness. In contrast, the embedded solution of the SP model online in a BMS is already possible because it only consists of ODEs with no algebraic constraint. Therefore, adopting a 'bottom-up' approach from the SP model could yield a faster advent of commercial electrochemical model-based BMSs.

Another unresolved challenge relates to the identification of reliable parameters for such electrochemical models. The approach to parameter estimation introduced in this dissertation is promising. First, the identification in principle of the minimum number of grouped parameters required to fully parametrise the model from a mathematical point of view is a relatively easy step that should be performed before attempting any model parameter estimation. The application of the structural identifiability analysis presented here for the SP model to the P2D model is more involved. Nevertheless, analysing the structural identifiability of the P2D model in a similar manner, by linearising all P2D model equations, would constitute an interesting area of future work. Second, frequency-domain experimental data is interesting for parameter estimation purposes because it conveys a lot of information with a relatively small dataset. Parameter identification of the SP and P2D models based on electrochemical impedance spectroscopy data could yield much more robust and faster online parameter estimation algorithms in

embedded applications as previously experienced for ECMs, *e.g.* [166]. The approach derived in this work uses linearisation to derive an approximate model transfer function; however, nonlinearities may play an important role in the model identifiability of such a complex model as the P2D model, and studying how nonlinearities may improve parameter estimation would be an interesting topic for further research.

Addressing these challenges could unlock new opportunities for electrochemical-based monitoring and control of batteries. More accurate estimation of battery states could be performed under highly dynamic and high C-rate input currents. By considering safety limits in terms of internal electrochemical battery states, rather than cell voltage and current, novel health-conscious BMSs could operate batteries closer to their limits while avoiding battery degradation [10, 12]. Furthermore, due to their physical meaning, these electrochemical models can relatively easily be improved to account for more physical phenomena, such as cell temperature distribution and degradation. The use of electrochemical models instead of ECMs in BMSs could therefore enable better battery state-of-health diagnostics and end-of-life prognostics.

Besides these prospects for embedded systems, the modelling work developed throughout this dissertation is also very useful for more general offline battery simulation applications. Specifically, the achieved gain in computational speed could prove highly valuable for 'scaling-up' the P2D model to battery pack simulations for instance, or for battery-related optimisation studies, such as battery design optimisation, or energy management optimal control in hybrid systems, including HEVs [15] or grid battery energy storage systems.

Appendix A

Modelling of degradation by SEI layer growth

A model for predicting battery capacity and power fade caused by the growth of the so-called *solid-electrolyte interphase* (SEI) in lithium-ion batteries is presented and combined to the electrochemical SP model. The irreversible formation of a SEI passivation layer on the surface of the anode material by electrolyte decomposition is believed to be one of the major degradation mechanisms in lithium-ion batteries [167]. Although the initial formation of the passivation layer is required to protect the electrolyte from further decomposition, the irreversible loss of 'cyclable' lithium due to the slow growth of the SEI layer over the battery lifetime results in cell capacity fade. The increasing thickness of the SEI layer also results in increased battery resistance and therefore power fade. The formation of the SEI results from solvent reduction, particularly ethylene carbonate (EC) reduction, due to the electrolyte instability at low potentials [45, 168]. The SEI is constituted from a variety of compounds, which can be quite complex depending on the electrolyte composition, such as lithium oxide or lithium carbonate. The SEI formed on the surface of the anode active material is electronically insulating, therefore both the lithium intercalation and solvent reduction reactions occur at the bottom of the

SEI layer at the graphite anode surface. On the one hand, the SEI material has a high ionic conductivity allowing the passage of lithium ions from the electrolyte to the anode surface. On the other hand, the large solvent molecules cannot easily diffuse through the SEI layer. The formation of new SEI compounds is therefore limited by the solvent diffusion through the SEI layer. First-principle modelling of the growth of the SEI layer and its associated cell capacity and power fade has already been discussed in the literature [45, 169], and such models can be coupled to electrochemical battery models. This appendix provides an overview of a first-principle model for the SEI layer growth similar to [45, 169]. The parameters for the SEI growth model are taken from these publications. Simulation results on the prediction of lithium-ion battery capacity and power fade are then investigated by combining the SEI growth model to the temperature-dependent SP model.

The SEI formation model consists in adding a solvent reduction side reaction to the electrochemical cell model. The rate of SEI formation can then be related to the growth rate of the SEI layer thickness and resistance. The implementation of the SEI formation model therefore requires adding and modifying some equations in the physics-based electrochemical model (SP or P2D). Similarly to the intercalation reaction, the kinetics of the solvent reduction can be described using the Butler-Volmer equation. However, by assuming that the reaction is irreversible, the simpler Tafel equation can be used instead:

$$j_{\mathrm{sr}} = -\frac{i_0}{\mathcal{F}}\sqrt{\bar{c}_{\mathrm{sol}}\bar{c}_{\mathrm{e}}\exp\left(\frac{-\mathcal{F}}{2RT}\eta_{\mathrm{sr}}\right)} \tag{A.1}$$

The dimensionless Li^+ concentration $\bar{c}_{\mathrm{e}} = c_{\mathrm{e}}/c_{\mathrm{e}}^{\mathrm{avg}}$ is assumed uniform in the SEI layer and equal to the dimensionless Li^+ concentration in the electrolyte at the surface of the SEI layer (no lithium ions diffusion gradient in the SEI). However, this side reaction kinetics is limited by the diffusion of solvent molecules through the SEI layer. By assuming a linear diffusion profile and a constant solvent concentration

in the electrolyte at the surface of the SEI layer c_{sol}^{0}, the dimensionless solvent concentration $\bar{c}_{\mathrm{sol}} = c_{\mathrm{sol}}/c_{\mathrm{sol}}^{0}$ at the bottom of the SEI layer (nearest the electrode) can be approximated by

$$\bar{c}_{\mathrm{sol}} = 1 + \frac{\delta_{\mathrm{film}}}{c_{\mathrm{sol}}^{0} D_{\mathrm{sol}}(T)} j_{\mathrm{sr}}, \tag{A.2}$$

where D_{sol} is the temperature-dependent diffusivity of the solvent in the SEI [169], and δ_{film} is the thickness of the SEI layer. The overpotential η_{sr} of the solvent reduction side reaction is defined by

$$\eta_{\mathrm{sr}} = \phi_{\mathrm{s}} - \phi_{\mathrm{e}} - U_{\mathrm{sr}}^{\mathrm{eq}} - j_{\mathrm{tot}} \mathcal{F} R_{\mathrm{film}}, \tag{A.3}$$

where ϕ_{s} is the anode solid-phase surface potential and ϕ_{e} is the electrolyte potential. The equilibrium potential of the solvent reduction $U_{\mathrm{sr}}^{\mathrm{eq}}$ is assumed constant and equal to 0.4 V [45], which means that SEI products are formed when the anode potential is lower than 0.4 V relative to Li/Li^{+} potential. The last term on the right-hand side of (A.3) is the voltage drop due to the motion of Li^{+} through the SEI layer. The global reaction rate j_{tot} is equal to the sum of the intercalation and solvent reduction reaction rates $j_{\mathrm{tot}} = j + j_{\mathrm{sr}}$. It can been noted that this SEI voltage drop term must also be added to the expression of the intercalation reaction overpotential η according to:

$$\eta = \phi_{\mathrm{s}} - \phi_{\mathrm{e}} - U^{\mathrm{eq}}(x_{\mathrm{s}}^{\mathrm{surf}}) - j_{\mathrm{tot}} \mathcal{F} R_{\mathrm{film}} \tag{A.4}$$

The SEI film resistance R_{film} is proportional to the thickness of the SEI layer δ_{film} and inversely proportional to the Li^{+} ionic conductivity of the solvent reduction products κ_{p} according to

$$R_{\mathrm{film}}(t) = \frac{\delta_{\mathrm{film}}(t)}{\kappa_{\mathrm{p}}}. \tag{A.5}$$

The rate of increase of the SEI layer thickness is directly proportional to the solvent reduction reaction rate j_{sr} according to,

$$\frac{d\delta_{\mathrm{film}}}{dt} = -\frac{j_{\mathrm{sr}} M_{\mathrm{p}}}{\rho_{\mathrm{p}}} \tag{A.6}$$

where M_{p} and ρ_{p} are respectively the molar mass and the density of the solvent reduction products.

The SEI layer growth model is coupled to the SP model in order to predict the capacity and power fade of the battery for a large number of cycles. The parameters for the electrochemical model are given in Table 3.1. The cycle considered in this study consists of a constant-current discharge step until the cut-off voltage of 3.5 V is reached, a 1000 s rest interval, a constant-current charge step until the upper voltage limit of 4.25 V is reached and another 1000 s rest interval before starting a new cycle. Figure A.1 shows the cell voltage predicted by the model during $1C$ discharge/charge cycles at 30 °C at several cycle numbers ranging from cycle 1 to cycle 5000. It is clear that the cell capacity is gradually reduced over time since the cut-off voltage is reached in shorter times with increasing number of cycles. It can also be noted that the resistance of the cell increases as indicated by the increasing voltage drop over cycles during cell discharge. Although the chosen C-rate is $1C$, it appears that the cell is discharged in far less than 3600 s even at cycle 1. This is due to the fact that (for simplicity) no constant-voltage step is included in the cycling and therefore the battery is never fully charged at the end of the cycle.

Figure A.2 shows the effect of the charge/discharge C-rate on the capacity loss of the cell. The first graph shows the capacity loss against number of cycles at $C/2$, $1C$ and $2C$. Surprisingly, the lower the C-rate the more capacity is lost according to the model for the same number of cycles (similar results are reported in the literature [45, 169]). This is due to the fact that cycling the cell at $2C$ is

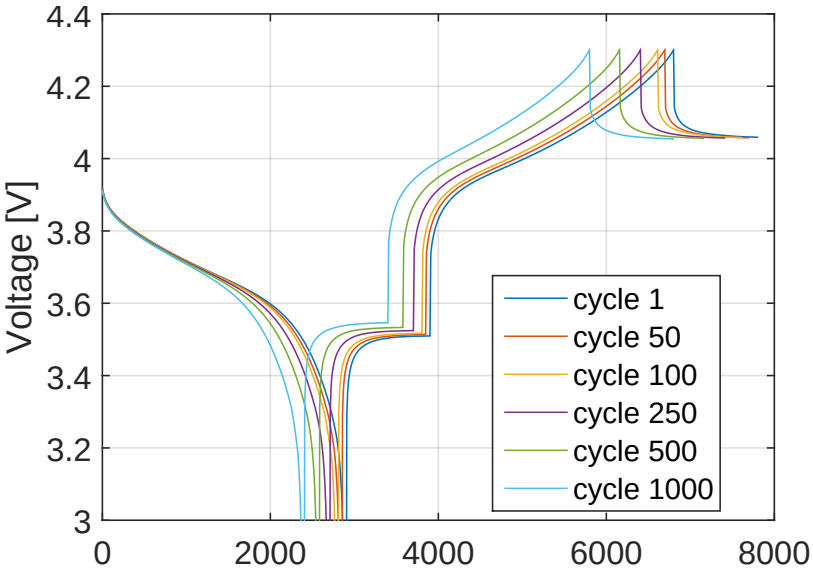

Fig. A.1 Voltage predicted by the model under $1\,C$ discharge/charge cycling at various cycles ranging from cycle 1 to 5000.

about four times faster than at $C/2$. The second graph shows the same capacity loss but plotted against time. The SEI formation mainly depends on time and C-rate does not have a large influence on the solvent reduction reaction according to the model. These results are discussed further subsequently. However, this simple model is already able to predict the $\sqrt{t}$ law of capacity loss that has been previously observed and reported in the literature [45, 169, 168].

These preliminary results suggest that the energy throughput in A h may be a better measure for degradation because it combines both the operating time and C-rate. Figure A.3 shows the capacity loss against energy throughput for different voltage operating windows. This graph reveals that capacity fade is faster when the cell is operated in a high voltage window (between 4.3 V and 3.6 V) compared to a low voltage window (between 4.0 V and 2.0 V). This confirms that low anode potentials associated with high SoCs are detrimental to lithium-ion cells and results in accelerated aging by SEI growth.

The small impact of C-rate on capacity fade is counter-intuitive since it is commonly believed that higher C-rates result in increased battery degradation. Firstly, the parameters used for the model such as the solvent reduction reaction

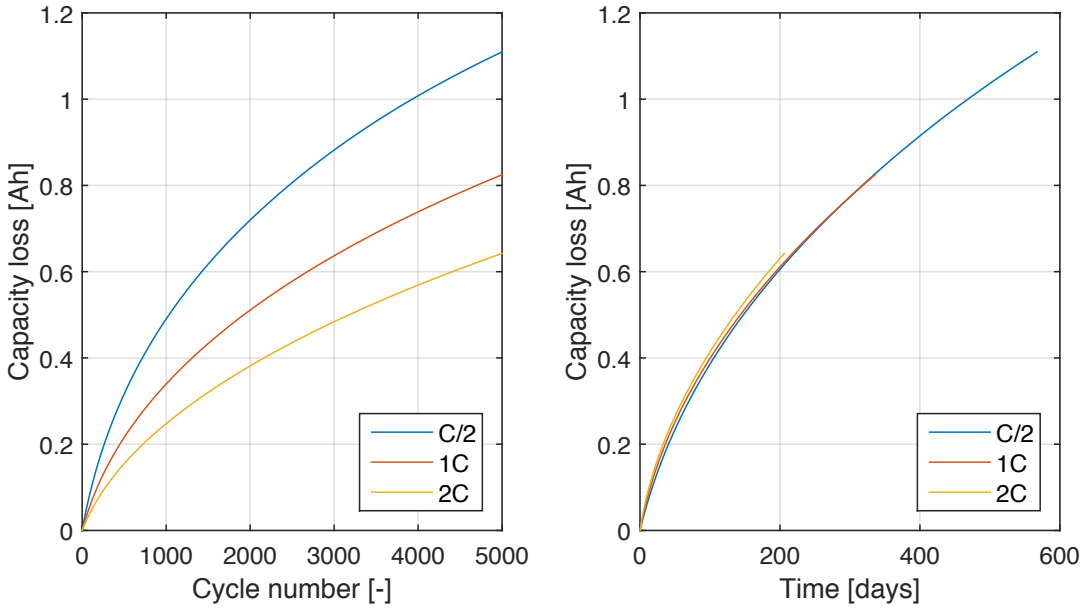

Fig. A.2 Capacity loss at different C-rates as a function of cycle number (left) and time (right).

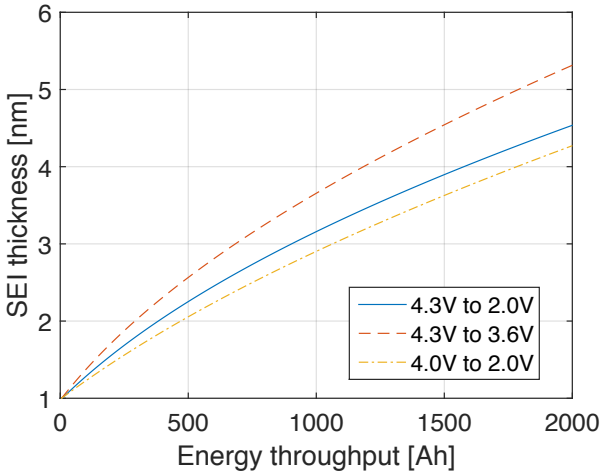

Fig. A.3 Effect of operating voltage window on SEI formation.

kinetics may be unrealistic and parameter estimation based on real aging data should be used to test the model. Secondly, the formation of the SEI layer is only one of several degradation mechanisms [170], and additional models need to be included to account for other degradation mechanisms, such as stress-induced cracking of electrode material for example [171]. Further investigations are therefore required to confirm these results using the P2D model and experimental data at higher C-rates.

Because the bulk thermal model presented in Section 2.3.2 is coupled to the SP model, temperature effects on SEI growth can also be investigated. Figure A.4 shows the predicted evolution of SEI layer thickness and capacity loss *vs.* cycle number for a cell cycled at 15 °C, 30 °C and 60 °C under $C/2$ constant current with 1000 s rest intervals between each charge and discharge. As reported in the literature [90], the SEI layer formation and the associated cell capacity loss are significantly increased at elevated temperatures due to the temperature-dependency of the solvent diffusivity D_{sol} in the SEI layer. As the temperature increases, diffusivity also increases allowing more solvent molecules to reach the bottom of the SEI layer where these are reduced into products that form the SEI.

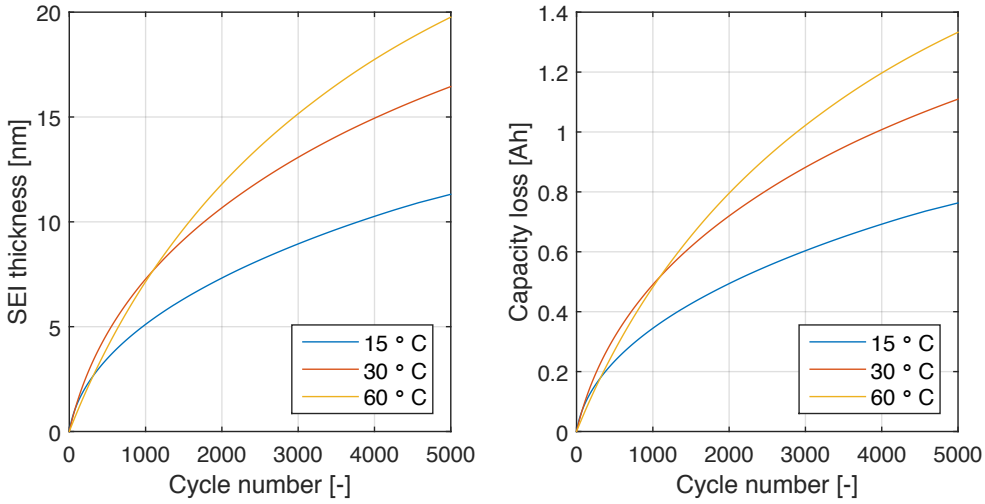

Fig. A.4 Evolution of the SEI layer thickness and capacity loss with cycle number at 15 °C, 30 °C and 60 °C.

These results show that the implementation of a credible additional model for degradation within a physics-based model such as the SP or the P2D model is relatively straightforward compared to a fully empirical approach, and can provide valuable information for cell degradation diagnostics and prognostics.

Appendix B

Discretisation of the spherical diffusion equation using symmetry

This appendix presents a slightly different method to discretising the BVP (2.3)–(2.4)–(2.5) constituting the solid-phase spherical diffusion model compared to the one introduced in Section 3.2.2. In Section 3.2.2, the discretisation using Chebyshev orthogonal collocation requires rescaling the domain $r \in [0, R_\mathrm{s}]$ on $[-1, 1]$; this results in discretisation nodes clustered at both the surface and centre of the particles. A higher density of nodes is more sensible at the surface than the centre of particles because the concentration gradient is sharp at the surface, but relatively small at the centre. Instead, by introducing $\bar{r} = r/R_\mathrm{s}$ and solving the model on the domain $r \in [-R_\mathrm{s}, R_\mathrm{s}]$ mapped onto $\bar{r} \in [-1, 1]$, the Chebyshev nodes are only clustered at the surface, and by symmetry we only need to solve the equation on $\bar{r} \in [0, 1]$, *i.e.* $r \in [0, R_\mathrm{s}]$. Introducing this change of coordinates in the BVP (3.16)–(3.17)–(3.18) reformulated with the change of variable $u_\mathrm{s} = \bar{r} c_\mathrm{s}$

results in the following PDE for the spherical diffusion

$$\frac{\partial u_\mathrm{s}}{\partial t} = \frac{D_\mathrm{s}}{R_\mathrm{s}^2}\frac{\partial^2 u_\mathrm{s}}{\partial \bar{r}^2}, \tag{B.1}$$

subject to

$$\left.\frac{\partial u_\mathrm{s}}{\partial \bar{r}}\right|_{\bar{r}=1} - u_\mathrm{s}(1) = \frac{-R_\mathrm{s}^2}{D_\mathrm{s}} j \tag{B.2}$$

By symmetry, we have that $c_\mathrm{s}(r) = c_\mathrm{s}(-r) \Leftrightarrow u_\mathrm{s}(r) = -u_\mathrm{s}(-r)$, or equivalently $u_\mathrm{s}(\bar{r}) = -u_\mathrm{s}(-\bar{r})$. We must also ensure that $c_\mathrm{s} = u_\mathrm{s}/\bar{r}$ remains finite as $\bar{r} \to 0$, therefore it follows that $u_\mathrm{s}(\bar{r} = 0) = 0$. Using the same notation conventions as Section 3.2, the discrete approximation to the diffusion equation can therefore be written

$$\frac{\partial \mathbf{u}}{\partial t} = \frac{D_\mathrm{s}}{R_\mathrm{s}^2}\mathrm{D}''_M \mathbf{u}, \tag{B.3}$$

with D''_M the second-derivative Chebyshev differentiation matrix. We define $M = 2N$ with $N \in \mathbb{N}$ so that $N + 1$ Chebyshev collocation nodes discretise half of the sphere, including the surface and centre. By recalling the symmetry condition $u_\mathrm{s}(\bar{r}) = -u_\mathrm{s}(-\bar{r})$ and that $u_\mathrm{s}(\bar{r} = 0) = 0 \Leftrightarrow \mathbf{u}_{N+1} = 0$, the discrete diffusion equation for the first half of the collocation nodes only $\mathbf{u}_{1:N}$ on $\bar{r} \in [0, 1]$ is given by

$$\frac{\partial \mathbf{u}_{1:N}}{\partial t} = \frac{D_\mathrm{s}}{R_\mathrm{s}^2}\left([\mathrm{D}''_M]_{1:N,1:N}\,\mathbf{u}_{1:N} + [\mathrm{D}''_M]_{1:N,N+2:M+1}\,\mathbf{u}_{N+2:M+1}\right). \tag{B.4}$$

Additionally, the discrete equivalent to the symmetry condition is given by

$$u_\mathrm{s}(\bar{r}) = -u_\mathrm{s}(-\bar{r}) \Rightarrow \mathbf{u}_{N+2:M+1} = -\mathrm{P}\mathbf{u}_{1:N}, \tag{B.5}$$

where the permutation matrix $\mathrm{P} = \mathrm{P}^{-1}$ is the backward-identity matrix, or exchange matrix, *i.e.* a matrix with 1's on the counter-diagonal and 0's everywhere else.

Therefore, we can write the diffusion equation in terms of $\mathbf{u}_{1:N}$ only:

$$\frac{\partial \mathbf{u}_{1:N}}{\partial t} = \frac{D_\mathrm{s}}{R_\mathrm{s}^2}\left(\left[\mathrm{D}''_M\right]_{1:N,1:N} - \left[\mathrm{D}''_M\right]_{1:N,N+2:M+1}\mathrm{P}\right)\mathbf{u}_{1:N} \tag{B.6}$$

For convenience, we define the matrices

$$\tilde{\mathrm{D}}''_N = \left[\mathrm{D}''_M\right]_{1:N,1:N} - \left[\mathrm{D}''_M\right]_{1:N,N+2:M+1}\mathrm{P} \tag{B.7}$$

and

$$\tilde{\mathrm{D}}''_N = \left[\mathrm{D}''_M\right]_{1:N,1:N} - \left[\mathrm{D}''_M\right]_{1:N,N+2:M+1}\mathrm{P}. \tag{B.8}$$

The diffusion equation further simplifies to

$$\frac{\partial \mathbf{u}_{1:N}}{\partial t} = \frac{D_\mathrm{s}}{R_\mathrm{s}^2}\tilde{\mathrm{D}}''_N\mathbf{u}_{1:N}. \tag{B.9}$$

Similarly, the discrete approximation to the boundary condition at the particle surface $r = R \Leftrightarrow \bar{r} = 1$ is given by

$$\left[\tilde{\mathrm{D}}'_N\right]_{1,:}\mathbf{u}_{1:N} - \mathbf{u}_1 = \frac{-R_\mathrm{s}^2}{D_\mathrm{s}}j, \tag{B.10}$$

or equivalently

$$\left[\tilde{\mathrm{D}}'_N\right]_{1,2:N}\mathbf{u}_{2:N} + \left(\left[\tilde{\mathrm{D}}'_N\right]_{1,1} - 1\right)\mathbf{u}_1 = \frac{R_\mathrm{s}^2}{D_\mathrm{s}}j. \tag{B.11}$$

This allows expressing the value of u_s at the surface $\mathbf{u}_1$ in terms of the value of u_s at the other nodes $\mathbf{u}_{2:N}$ as

$$\mathbf{u}_1 = \frac{\left[\tilde{\mathrm{D}}'_N\right]_{1,2:N}}{1 - \left[\tilde{\mathrm{D}}'_N\right]_{1,1}}\mathbf{u}_{2:N} + \frac{1}{1 - \left[\tilde{\mathrm{D}}'_N\right]_{1,1}}\frac{R_\mathrm{s}^2}{D_\mathrm{s}}j. \tag{B.12}$$

We now substitute the expression of $\mathbf{u}_1$ into the diffusion equation for $\mathbf{u}_{1:N}$ to obtain the following reduced diffusion equation for the inner nodes only $\mathbf{u}_{2:N}$,

which automatically satisfies the surface boundary condition:

$$\frac{\partial \mathbf{u}_{2:N}}{\partial t} = \frac{D_\mathrm{s}}{R_\mathrm{s}^2}\left(\left[\tilde{\mathrm{D}}''_N\right]_{2:N,2:N} + \frac{\left[\tilde{\mathrm{D}}''_N\right]_{2:N,1}\left[\tilde{\mathrm{D}}'_N\right]_{1,2:N}}{1-\left[\tilde{\mathrm{D}}'_N\right]_{1,1}}\right)\mathbf{u}_{2:N} + \frac{\left[\tilde{\mathrm{D}}''_N\right]_{2:N,1}}{1-\left[\tilde{\mathrm{D}}'_N\right]_{1,1}} j \tag{B.13}$$

This diffusion equation can be cast into the following state-space form:

$$\frac{\partial \mathbf{u}_{2:N}}{\partial t} = \mathrm{A}\mathbf{u}_{2:N} + \mathrm{B}j \tag{B.14}$$

$$\mathbf{c}_{2:N+1} = \mathrm{C}\mathbf{u}_{2:N} + \mathrm{D}\,j \tag{B.15}$$

where $\mathbf{c}$ is the vector containing the lithium concentration values at the Chebyshev nodes, and

$$\mathrm{A} = \frac{D_\mathrm{s}}{R_\mathrm{s}^2}\left(\left[\tilde{\mathrm{D}}''_N\right]_{2:N,2:N} + \frac{\left[\tilde{\mathrm{D}}''_N\right]_{2:N,1}\left[\tilde{\mathrm{D}}'_N\right]_{1,2:N}}{1-\left[\tilde{\mathrm{D}}'_N\right]_{1,1}}\right) \tag{B.16}$$

$$\mathrm{B} = \frac{\left[\tilde{\mathrm{D}}''_N\right]_{2:N,1}}{1-\left[\tilde{\mathrm{D}}'_N\right]_{1,1}} \tag{B.17}$$

$$\mathrm{C} = \frac{1}{R_\mathrm{s}}\frac{\left[\tilde{\mathrm{D}}'_N\right]_{1,2:N}}{1-\left[\tilde{\mathrm{D}}'_N\right]_{1,1}} \tag{B.18}$$

$$\mathrm{D} = \frac{R_\mathrm{s}}{D_\mathrm{s}}\frac{1}{1-\left[\tilde{D}^1_N\right]_{1,1}} \tag{B.19}$$

The values of concentration at the centre of the particle $\mathbf{c}_{N+1}$ can be computed by recalling the original boundary condition:

$$\left.\frac{\partial c}{\partial \bar{r}}\right|_{\bar{r}=1} = \frac{-R_\mathrm{s}}{D_\mathrm{s}} j \tag{B.20}$$

Recalling $c_\mathrm{s}(\bar{r}) = c_\mathrm{s}(-\bar{r})$, this boundary condition can be written in its discrete form:

$$\left(\left[\mathrm{D}'_M\right]_{1,1:N} + \left[\mathrm{D}'_M\right]_{1,N+2:M+1}\mathrm{P}\right)\mathbf{c}_{1:N} + \left[\mathrm{D}'_M\right]_{1,N+1}\mathbf{c}_{N+1} = \frac{-R_\mathrm{s}}{D_\mathrm{s}} j \tag{B.21}$$

which gives the expression for the concentration at the centre of the particle:

$$\mathbf{c}_{N+1} = -\frac{\left[\mathrm{D}'_M\right]_{1,1:N} + \left[D'_M\right]_{1,N+2:M+1}\mathrm{P}}{\left[\mathrm{D}'_M\right]_{1,N+1}}\mathbf{c}_{1:N} - \frac{1}{\left[\mathrm{D}'_M\right]_{1,N+1}}\frac{R_\mathrm{s}}{D_\mathrm{s}}j \tag{B.22}$$

References

[1] D. A. Howey, S. R. Duncan, and A. M. Bizeray, "Advanced battery management systems using fast electrochemical modelling," in *Hybrid and Electric Vehicles Conference IET 2013 (HEVC 2013)*, (London), Institution of Engineering and Technology, 2013.

[2] A. Bizeray, S. Zhao, S. Duncan, and D. Howey, "Lithium-ion battery thermal-electrochemical model-based state estimation using orthogonal collocation and a modified extended Kalman filter," *Journal of Power Sources*, vol. 296, pp. 400–412, 2015.

[3] S. Zhao, A. M. Bizeray, S. R. Duncan, and D. A. Howey, "Performance evaluation of an extended Kalman filter for state estimation of a pseudo-2D thermal-electrochemical lithium-ion battery model," in *Proceedings of the ASME 2015 Dynamic Systems and Control Conference*, (Colombus, Ohio), pp. 1–5, 2015.

[4] A. M. Bizeray, D. A. Howey, and C. W. Monroe, "Resolving a Discrepancy in Diffusion Potentials , with a Case Study for Li-Ion Batteries," *Journal of The Electrochemical Society*, vol. 163, no. 8, pp. E223–E229, 2016.

[5] A. M. Bizeray, J.-H. Kim, S. R. Duncan, and D. A. Howey, "Identifiability and parameter estimation of the single particle li-ion battery model." In preparation.

[6] B. Nykvist and M. Nilsson, "Rapidly falling costs of battery packs for electric vehicles," *Nature Climate Change*, vol. 5, no. 4, pp. 329–332, 2015.

[7] B. Dunn, H. Kamath, and J.-M. Tarascon, "Electrical Energy Storage for the Grid: A Battery of Choices," *Science*, vol. 334, no. 6058, pp. 928–935, 2011.

[8] M. T. Lawder, B. Suthar, P. W. C. Northrop, S. De, C. M. Hoff, O. Leitermann, M. L. Crow, S. Santhanagopalan, and V. R. Subramanian, "Battery Energy Storage System (BESS) and Battery Management System (BMS) for Grid-Scale Applications," *Proceedings of the IEEE*, vol. 102, 2014.

[9] D. A. Howey and S. M. Alavi, "Rechargeable battery energy storage system design," in *Handbook of Clean Energy Systems, vol. 5*, Wiley, 2015.

[10] N. A. Chaturvedi, R. Klein, J. Christensen, J. Ahmed, and A. Kojic, "Algorithms for advanced battery-management systems," *IEEE Control Systems Magazine*, vol. 30, no. 3, pp. 49–68, 2010.

[11] R. Klein, N. A. Chaturvedi, J. Christensen, J. Ahmed, R. Findeisen, and A. Kojic, "Optimal Charging Strategies in Lithium-Ion Battery," in *American Control Conference (ACC), 2011*, pp. 382–387, 2011.

[12] S. J. Moura, N. A. Chaturvedi, and M. Krstic, "Constraint Management in Li-ion Batteries : A Modified Reference Governor Approach," in *American Control Conference (ACC), 2013*, (Washington, DC), pp. 5332–5337, 2013.

[13] H. Perez, N. Shahmohammadhamedani, and S. Moura, "Enhanced Performance of Li-Ion Batteries via Modified Reference Governors and Electrochemical Models," *IEEE/ASME Transactions on Mechatronics*, pp. 1–10, 2014.

[14] B. Suthar, P. W. C. Northrop, R. D. Braatz, and V. R. Subramanian, "Optimal Charging Profiles with Minimal Intercalation-Induced Stresses for Lithium-Ion Batteries Using Reformulated Pseudo 2-Dimensional Models," *Journal of the Electrochemical Society*, vol. 161, no. 11, pp. F3144–F3155, 2014.

[15] S. J. Moura, J. L. Stein, and H. K. Fathy, "Battery-Health Conscious Power Management in Plug-In Hybrid Electric Vehicles via Electrochemical Modeling and Stochastic Control," *IEEE Transactions on Control Systems Technology*, vol. 21, no. 3, pp. 679–694, 2013.

[16] T. Reddy, ed., *Linden's handbook of battery technologies*. McGraw Hill Professional, 4 ed., 2010.

[17] G. L. Plett, "Extended Kalman filtering for battery management systems of LiPB-based HEV battery packs - Part 3. State and parameter estimation," *Journal of Power Sources*, vol. 134, pp. 262–276, 2004.

[18] X. Hu, S. Li, and H. Peng, "A comparative study of equivalent circuit models for Li-ion batteries," *Journal of Power Sources*, vol. 198, pp. 359–367, 2012.

[19] C. Birkl and D. Howey, "Model identification and parameter estimation for $LiFePO_4$ batteries," in *Hybrid and Electric Vehicles Conference IET 2013 (HEVC 2013)*, (London), 2013.

[20] M. Verbrugge, D. Frisch, and B. Koch, "Adaptive Energy Management of Electric and Hybrid Electric Vehicles," *Journal of The Electrochemical Society*, vol. 152, no. 2, pp. A333–A342, 2005.

[21] M. Verbrugge and B. Koch, "Generalized Recursive Algorithm for Adaptive Multiparameter Regression," *Journal of The Electrochemical Society*, vol. 153, no. 1, pp. A187–A201, 2006.

[22] D. Andre, M. Meiler, K. Steiner, C. Wimmer, T. Soczka-Guth, and D. U. Sauer, "Characterization of high-power lithium-ion batteries by electrochemical impedance spectroscopy. I. Experimental investigation," *Journal of Power Sources*, vol. 196, no. 12, pp. 5334–5341, 2011.

[23] D. Andre, M. Meiler, K. Steiner, H. Walz, T. Soczka-Guth, and D. U. Sauer, "Characterization of high-power lithium-ion batteries by electrochemical impedance spectroscopy. II: Modelling," *Journal of Power Sources*, vol. 196, no. 12, pp. 5349–5356, 2011.

[24] J. Gomez, R. Nelson, E. E. Kalu, M. H. Weatherspoon, and J. P. Zheng, "Equivalent circuit model parameters of a high-power Li-ion battery: Thermal and state of charge effects," *Journal of Power Sources*, vol. 196, no. 10, pp. 4826–4831, 2011.

[25] S. M. M. Alavi, C. R. Birkl, and D. A. Howey, "Time-domain fitting of battery electrochemical impedance models," *Journal of Power Sources*, vol. 288, pp. 345–352, 2015.

[26] M. Doyle, T. F. Fuller, and J. Newman, "Modeling of Galvanostatic Charge and Discharge of the Lithium/Polymer/Insertion Cell," *Journal of The Electrochemical Society*, vol. 140, no. 6, pp. 1526–1533, 1993.

[27] M. Doyle, *Design and simulation of lithium rechargeable batteries*. PhD thesis, University of California, Berkeley Laboratory, 1995.

[28] T. F. Fuller, M. Doyle, and J. Newman, "Simulation and Optimization of the Dual Lithium Ion Insertion Cell," *Journal of The Electrochemical Society*, vol. 141, no. 1, pp. 1–10, 1994.

[29] M. Doyle and Y. Fuentes, "Computer Simulations of a Lithium-Ion Polymer Battery and Implications for Higher Capacity Next-Generation Battery Designs," *Journal of The Electrochemical Society*, vol. 150, no. 6, pp. A706–A713, 2003.

[30] J. Newman and W. Tiedemann, "Porous-electrode theory with battery applications," *AIChE Journal*, vol. 21, no. 1, pp. 25–41, 1975.

[31] J. Newman and K. E. Thomas-Alyea, *Electrochemical Systems*. Wiley & Sons, 2004.

[32] J. C. Forman, S. J. Moura, J. L. Stein, and H. K. Fathy, "Genetic identification and fisher identifiability analysis of the Doyle-Fuller-Newman model from experimental cycling of a $LiFePO_4$ cell," *Journal of Power Sources*, vol. 210, pp. 263–275, 2012.

[33] I. J. Ong and J. Newman, "Double-Layer Capacitance in a Dual Lithium Ion Insertion Cell," *Journal of The Electrochemical Society*, vol. 146, no. 12, pp. 4360–4365, 1999.

[34] M. Doyle, J. P. Meyers, and J. Newman, "Computer Simulations of the Impedance Response of Lithium Rechargeable Batteries," *Journal of The Electrochemical Society*, vol. 147, no. 1, pp. 99–110, 2000.

[35] J. P. Meyers, M. Doyle, R. M. Darling, and J. Newman, "The Impedance Response of a Porous Electrode Composed of intercalation particles," *Journal of The Electrochemical Society*, vol. 147, no. 8, pp. 2930–2940, 2000.

[36] C. R. Pals and J. Newman, "Thermal Modeling of the Lithium / Polymer Battery - I. Discharge behavior of a single cell," *Journal of The Electrochemical Society*, vol. 142, no. 10, pp. 3274–3281, 1995.

[37] C. R. Pals and J. Newman, "Thermal Modeling of the Lithium / Polymer Battery - II. Temperature profiles in cell stack," *Journal of The Electrochemical Society*, vol. 142, no. 10, pp. 3282–3288, 1995.

[38] G. G. Botte, B. A. Johnson, and R. E. White, "Influence of Some Design Variables on the Thermal Behavior of a Lithium-Ion Cell," *Journal of The Electrochemical Society*, vol. 146, no. 3, pp. 914–923, 1999.

[39] W. B. Gu and C. Y. Wang, "Thermal-Electrochemical Modeling of Battery Systems," *Journal of The Electrochemical Society*, vol. 147, no. 8, pp. 2910–2922, 2000.

[40] L. Song and J. W. Evans, "Electrochemical-Thermal Model of Lithium Polymer Batteries," *Journal of The Electrochemical Society*, vol. 147, no. 6, pp. 2086–2095, 2000.

[41] P. M. Gomadam, J. W. Weidner, R. A. Dougal, and R. E. White, "Mathematical modeling of lithium-ion and nickel battery systems," *Journal of Power Sources*, vol. 110, no. 2, pp. 267–284, 2002.

[42] V. Srinivasan and C. Y. Wang, "Analysis of Electrochemical and Thermal Behavior of Li-Ion Cells," *Journal of The Electrochemical Society*, vol. 150, no. 1, pp. A98–A106, 2003.

[43] G.-H. Kim, K. Smith, K.-J. Lee, S. Santhanagopalan, and A. Pesaran, "Multi-Domain Modeling of Lithium-Ion Batteries Encompassing Multi-Physics in Varied Length Scales," *Journal of The Electrochemical Society*, vol. 158, no. 8, pp. A955–A969, 2011.

[44] R. Darling and J. Newman, "Modeling Side Reactions in Composite $LiMn_2O_4$ Electrodes," *Journal of The Electrochemical Society*, vol. 145, no. 3, pp. 990–998, 1998.

[45] P. Ramadass, B. Haran, P. M. Gomadam, R. White, and B. N. Popov, "Development of First Principles Capacity Fade Model for Li-Ion Cells," *Journal of The Electrochemical Society*, vol. 151, no. 2, pp. A196–A203, 2004.

[46] A. V. Randall, R. D. Perkins, X. Zhang, and G. L. Plett, "Controls oriented reduced order modeling of solid-electrolyte interphase layer growth," *Journal of Power Sources*, vol. 209, pp. 282–288, 2012.

[47] S. Atlung, K. West, and T. Jacobsen, "Dynamic aspects of solid solution cathodes for electrochemical power sources," *Journal of The Electrochemical Society*, vol. 126, no. 8, pp. 1311–1321, 1979.

[48] G. Ning and B. N. Popov, "Cycle Life Modeling of Lithium-Ion Batteries," *Journal of The Electrochemical Society*, vol. 151, no. 10, pp. A1584–A1591, 2004.

[49] S. Santhanagopalan and R. E. White, "Online estimation of the state of charge of a lithium ion cell," *Journal of Power Sources*, vol. 161, no. 2, pp. 1346–1355, 2006.

[50] S. J. Moura, N. A. Chaturvedi, and M. Krstić, "Adaptive Partial Differential Equation Observer for Battery State-of-Charge/State-of-Health Estimation Via an Electrochemical Model," *Journal of Dynamic Systems, Measurement, and Control*, vol. 136, no. 1, 2013.

[51] D. Di Domenico, A. Stefanopoulou, and G. Fiengo, "Lithium-Ion Battery State of Charge and Critical Surface Charge Estimation Using an Electrochemical Model-Based Extended Kalman Filter," *Journal of Dynamic Systems, Measurement, and Control*, vol. 132, no. 6, 2010.

[52] K. Smith, C. D. Rahn, and C.-Y. Wang, "Model-based electrochemical estimation of lithium-ion batteries," in *2008 IEEE International Conference on Control Applications*, no. 1, (San Antonio, Texas), pp. 714–719, 2008.

[53] K. Smith, C. D. Rahn, and C.-Y. Wang, "Model-Based Electrochemical Estimation and Constraint Management for Pulse Operation of Lithium Ion Batteries," *IEEE Transactions on Control Systems Technology*, vol. 18, pp. 654–663, may 2010.

[54] K. Smith, C. D. Rahn, and C.-Y. Wang, "Control oriented 1D electrochemical model of lithium ion battery," *Energy Conversion and Management*, vol. 48, no. 9, pp. 2565–2578, 2007.

[55] K. Smith, C. D. Rahn, and C.-Y. Wang, "Model Order Reduction of 1D Diffusion Systems Via Residue Grouping," *Journal of Dynamic Systems, Measurement, and Control*, vol. 130, no. 1, 2008.

[56] K. D. Stetzel, L. L. Aldrich, M. S. Trimboli, and G. L. Plett, "Electrochemical state and internal variables estimation using a reduced-order physics-based model of a lithium-ion cell and an extended Kalman filter," *Journal of Power Sources*, vol. 278, pp. 490–505, 2015.

[57] J. L. Lee, A. Chemistruck, and G. L. Plett, "One-dimensional physics-based reduced-order model of lithium-ion dynamics," *Journal of Power Sources*, vol. 220, pp. 430–448, 2012.

[58] J. L. Lee, A. Chemistruck, and G. L. Plett, "Discrete-time realization of transcendental impedance models, with application to modeling spherical solid diffusion," *Journal of Power Sources*, vol. 206, pp. 367–377, 2012.

[59] J. L. Lee, L. L. Aldrich, K. D. Stetzel, and G. L. Plett, "Extended operating range for reduced-order model of lithium-ion cells," *Journal of Power Sources*, vol. 255, pp. 85–100, 2014.

[60] T.-S. Dao, C. P. Vyasarayani, and J. McPhee, "Simplification and order reduction of lithium-ion battery model based on porous-electrode theory," *Journal of Power Sources*, vol. 198, pp. 329–337, 2012.

[61] L. Cai and R. E. White, "Lithium ion cell modeling using orthogonal collocation on finite elements," *Journal of Power Sources*, vol. 217, pp. 248–255, 2012.

[62] P. W. C. Northrop, V. Ramadesigan, S. De, and V. R. Subramanian, "Coordinate Transformation, Orthogonal Collocation, Model Reformulation and Simulation of Electrochemical-Thermal Behavior of Lithium-Ion Battery Stacks," *Journal of The Electrochemical Society*, vol. 158, no. 12, pp. A1461–A1477, 2011.

[63] B. Suthar, V. Ramadesigan, P. W. C. Northrop, B. Gopaluni, S. Santhanagopalan, R. D. Braatz, and V. R. Subramanian, "Optimal Control and State Estimation of Lithium-ion Batteries Using Reformulated Models," in *American Control Conference (ACC), 2013*, (Washington DC), pp. 5350–5355, 2013.

[64] R. B. Gopaluni and R. D. Braatz, "State of Charge Estimation in Li-Ion Batteries Using an Isothermal Pseudo Two-Dimensional Model," in *Proceedings of the 10th IFAC International Symposium on Dynamics and Control of Process System* (H. Michael, ed.), (Mumbai, India), pp. 135–140, 2013.

[65] V. R. Subramanian, V. D. Diwakar, and D. Tapriyal, "Efficient Macro-Micro Scale Coupled Modeling of Batteries," *Journal of The Electrochemical Society*, vol. 152, no. 10, pp. A2002–A2008, 2005.

[66] S. Jiang, "A Parameter Identification Method for a Battery Equivalent Circuit Model," in *SAE Technical Paper*, no. 2310, pp. 1–9, 2011.

[67] R. A. Nazer, V. Cattin, P. Granjon, and M. Montaru, "A new optimization algorithm for a li-ion battery equivalent electrical equivalent circuit identification.," in *9th International Conference of Modeling, Optimization and Simulation - MOSIM'12*, (Bordeaux, France), 2012.

[68] J. Jang and J. Yoo, "Equivalent circuit evaluation method of lithium polymer battery using Bode plot and numerical analysis," *IEEE Transactions on Energy Conversion*, vol. 26, no. 1, pp. 290–298, 2011.

[69] N. Moubayed, J. Kouta, A. El-Ali, H. Dernayka, and R. Outbib, "Parameter identification of the lead-acid battery model," in *2008 33rd IEEE Photovoltaic Specialists Conference*, pp. 1–6, 2008.

[70] S. Santhanagopalan, Q. Guo, and R. E. White, "Parameter Estimation and Model Discrimination for a Lithium-Ion Cell," *Journal of The Electrochemical Society*, vol. 154, no. 3, pp. A198–A206, 2007.

[71] L. Ljung, *System Identification: Theory for the User*. Pearson Education, 1998.

[72] S. Santhanagopalan, Q. Zhang, K. Kumaresan, and R. E. White, "Parameter Estimation and Life Modeling of Lithium-Ion Cells," *Journal of The Electrochemical Society*, vol. 155, no. 4, pp. A345–A353, 2008.

[73] C. Speltino, D. D. Domenico, G. Fiengo, and A. Stefanopoulou, "Experimental identification and validation of an electrochemical model of a Lithium-Ion Battery," in *2009 IEEE European Control Conference*, (Budapest, Hungary), pp. 1053–1058, 2009.

[74] V. Ramadesigan, V. Boovaragavan, M. Arabandi, K. Chen, H. Tsukamoto, R. Braatz, and V. Subramanian, "Parameter Estimation and Capacity Fade Analysis of Lithium-Ion Batteries Using First-Principles-Based Efficient Reformulated Models," in *ECS Transactions*, vol. 19, pp. 11–19, 2009.

[75] V. Ramadesigan, K. Chen, N. A. Burns, V. Boovaragavan, R. D. Braatz, and V. R. Subramanian, "Parameter Estimation and Capacity Fade Analysis of Lithium-Ion Batteries Using Reformulated Models," *Journal of The Electrochemical Society*, vol. 158, no. 9, pp. A1048–A1054, 2011.

[76] J. C. Forman, S. J. Moura, J. L. Stein, and H. K. Fathy, "Genetic parameter identification of the Doyle-Fuller-Newman model from experimental cycling of a $LiFePO_4$ battery," in *Proceedings of the 2011 American Control Conference*, (San Francisco, CA, USA), pp. 362–369, 2011.

[77] R. Masoudi, T. Uchida, and J. McPhee, "Parameter estimation of an electrochemistry-based lithium-ion battery model," *Journal of Power Sources*, vol. 291, pp. 215–224, 2015.

[78] M. A. Rahman, S. Anwar, and A. Izadian, "Electrochemical model parameter identification of a lithium-ion battery using particle swarm optimization method," *Journal of Power Sources*, vol. 307, pp. 86–97, 2016.

[79] L. Zhang, L. Wang, G. Hinds, C. Lyu, J. Zheng, and J. Li, "Multi-objective optimization of lithium-ion battery model using genetic algorithm approach," *Journal of Power Sources*, vol. 270, pp. 367–378, 2014.

[80] J. Vazquez-Arenas, L. E. Gimenez, M. Fowler, T. Han, and S.-K. Chen, "A rapid estimation and sensitivity analysis of parameters describing the behavior of commercial Li-ion batteries including thermal analysis," *Energy Conversion and Management*, vol. 87, pp. 472–482, 2014.

[81] J. Marcicki, M. Canova, A. T. Conlisk, and G. Rizzoni, "Design and parametrization analysis of a reduced-order electrochemical model of graphite/$LiFePO_4$ cells for SOC/SOH estimation," *Journal of Power Sources*, vol. 237, pp. 310–324, 2013.

[82] A. P. Schmidt, M. Bitzer, Á. W. Imre, and L. Guzzella, "Experiment-driven electrochemical modeling and systematic parameterization for a lithium-ion battery cell," *Journal of Power Sources*, vol. 195, no. 15, pp. 5071–5080, 2010.

[83] A. Jokar, B. Rajabloo, M. Désilets, and M. Lacroix, "An Inverse Method for Estimating the Electrochemical Parameters of Lithium-Ion Batteries - I. Methodology," *Journal of The Electrochemical Society*, vol. 163, no. 14, pp. A2876–A2886, 2016.

[84] B. Rajabloo, A. Jokar, M. Désilets, and M. Lacroix, "An Inverse Method for Estimating the Electrochemical Parameters of Lithium-Ion Batteries - II: Implementation," *Journal of The Electrochemical Society*, vol. 163, no. 14, pp. A2876–A2886, 2016.

[85] D. C. López C, G. Wozny, A. Flores-Tlacuahuac, R. Vasquez-Medrano, and V. M. Zavala, "A Computational Framework for Identifiability and Ill-Conditioning Analysis of Lithium-Ion Battery Models," *Industrial & Engineering Chemistry Research*, vol. 55, no. 11, pp. 3026–3042, 2016.

[86] P. W. C. Northrop, V. Ramadesigan, S. De, and V. R. Subramanian, "Coordinate Transformation, Orthogonal Collocation, Model Reformulation and Simulation of Electrochemical-Thermal Behavior of Lithium-Ion Battery Stacks," *Journal of The Electrochemical Society*, vol. 158, no. 12, p. A1461, 2011.

[87] V. R. Subramanian, J. A. Ritter, and R. E. White, "Approximate Solutions for Galvanostatic Discharge of Spherical Particles I. Constant Diffusion Coefficient," *Journal of The Electrochemical Society*, vol. 148, no. 11, pp. E444–E449, 2001.

[88] V. Ramadesigan, V. Boovaragavan, J. C. Pirkle, and V. R. Subramanian, "Efficient Reformulation of Solid-Phase Diffusion in Physics-Based Lithium-Ion Battery Models," *Journal of The Electrochemical Society*, vol. 157, no. 7, pp. A854–A860, 2010.

[89] Y. Ji, Y. Zhang, and C.-Y. Wang, "Li-Ion Cell Operation at Low Temperatures," *Journal of the Electrochemical Society*, vol. 160, no. 4, pp. A636–A649, 2013.

[90] J. Wang, P. Liu, J. Hicks-Garner, E. Sherman, S. Soukiazian, M. Verbrugge, H. Tataria, J. Musser, and P. Finamore, "Cycle-life model for graphite-$LiFePO_4$ cells," *Journal of Power Sources*, vol. 196, no. 8, pp. 3942–3948, 2011.

[91] D.-W. Chung, M. Ebner, D. R. Ely, V. Wood, and R. Edwin García, "Validity of the Bruggeman relation for porous electrodes," *Modelling and Simulation in Materials Science and Engineering*, vol. 21, 2013.

[92] L. O. Valoen and J. N. Reimers, "Transport Properties of $LiPF_6$-Based Li-Ion Battery Electrolytes," *Journal of The Electrochemical Society*, vol. 152, no. 5, pp. A882–A891, 2005.

[93] V. Ramadesigan, P. W. C. Northrop, S. De, S. Santhanagopalan, R. D. Braatz, and V. R. Subramanian, "Modeling and Simulation of Lithium-Ion Batteries from a Systems Engineering Perspective," *Journal of The Electrochemical Society*, vol. 159, no. 3, pp. R31–R45, 2012.

[94] E. McTurk, C. R. Birkl, M. R. Roberts, D. A. Howey, and P. G. Bruce, "Minimally Invasive Insertion of Reference Electrodes into Commercial Lithium-Ion Pouch Cells," *ECS Electrochemistry Letters*, vol. 4, no. 12, pp. A145–A147, 2015.

[95] Q. Guo and R. E. White, "Cubic Spline Regression for the Open-Circuit Potential Curves of a Lithium-Ion Battery," *Journal of The Electrochemical Society*, vol. 152, no. 2, pp. A343–A350, 2005.

[96] C. R. Birkl, E. McTurk, M. R. Roberts, P. G. Bruce, and D. A. Howey, "A Parametric Open Circuit Voltage Model for Lithium Ion Batteries," *Journal of The Electrochemical Society*, vol. 162, no. 12, pp. A2271–A2280, 2015.

[97] J. R. Dahn, T. Zheng, Y. Liu, and J. S. Xue, "Mechanisms for Lithium Insertion in Carbonaceous Materials," *Science*, vol. 270, no. 5236, pp. 590–593, 1995.

[98] A. Sleigh, J. Murray, and W. McKinnon, "Memory effects due to phase conversion and hysteresis in Li/Li_xMnO_2 cells," *Electrochimica acta*, vol. 36, no. 9, pp. 1469–1474, 1991.

[99] P. G. Bruce, A. R. Armstrong, and R. L. Gitzendanner, "New intercalation compounds for lithium batteries: layered $LiMnO_2$," *Journal of Materials Chemistry*, vol. 9, no. 1, pp. 193–198, 1999.

[100] J. Barker, R. Pynenburg, R. Koksbang, and M. Y. Saidi, "An electrochemical investigation into the lithium insertion properties of Li_xCoO_2," *Electrochimica Acta*, vol. 41, no. 15, pp. 2481–2488, 1996.

[101] W. Dreyer, J. Jamnik, C. Guhlke, R. Huth, J. Moskon, and M. Gaberscek, "The thermodynamic origin of hysteresis in insertion batteries.," *Nature materials*, vol. 9, no. 5, pp. 448–53, 2010.

[102] G. L. Plett, "Extended Kalman filtering for battery management systems of LiPB-based HEV battery packs - Part 2. Modeling and identification," *Journal of Power Sources*, vol. 134, pp. 262–276, 2004.

[103] M. Verbrugge and E. Tate, "Adaptive state of charge algorithm for nickel metal hydride batteries including hysteresis phenomena," *Journal of Power Sources*, vol. 126, no. 1-2, pp. 236–249, 2004.

[104] J. Liu and C. W. Monroe, "Solute-volume effects in electrolyte transport," *Electrochimica Acta*, vol. 135, pp. 447–460, 2014.

[105] A. M. Ramos and C. P. Please, "Some comments on the Butler-Volmer equation for modeling Lithium-ion batteries," *ArXiv e-prints*, pp. 1–14, 2015.

[106] K. Smith and C.-Y. Wang, "Power and thermal characterization of a lithium-ion battery pack for hybrid-electric vehicles," *Journal of Power Sources*, vol. 160, no. 1, pp. 662–673, 2006.

[107] K. Smith and C.-Y. Wang, "Solid-state diffusion limitations on pulse operation of a lithium ion cell for hybrid electric vehicles," *Journal of Power Sources*, vol. 161, no. 1, pp. 628–639, 2006.

[108] K. A. Smith, C. D. Rahn, and C. Y. Wang, "Control oriented 1D electrochemical model of lithium ion battery," *Energy Conversion and Management*, vol. 48, no. 9, pp. 2565–2578, 2007.

[109] G.-H. Kim, K. Smith, J. Ireland, and A. Pesaran, "Fail-safe design for large capacity lithium-ion battery systems," *Journal of Power Sources*, vol. 210, pp. 243–253, 2012.

[110] M. W. Verbrugge and P. Liu, "Microstructural Analysis and Mathematical Modeling of Electric Double-Layer Supercapacitors," *Journal of The Electrochemical Society*, vol. 152, no. 5, pp. D79–D87, 2005.

[111] G. Richardson, G. Denuault, and C. P. Please, "Multiscale modelling and analysis of lithium-ion battery charge and discharge," *Journal of Engineering Mathematics*, vol. 72, no. 1, pp. 41–72, 2012.

[112] V. R. Subramanian, V. Boovaragavan, and V. D. Diwakar, "Toward Real-Time Simulation of Physics Based Lithium-Ion Battery Models," *Electrochemical and Solid-State Letters*, vol. 10, no. 11, pp. A255–A260, 2007.

[113] B. S. Haran, B. N. Popov, and R. E. White, "Determination of the hydrogen diffusion coefficient in metal hydrides by impedance spectroscopy," *Journal of Power Sources*, vol. 75, no. 1, pp. 56–63, 1998.

[114] D. Bernardi, E. Pawlikowski, and J. Newman, "A General Energy Balance for Battery Systems," *Journal of The Electrochemical Society*, vol. 132, no. 1, 1985.

[115] Y. Chen and J. W. Evans, "Heat transfer phenomena in lithium/polymer-electrolyte batteries for electric vehicle application," *Journal of the Electrochemical Society*, vol. 140, no. 7, pp. 1833–1838, 1993.

[116] Y. Chen and J. W. Evans, "Thermal analysis of lithium polymer electrolyte batteries by a two dimensional model-thermal behaviour and design optimization," *Electrochimica Acta*, vol. 39, no. 4, pp. 517–526, 1994.

[117] Y. Chen and J. W. Evans, "Thermal Analysis of Lithium-Ion Batteries," *Journal of The Electrochemical Society*, vol. 143, no. 9, pp. 2708–2712, 1996.

[118] L. Rao and J. Newman, "Heat-Generation Rate and General Energy Balance for insertion battery systems," *Journal of The Electrochemical Society*, vol. 144, no. 8, pp. 2697–2704, 1997.

[119] B. Wu, V. Yufit, M. Marinescu, G. J. Offer, R. F. Martinez-Botas, and N. P. Brandon, "Coupled thermal-electrochemical modelling of uneven heat generation in lithium-ion battery packs," *Journal of Power Sources*, vol. 243, pp. 544–554, 2013.

[120] K. J. Lee, K. Smith, A. Pesaran, and G. H. Kim, "Three dimensional thermal-, electrical-, and electrochemical-coupled model for cylindrical wound large format lithium-ion batteries," *Journal of Power Sources*, vol. 241, pp. 20–32, 2013.

[121] F. P. Incropera, D. P. DeWitt, T. L. Bergman, and A. S. Lavine, *Fundamentals of Heat and Mass Transfer*, vol. 6th. Wiley & Sons, 2007.

[122] S. J. Drake, D. A. Wetz, J. K. Ostanek, S. P. Miller, J. M. Heinzel, and A. Jain, "Measurement of anisotropic thermophysical properties of cylindrical Li-ion cells," *Journal of Power Sources*, vol. 252, pp. 298–304, 2014.

[123] R. R. Richardson and D. A. Howey, "Sensorless Battery Internal Temperature Estimation Using a Kalman Filter with Impedance Measurement," *IEEE Transactions on Sustainable Energy*, vol. 6, no. 4, pp. 1190–1199, 2015.

[124] R. R. Richardson, S. Zhao, and D. A. Howey, "On-board monitoring of 2-D spatially-resolved temperatures in cylindrical lithium-ion batteries: Part II. State estimation via impedance-based temperature sensing," *Journal of Power Sources*, vol. 327, pp. 726–735, 2016.

[125] U. S. Kim, C. B. Shin, and C. S. Kim, "Effect of electrode configuration on the thermal behavior of a lithium-polymer battery," *Journal of Power Sources*, vol. 180, no. 2, pp. 909–916, 2008.

[126] U. S. Kim, C. B. Shin, and C. S. Kim, "Modeling for the scale-up of a lithium-ion polymer battery," *Journal of Power Sources*, vol. 189, no. 1, pp. 841–846, 2009.

[127] U. S. Kim, J. Yi, C. B. Shin, T. Han, and S. Park, "Modelling the thermal behaviour of a lithium-ion battery during charge," *Journal of Power Sources*, vol. 196, no. 11, pp. 5115–5121, 2011.

[128] J. B. Robinson, E. Engebretsen, D. P. Finegan, J. Darr, G. Hinds, P. R. Shearing, and D. J. L. Brett, "Detection of Internal Defects in Lithium-Ion Batteries Using Lock-in Thermography," *ECS Electrochemistry Letters*, vol. 4, no. 9, pp. A106–A109, 2015.

[129] K. Kumaresan, G. Sikha, and R. E. White, "Thermal Model for a Li-Ion Cell," *Journal of The Electrochemical Society*, vol. 155, no. 2, pp. A164–A171, 2008.

[130] L. Cai and R. E. White, "Mathematical modeling of a lithium ion battery with thermal effects in COMSOL Inc. Multiphysics software," *Journal of Power Sources*, vol. 196, no. 14, pp. 5985–5989, 2011.

[131] Y. Ye, Y. Shi, N. Cai, J. Lee, and X. He, "Electro-thermal modeling and experimental validation for lithium ion battery," *Journal of Power Sources*, vol. 199, pp. 227–238, 2012.

[132] M. Guo, G. Sikha, and R. E. White, "Single-Particle Model for a Lithium-Ion Cell: Thermal Behavior," *Journal of The Electrochemical Society*, vol. 158, no. 2, pp. A122–A132, 2011.

[133] O. Y. Egorkina and A. M. Skundin, "The effect of temperature on lithium intercalation into carbon materials," *Journal of Solid State Electrochemistry*, vol. 2, no. 4, pp. 216–220, 1998.

[134] D. Gottlieb and S. A. Orszag, *Numerical analysis of spectral methods: Theory and Applications*. SIAM, 1977.

[135] L. N. Trefethen, *Spectral Methods in MATLAB*. SIAM, 2000.

[136] J. A. C. Weideman and S. C. Reddy, "A MATLAB Differentiation Matrix Suite," *ACM Transactions on Mathematical Softwares*, vol. 26, no. 4, pp. 465–519, 2000.

[137] C. W. Clenshaw and A. R. Curtis, "A method for numerical integration on an automatic computer," *Numerische Mathematik*, vol. 2, no. 1, pp. 197–205, 1960.

[138] T. A. Driscoll, N. Hale, and L. N. Trefethen, *Chebfun Guide*. Oxford: Pafnuty Publications, 2014.

[139] L. Petzold, "Differential/algebraic equations are not ODE's," *SIAM Journal on Scientific and Statistical Computing*, vol. 3, no. 3, pp. 367–384, 1982.

[140] L. R. Petzold, "A description of DASSL: A differential / algebraic system solver," 1982.

[141] K. E. Brenan, S. L. Campbell, and L. R. Petzold, *Numerical Solution of Initial-Value Problems in Differential-Algebraic Equations*. Society for Industrial and Applied Mathematics, 1995.

[142] A. C. Hindmarsh, P. N. Brown, K. E. Grant, S. L. Lee, R. Serban, D. E. Shumaker, and C. S. Woodward, "SUNDIALS: Suite of Nonlinear and Differential/Algebraic Equation Solvers," *ACM Transactions on Mathematical Software*, vol. 31, no. 3, pp. 363–396, 2005.

[143] E. Hairer and G. Wanner, *Solving ordinary differential equations II: Stiff and differential-algebraic problems*. Springer, 1991.

[144] B. Wu and R. White, "An initialization subroutine for DAEs solvers: DAEIS," *Computers & Chemical Engineering*, vol. 25, no. 2-3, pp. 301–311, 2001.

[145] V. Boovaragavan and V. R. Subramanian, "A quick and efficient method for consistent initialization of battery models," *Electrochemistry Communications*, vol. 9, no. 7, pp. 1772–1777, 2007.

[146] R. N. Methekar, V. Ramadesigan, J. C. Pirkle, and V. R. Subramanian, "A perturbation approach for consistent initialization of index-1 explicit differential–algebraic equations arising from battery model simulations," *Computers & Chemical Engineering*, vol. 35, no. 11, pp. 2227–2234, 2011.

[147] L. F. Shampine, M. W. Reichelt, and J. A. Kierzenka, "Solving Index-1 DAEs in MATLAB and Simulink," *SIAM Review*, vol. 41, no. 3, pp. 538–552, 1999.

[148] F. N. Fritsch and R. E. Carlson, "Monotone Piecewise Cubic Interpolation," *SIAM Journal on Numerical Analysis*, vol. 17, no. 2, pp. 238–246, 1980.

[149] T. L. Kulova, A. M. Skundin, E. A. Nizhnikovskii, and A. V. Fesenko, "Temperature effect on the lithium diffusion rate in graphite," *Russian Journal of Electrochemistry*, vol. 42, no. 3, pp. 259–262, 2006.

[150] K. Nakamura, H. Ohno, K. Okamura, Y. Michihiro, I. Nakabayashi, and T. Kanashiro, "On the diffusion of Li+ defects in $LiCoO_2$ and $LiNiO_2$," *Solid State Ionics*, vol. 135, no. 1-4, pp. 143–147, 2000.

[151] H. Zheng, J. Qin, Y. Zhao, T. Abe, and Z. Ogumi, "Temperature dependence of the electrochemical behavior of $LiCoO_2$ in quaternary ammonium-based ionic liquid electrolyte," *Solid State Ionics*, vol. 176, no. 29-30, pp. 2219–2226, 2005.

[152] M. André, "The ARTEMIS European driving cycles for measuring car pollutant emissions," *Science of the Total Environment*, vol. 334-335, pp. 73–84, 2004.

[153] V. M. Becerra, P. D. Roberts, and G. W. Griffiths, "Applying the extended Kalman filter to systems described by nonlinear differential-algebraic equations," *Control Engineering Practice*, vol. 9, pp. 267–281, 2001.

[154] A. Gelb, J. F. Kasper, R. A. Nash, C. F. Price, and A. A. Sutherland, *Applied Optimal Estimation*. The MIT Press, 1974.

[155] P. S. Maybeck, *Stochastic Models, Estimation and Control (Vol. 1)*. Academic Press, 1979.

[156] S. Särkkä, *Bayesian filtering and smoothing*. Cambridge University Press, 2013.

[157] D. Simon, *Optimal state estimation: Kalman, H-Infinity, and Nonlinear Approaches*. Wiley-Interscience, 2006.

[158] R. Bellman and K. J. Astrom, "On structural identifiability," *Mathematical Biosciences*, vol. 7, no. 3-4, pp. 329–339, 1970.

[159] S. M. M. Alavi, A. Mahdi, S. J. Payne, and D. A. Howey, "Structural identifiability of battery equivalent circuit models," *ArXiv e-prints*, pp. 1–18, 2016.

[160] E. Barsoukov and J. R. Macdonald, *Impedance Spectroscopy*. Hoboken, NJ, USA: John Wiley & Sons, Inc., 2005.

[161] S. Buller, M. Thele, E. Karden, and R. W. De Doncker, "Impedance-based non-linear dynamic battery modeling for automotive applications," *Journal of Power Sources*, vol. 113, no. 2, pp. 422–430, 2003.

[162] D. A. Howey, P. D. Mitcheson, V. Yufit, G. J. Offer, and N. P. Brandon, "Online measurement of battery impedance using motor controller excitation," *IEEE Transactions on Vehicular Technology*, vol. 63, no. 6, pp. 2557–2566, 2014.

[163] M. Ecker, T. K. D. Tran, P. Dechent, S. Kabitz, A. Warnecke, and D. U. Sauer, "Parameterization of a Physico-Chemical Model of a Lithium-Ion Battery: I. Determination of Parameters," *Journal of the Electrochemical Society*, vol. 162, no. 9, pp. A1836–A1848, 2015.

[164] A. M. Bizeray, J. Reniers, and D. A. Howey, "Spectral_li-ion_SPM," 2016.

[165] M. T. Lawder, V. Ramadesigan, B. Suthar, and V. R. Subramanian, "Extending explicit and linearly implicit ODE solvers for index-1 DAEs," *Computers & Chemical Engineering*, vol. 82, pp. 283–292, 2015.

[166] D. A. Howey, P. D. Mitcheson, V. Yufit, G. J. Offer, and N. P. Brandon, "Online measurement of battery impedance using motor controller excitation," *IEEE Transactions on Vehicular Technology*, vol. 63, no. 6, pp. 2557–2566, 2014.

[167] D. Aurbach, E. Zinigrad, Y. Cohen, and H. Teller, "A short review of failure mechanisms of lithium metal and lithiated graphite anodes in liquid electrolyte solutions," *Solid State Ionics*, vol. 148, pp. 405–416, 2002.

[168] H. J. Ploehn, P. Ramadass, and R. E. White, "Solvent Diffusion Model for Aging of Lithium-Ion Battery Cells," *Journal of The Electrochemical Society*, vol. 151, no. 3, pp. A456–A462, 2004.

[169] M. B. Pinson and M. Z. Bazant, "Theory of SEI Formation in Rechargeable Batteries: Capacity Fade, Accelerated Aging and Lifetime Prediction," *Journal of the Electrochemical Society*, vol. 160, no. 2, pp. A243–A250, 2013.

[170] C. R. Birkl, M. R. Roberts, E. Mcturk, P. G. Bruce, and D. A. Howey, "Degradation Diagnostics for Lithium Ion Cells," *Journal of Power Sources*, vol. 341, pp. 1–35, 2016.

[171] R. Deshpande, M. Verbrugge, Y.-T. Cheng, J. Wang, and P. Liu, "Battery Cycle Life Prediction with Coupled Chemical Degradation and Fatigue Mechanics," *Journal of the Electrochemical Society*, vol. 159, no. 10, pp. A1730–A1738, 2012.